UNIVERSITÀ DEGLI STUDI DI PALERMO

Dottorato di Ricerca in Ingegneria Chimica, Gestionale, Informatica, Meccanica
Indirizzo "Ingegneria Chimica e dei Materiali"
Dipartimento di Ingegneria Chimica, Gestionale, Informatica, Meccanica (DICGIM)
Settore Scientifico Disciplinare ING-IND 26

REVERSE ELECTRODIALYSIS
ADVANCED MODELLING AND SCALE-UP

IL DOTTORE
Ing. MICHELE TEDESCO

IL COORDINATORE
Prof. Ing. SALVATORE GAGLIO

IL TUTOR
Prof. Ing. GIORGIO MICALE

I CO TUTORS
Dr. Ing. ANDREA CIPOLLINA
Prof. Ing. DAVID BOGLE
Ing. WILLEM VAN BAAK

CICLO XXV
ANNO CONSEGUIMENTO TITOLO 2015

CONTENTS

LIST OF ISI PUBLICATIONS

- M. Tedesco, A. Cipollina, A. Tamburini, W. van Baak, G. Micale,
  Modelling the reverse electrodialysis process with seawater and concentrated brines,
  Desalin. Water Treat. 49 (2012) 404–424.

- M. Tedesco, A. Cipollina, A. Tamburini, I. D. L. Bogle, G. Micale,
  A simulation tool for analysis and design of reverse electrodialysis using concentrated brines,
  Chem. Eng. Res. Des., 93 (2015) 441–456.

- M. Tedesco, A. Cipollina, A. Tamburini, G. Micale, J. Helsen, M. Papapetrou,
  REAPower: Use of desalination brine for power production through reverse electrodialysis,
  Desalin. Water Treat. (in press), doi:10.1080/19443994.2014.934102.

- M. Tedesco, P. Mazzola, A. Tamburini, G. Micale, I. D. L. Bogle, M. Papapetrou A. Cipollina,
  Analysis and simulation of scale-up potentials in reverse electrodialysis,
  Desalin. Water Treat. (in press), doi:10.1080/19443994.2014.947781.

SUBMITTED PAPERS

- M. Tedesco, E. Brauns, A. Cipollina, G. Micale, P. Modica, G. Russo, J. Helsen,
  Laboratory scale-up of Reverse Electrodialysis for power production from seawater and brine,
  submitted to Journal of Membrane Science (2015).

PAPERS IN PREPARATION

- M. Tedesco, D. Vaccari, A. Cipollina, A. Tamburini, G. Micale,
  Operation and perspectives of the first pilot plant fed with brackish water and saltworks brines, in preparation.

- M. Tedesco, D. Vaccari, A. Cipollina, A. Tamburini, G. Micale,
  Performance analysis of the first reverse electrodialysis prototype plant operating with natural brackish water and saltworks brine, in preparation.

- F. Santoro, M. Tedesco, A. Cipollina, A. Tamburini, I. D. L. Bogle, G. Micale, *Optimal design of Reverse electrodialysis unit for power production from seawater and brine*, in preparation.

- M. Tedesco, A. Cipollina, A. Tamburini, W. van Baak, G. Micale, *Investigation of the most suitable salts for Power Production by Reverse Electrodialysis*, in preparation.

PRESENTATIONS AT INTERNATIONAL CONFERENCES

- *A multi-scale model for the reverse electrodialysis process with seawater and concentrated brines*
  Desalination for the Environment, Clean Water and Energy
  Barcelona, Spain – April 2012

- *Reverse electrodialysis with seawater and concentrated Brine: a comprehensive process modelling*
  International Workshop on Salinity Gradient Energy
  Milano, Italy – September 2012

- *SGP-RE energy production from seawater and brines: the REAPower project. Achievements and perspectives*
  INES Seminar
  Palermo, Italy – May 2013

- *REAPower: use of desalination brine for power production through reverse electrodialysis*[*]
  International Conference WIN4Life
  Tinos Island, Greece – September 2013

- *Reverse electrodialysis process with seawater and concentrated brines: a COMSOL model for equipment design*
  COMSOL Conference Rotterdam 2013
  Rotterdam, The Netherlands – October 2013

- *Reverse electrodialysis process: analysis of optimal conditions for process scale-up*
  Desalination for the Environment, Clean Water and Energy
  Limassol, Cyprus – May 2014

- *Performance analysis of the first reverse electrodialysis prototype plant operating with natural brackish water and saltworks brine*[†]
  Second International Conference on Salinity Gradient Energy
  Leeuwarden, The Netherlands – September 2014

[*] Invited speech.

[†] Awarded as Best Presentation of the conference.

SUBMITTED ABSTRACTS FOR ORAL PRESENTATIONS

- *Salinity Gradient Power from brines through reverse electrodialysis: from laboratory experiments to the first operating prototype in the world*
  Advanced Membrane Technology VI: Water, Energy, and New Frontiers
  Siracusa, Italy – February 2015

- *Operation and perspectives of the first pilot plant fed with brackish water and saltworks brines*
  Desalination for Clean Water and Energy
  Palermo, Italy – May 2015

- *Performance of a RED system with Ammonium Hydrogen Carbonate solutions*
  Desalination for Clean Water and Energy
  Palermo, Italy – May 2015

INTRODUCTION

The increasing world energy demand during the last decades, together with sustainability issues related to large use of fossil fuels, is leading to a growing interest towards new alternative energy sources. Among the several investigated opportunities, a promising option is Salinity Gradient Power (SGP), i.e. the recovery of chemical energy associated with the "controlled" mixing of two salt solutions with different concentrations. As an example, this notable potential can be exploited in coastal areas, where river mouths reach the main reservoirs (seas and oceans).

The energy theoretically exploitable from natural salinity gradients is considerably high. In fact, salinity gradient power (SGP) has been estimated to be the second largest marine-based energy source, with a global power of 980 GW potentially available for extraction.

A number of technologies have been proposed to convert SGP into mechanical energy (pressure-retarded osmosis, PRO) or directly into electricity (namely, reverse electrodialysis, RED, and capacitive mixing, CDLE). Among these, RED represents a viable technology that might be brought to industrial implementation as soon as new membranes will be available at competitive costs.

Although the principle of RED technology is well known since 1950, the status of development yet requires extensive R&D efforts for exploring the real potential of such process. The overall performance of RED process depends on membranes properties, stack design, and especially feed solution properties. In particular, although most of the applications of RED process has been so far limited to river water and seawater, the use of fresh water as dilute solution causes high electrical resistance inside the stack, thus limiting the output power. In order to reduce the resistance of the dilute compartments, sea or brackish water can be used as diluate, while concentrated brine (e.g. from saltworks, salt mines or other industrial activities) can be used as concentrate.

This concept has been at the basis of the EU-funded REAPower project (*Reverse Electrodialysis Alternative Power*), whose main goal was to demonstrate the implementation of the RED technology for the case of concentrated brines.

Focus of this PhD has been a comprehensive study of the reverse electrodialysis process, both through modelling and experimental activities. The research efforts, closely related to the R&D of the REAPower project, eventually ended up with the construction and testing of the first pilot plant operating with real brackish water and brine from a saltwork located in Marsala (Italy).

The research was initially focused on the development of a new mathematical model for the RED process powered by seawater (or brackish water) and concentrated brine. A multi-scale modelling approach has been adopted for this purpose, since it is especially suitable for design and optimisation of chemical processes of noteworthy complexity. In particular, the model has been developed at two different scales of description: (i) a lower-scale model, describing the physical phenomena in a single repeating unit of the system (*cell pair*); (ii) a higher-scale model related to the whole equipment (*stack*), including all cell pairs and the relevant interconnections. Finally, a model for the whole plant has been implemented in an equation-based solver software (gPROMS®), allowing the simulation of a number of stacks interconnected with different layouts.

The model was validated against original experimental information and then used to analyse the influence of the main operating factors on power output. A good matching was found between predictions and experiments for a wide range of inlet concentrations, flow rates and feed temperatures. The simulations performed on asymmetric stacks and assuming different feed flow arrangements between RED modules eventually provided indications for a final scale-up of the process.

The original data used for model validation were collected during a wide experimental campaign performed on a laboratory RED unit at VITO (Flemish Institute for Technological Research – Mol, Belgium). Two different sets of membranes were tested, analysing various operating conditions in terms of feed concentration, temperature and flow rate. These tests allowed to identify the optimal conditions for the investigated system and reached values of power output among the highest reported to date in the literature.

Based on the information collected from both modelling and laboratory investigations, a RED pilot plant was designed and installed in Marsala (South of

Italy) as final accomplishment of the REAPower project. A first prototype equipped with 125 cell pairs and 44x44 cm^2 membrane area was installed and tested, using brackish water (equivalent to 0.03 mol/l NaCl) and saturated brine from saltworks (5 mol/l NaCl) as feed streams. The process performance was monitored in terms of both pressure drops and power production over a period of five months of operation.

The pilot plant has been later up-scaled through the installation of two larger prototypes, each one equipped with 500 cell pairs. The plant, which has been tested over six months of operation, is currently the first plant worldwide operating with real brine and brackish water.

The research activities carried out in a real environment suggest that the RED technology can be considered as a reliable way to obtain sustainable electric energy in the near future. Moreover, the improved knowledge in RED process can lead to novel applications, which may not be confined to the use of natural streams.

To this end, the latest development of research activities carried out within the framework of this PhD led to the conceptual analysis of a heat engine based on RED technology, in which artificial salinity gradients are used to produce electricity. The discharged solutions from the RED unit are then regenerated by low-grade heat through a suitable thermal separation stage. Therefore, the RED process can be exploited as a viable alternative to recover industrial waste heat and produce electricity in a sustainable way.

The present thesis has been organised to cover the main aspects of the RED process and describe the aforementioned objectives.

In particular, **Chapters 1** presents an overall introduction to the RED technology, presenting the state-of-the-art and the current barriers to overcome.

Chapter 2 reports some useful background information on electro-membrane processes.

Starting from the relevant works in the literature, **Chapter 3** describes in detail the development of the proposed multi-scale model. Moreover, the new process simulator for the whole plant is presented.

Chapter 4 reports the model predictions and the results achieved both for laboratory and prototype units.

Chapter 5 showed the laboratory experimental campaign performed at VITO. Apart from giving input for model validation, such campaign led to significant outcomes for characterising the best process conditions. The information collected during such period was therefore extremely useful for the final scale-up of the technology.

Chapter 6 describes all the phases occurred during the design, construction and testing of the REAPower demonstration pilot plant.

Chapter 7 reports the operation and results collected in the real environment over a period of six months.

Finally, **Chapter 8** focuses on the development of a 'RED-heat engine' system, through a theoretical investigation of suitable salts and a preliminary analysis of possible thermally-driven technologies to regenerate the working fluids.

1 THE REVERSE ELECTRODIALYSIS PROCESS[*]

Abstract

Salinity Gradient Power (SGP) is a valuable renewable energy source based on the controlled mixing of two solutions of different salinity. Reverse Electrodialysis (SGP-RE or RED) is, in turn, a promising technology to exploit this energy source and directly generate electricity.

The aim of this chapter is to provide a brief review of the development of RED process, understanding the main technological barriers still to overcome for a successful scale-up of the process. In fact, although the principle of this technology has been well known for several years, further R&D efforts are still necessary in order to explore the real potential of RED process.

In particular, the use of seawater (or brackish water) and concentrated brine as feed solutions can lead to a significant enhancement of the power output from a RED system. This concept has been the basic idea of the EU-funded REAPower project, whose main goal was demonstrating the potential of reverse electrodialysis technology with concentrated brine through the construction of the first RED pilot plant in a real environment.

[*] Part of this chapter has been published in revised form as:

- M. Tedesco, A. Cipollina, A. Tamburini, G. Micale, J. Helsen, M. Papapetrou, *Reapower: Use of Desalination Brine for Power Production through Reverse Electrodialysis*, Desalination and Water Treatment (in press), doi:10.1080/19443994.2014.934102.

1.1 Introduction to Salinity Gradient Power

Research activities on "water-related" renewable energy sources have seen an increasing interest during last years. While hydroelectric processes already exploit 800 GW worldwide, salinity gradient power (SGP) remains an untapped source of energy [1].

SGP can be seen as the chemical potential energy that can be exploited when two salt streams with different salinity (e.g. river water and seawater) are mixed together. The amount of energy theoretically exploited can be estimated as the Gibbs free energy of mixing [2]. According to this calculation, mixing one cubic meter of seawater (0.5 M) with the same volume of fresh water (5 mM), about 0.5 kWh of energy can be theoretically produced, i.e. equivalent to the hydroelectric power of 1 m^3 of water flowing down a 175 m waterfall [3]. On the basis of average ocean salinity and annual global discharge of rivers, the available power from salinity gradients has been estimated to be between 1.4 and 2.6 TW [4]. Taken into account technical issues related to actual energy conversion, about 980 GW of such energy could be harvested [3], which still represents a notable amount of renewable energy.

Different technologies have been proposed to convert SGP into more exploitable forms, i.e. mechanical energy or electricity. Among these, two membrane-based processes have been widely investigated so far: pressure-retarded osmosis (PRO [2,5]) and reverse electrodialysis (RED). These two processes can be seen as the opposite of the well-known desalination technologies (reverse osmosis and electrodialysis, respectively), where the use of selective membranes allow the passage of only solvent (PRO and RO) or ions (RED and ED).

Aside from PRO and RED, other salinity gradient power technologies have been recently proposed, based on the use of capacitive electrodes [6], which can be also coupled with ion exchange membranes [7]. However, these technologies, whose main bottleneck is the development of suitable electrode materials, are still in their very early research stage, and will not described in this thesis.

In pressure-retarded osmosis, two streams with different salinity are mixed together through a semi-permeable membrane, which allows the flow of solvent (water), and retains the solute (dissolved salts). As a result, water flows by osmosis

through the membrane towards the concentrated compartment. If a hydrostatic pressure is applied to the concentrate compartment, the water flux results in a pressurisation of the concentrate. Such pressurised solution can be sent to a hydroturbine to generate electricity.

In the reverse electrodialysis process, dilute and concentrated solutions are separated by ion exchange membranes (IEMs), which are selective to the passage of either cations or anions. Therefore, cations flow through cation exchange membranes (CEMs), while anions flow through anion exchange membranes (AEMs). As a result, the salinity gradient creates an ionic current through the membranes; the ionic current is eventually converted into electric current at the electrodes. As this technology has been the focus of this thesis, a more detailed description of its principle is reported in the next paragraph.

A comprehensive comparison between pressure-retarded osmosis and reverse electrodialysis has been already presented by different authors [1–3], and it is beyond the scope of this thesis. In particular, Post suggested that RED might be characterised by lower pre-treatment requirements with respect to PRO, as electrodialysis membranes are generally less sensible to biofouling than reverse osmosis membranes [2,8].

Both RED and PRO have experienced an increasing interest among the scientific community during the last decade. In the case of PRO, a notable breakthrough for the technology has been the use of pressure exchangers, firstly proposed by Loeb in 2002 [9]. On the other hand, the main challenge of both technologies is the development of new membranes with high performance (namely, high water permeability for PRO and low resistance for RED) and relatively low cost (especially for RED, as ion exchange membranes are generally more expensive than osmosis membranes).

Aside from the widely investigated PRO, RED and capacitive mixing processes, researchers are currently focused on new systems for exploit salinity gradients, e.g. based on swelling properties of hydrogels [10]. Such growing interest in the development of new SGP technology clearly demonstrates that salinity gradient power might change the overview on renewable energy source in the near future.

1.2 Principle of reverse electrodialysis

The principle of RED is sketched in Figure 1.1. The repeating unit of the system (*cell pair*) is constituted by a Cation Exchange Membrane (CEM), a dilute (LOW) compartment, an Anion Exchange Membrane (AEM) and a concentrate (HIGH) compartment. As in electrodialysis, up to several hundreds of cell pairs can be stacked within a single unit for practical applications [11]. Polymeric net spacers are normally used to maintain the inter-membranes distance, as well as for reducing concentration polarisation phenomena [12]. At the ends of the stack, two external compartments contain the electrodes and an electrolyte solution (*electrode rinse solution*) with a suitable redox couple (e.g. Fe^{2+}/ Fe^{3+} chloride [13]).

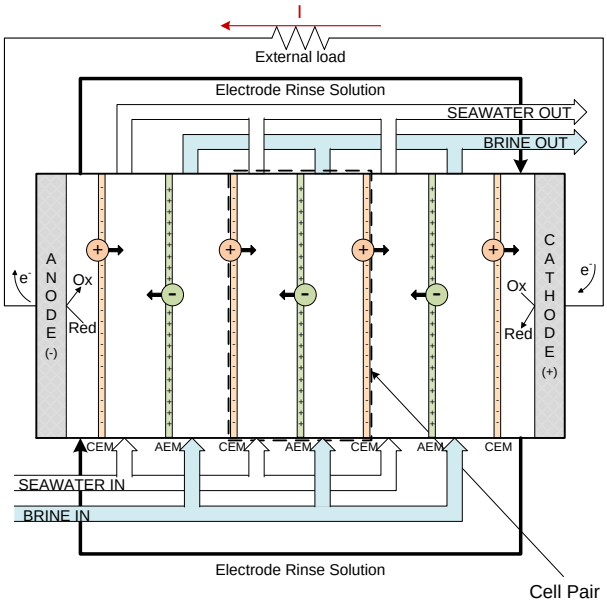

Figure 1.1. Principle of the RED process. The repeating unit of the system (cell pair) is constituted by a CEM, a dilute compartment, an AEM and a concentrate compartment. In this picture, seawater and brine are adopted as feed solutions.

When two salt solutions with different salinity are fed to the stack, the concentration gradient causes the transport of ions through the membranes. This ion

flux is regulated by the membrane permselectivity, i.e. the selectivity towards cation/anion transport through CEM/AEM, respectively. Ideally, only cations can flow through CEMs, and only anions through AEMs (in the opposite direction). The ionic current through membranes is eventually converted into electric current by means of redox reactions at the electrodes, and can be collected by an external load.

The RED process has been described as a reliable technology in the literature since 1954 [14]. Since then, a number of researchers demonstrated by experiments the feasibility of the RED process (Figure 1.2). Conventional electrodialysis (ED) stacks, i.e. built with membranes and spacers commonly used for ED, were initially exploited for this purpose [15–17].

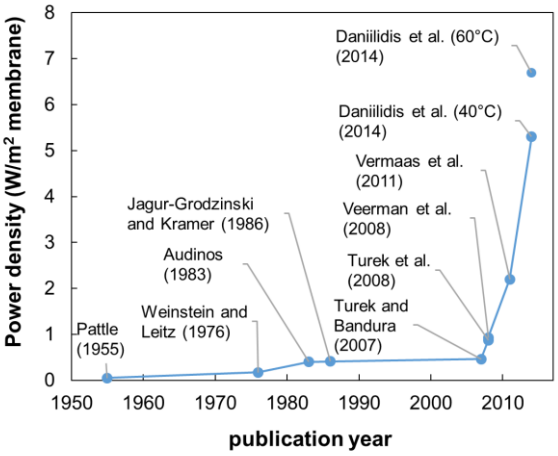

Figure 1.2. Power density (expressed as W/m^2 of membrane) experimentally obtained in RED system. Sources: [14–21].

During the last years, the RED process has seen notable improvements thanks to the investigation presented by different authors, especially by Post [22], Długołecki [23], Veerman [24] and Vermaas [25]. With this regard, Veerman et al. obtained a power of 0.93 W with a 50 cell pairs stack of 1 m^2 of total membrane area, using river water and seawater as feed solutions [20].

The use of river water has in fact a remarkable drawback: the low conductivity of the solution causes high electric resistance within the unit, limiting the output power

achievable. For this reason, decreasing the compartments thickness a considerable reduction of the stack resistance is obtained, thus enhancing the output power. For instance, Vermaas et al. reported a power density of 2.2 W/m^2 of membrane using spacers of 60 μm thickness [26]. Such thin compartment thickness might be necessary to reduce the electric resistance in the river water compartment. On the other hand, very thin channels cause high pressure drops, increasing the risk of fouling. Another possibility to avoid high resistance in the dilute compartment is using seawater (instead of river water) as dilute, and a more concentrated solution as concentrate, such as concentrated brine from salt ponds, salt mines or other industrial activities [27–29].

1.3 Membrane development

The first studies on RED process were based on the use of commercial membranes for electrodialysis [14–18]. Audinos [15] (and, more recently, Długołęcki [30]) clearly suggested that the development of new IEMs is necessary to suit the requirements of RED technology. In particular, the suitable IEMs should have:

- *Low electrical resistance.* Membranes with an electric resistance as low as possible are required, especially when highly concentrated solutions are used as feed, when IEMs resistance represent more than 70% of the overall stack resistance [31]. Moreover, in the case of fresh water – seawater conditions, it has been experimentally demonstrated that membranes resistance increases significantly due to the low concentration of fresh water [32,33].
- *High permselectivity.* The permselectivity of commercial membranes is generally rather high (>96%) when diluted solutions are used (i.e. typical concentration of river water and seawater). On the other hand, the permselectivity decreases sensibly when highly concentrated solutions are used [33].
- *Good mechanical stability.* While the development of very thin membranes may reduce significantly the overall resistance, a good mechanical stability

should be guaranteed for practical applications. Moreover, a low swelling degree increase the mechanical stability of membranes [34].

- *High chemical stability*. The membrane should be stable in a wide range of pH. This is particularly relevant when low pH (2-3) is kept in the electrode compartments of some RED systems [13,35].
- *High thermal stability*. High temperature has been proven to benefit the performance of RED process [21]. The development of IEMs stable at T > 60°C might be a further enhancement of the technology.

Apart from the aforementioned properties, a significant reduction in the cost is necessary to make RED technology economically feasible in the near future. Post assumed a cost of installed membranes of 2 €/m^2 (including end plates and electrodes) for an economic analysis of a 200 kW RED module. In this way, a cost of electricity of 0.08 €/kWh is estimated, i.e. comparable with the price of wind energy [36]. More recently, Daniilidis suggested that a cost of membranes below 4.3 €/m^2 would be already acceptable for making RED technology economically feasible. On the other hand, this more optimistic estimation may be achieved assuming the use of brine instead of seawater as concentrated feed stream [37].

1.4 Stack design for reverse electrodialysis

In principle, the stack design developed for commercial electrodialysis units can be adopted for RED process. Co-current flow configuration is generally preferable in ED, in order to avoid leakages due to local pressure difference across membranes [38]. In fact, Veerman demonstrated that a counter-current flow configuration does not improve appreciably the overall performance, leading just to a 1% increase of the power output, yet increasing the risk of internal leakages [39].

More recently, several patents have been reported on new stack design, based on cross-flow arrangement for feed solutions [40]. The aim of such new design is to ensure a more homogeneous flow distribution within compartments, in order to reduce the internal resistance of the stack. In particular, a crucial aspect in stack design is the development of a suitable flow distribution system, i.e. able to reduce the concentrated

pressure drops at inlet/outlet and ensure a homogeneous flow distribution inside channels [41,42].

1.5 Net spacers and profiled membranes

In conventional electrodialysis units, polymeric woven spacers are adopted to separate membranes and create the compartments for solutions [38]. Both geometry and thickness of the spacer are important parameters for reducing pressure drops, thus enhancing the net power output of the system [12,41]. In particular, the use of thinner spacers clearly reduce the electrical resistance of the compartments, thus increasing the power output. For this reason, in general a lower compartments thickness is preferable in reverse electrodialysis.

Vermaas analysed the influence of different types of spacers on power output, ranging from 485 μm down to 60 μm thickness, observing that using very thin spacers allow to double the power density with respect to the case of thicker spacers [26]. Such effect is remarkable when fresh water is used as dilute, being the main ohmic loss in the overall stack resistance [33].

A sensible reduction of the overall stack resistance has been achieved by using conductive spacers instead of common (uncharged) spacers. Długołecki et al. showed that the use of ion-conductive materials allow to halve the resistance when river water and seawater are used as feed, thus increasing the power density by a factor of 3 [43]. Starting from these results, further efforts have been focused on the construction of profiled membranes, were the spacers are substituted by properly structured IEMs. In this way, a reduction of the overall resistance was detected, although increasing the influence of concentration polarisation phenomena on the process. As a result, only a slight increase in the power density was observed, essentially at high flow velocity [44]. Such first experimental results suggest that the use of profiled membranes can lead to a reliable improvement in the stack design of RED process, though the current development requires further investigation for identifying proper structure/geometry for the membranes.

1.6 Electrode systems for RED

The electrode system required for a RED unit is constituted be two electrodes (anode and cathode) placed in the outer compartments, plus two "outer" membranes (for separating effectively the solution flowing in the electrode compartments from concentrate and diluate), and an electrode rinse solution, which contains a suitable redox couple for electrochemical reactions.

The selection of suitable conditions for the electrode system is of a prior importance for guaranteeing stable performance of the RED process. The first experimental works on RED process were performed using NaCl solutions as electrode rinse solution [2,16]. However, this determines the formation of chlorine and H_2 as anodic and cathodic products, respectively. In fact, the formation of gaseous species at the electrode surface causes also a significant increase of the electric resistance in the compartments. Such phenomenon has been observed also in RED system using ammonium bicarbonate as active species for the electrode rinse solution [45]. Sodium sulphate (Na_2SO_4) can be used to avoid chlorine formation, generating oxygen at the anode [18,19].

A detailed investigation of suitable electrode systems for RED has been performed by Veerman, who compared a number of electrode systems in terms of safety, health, environment, technical feasibility and economics [13]. Based on such investigation, the most suitable system proposed was the use of Fe^{2+}/ Fe^{3+} couple in a NaCl-HCl supporting electrolyte, with Ru/Ir covered titanium electrodes [13]. Apart from Fe^{2+}/ Fe^{3+} couple, also hexacyanoferrate $[Fe(CN)_6]^{4-}$/$[Fe(CN)_6]^{3-}$ is widely used as redox species in RED process [20,46]; in fact, this species is very stable in the process conditions, provided that the contact with oxygen and light is avoided [47].

1.7 Pre-treatment strategies

Fouling and biofouling phenomena are relevant issues that affect the efficiency of any membrane process. Although ion exchange membranes are less sensitive to fouling than reverse osmosis membranes [8], some pre-treatment strategies of the feed solutions are still required to guarantee long-term operation with natural streams. In

particular, ion exchange membranes are subject to fouling by electrically charged particles, such as polyelectrolytes, humic acids, and surfactants [38]. Moreover, IEMs can also suffer the adsorption of natural organic matter, thus causing a dramatic increase of the electrical resistance [48].

In electrodialysis applications, the periodical switching of the polarity of electrode (i.e. Electrodialysis Reversal, EDR [49]) allowed to reduce the fouling caused by organic acids and charged colloids [50]. This method led to a significant less impact of fouling phenomena in ED, and lead to long-term operation. The same principle has been proposed as possible strategy in reverse electrodialysis, i.e. based on a reversal of feed waters [22,51]. With this regard, Post showed that a single reversal of feed streams is not effective to reduce pressure drops in RED stack where biofilm formation occurred. On the other hand, a periodical switching (i.e. daily or hourly) was useful to retard biofouling phenomena in the first 15 days [22].

Testing a RED stack with real seawater and fresh water, Vermaas observed that colloidal fouling occurred, mainly due to clay minerals and remnants of diatom shells [52]. In particular, when using a 20 μm filter was used as only pre-treatment, the fouling rate was unacceptable, causing a 50% reduction of power density in the first day of operation [52]. With this regard, periodic air sparging and switching of feed streams have been proposed as valuable methods to reduce colloidal fouling [51].

1.8 The REAPower project: RED process with concentrated brine

The use of fresh water as dilute stream causes high electrical resistance, thus limiting the power output achievable by the RED system. On the other hand, using seawater (or brackish water) as diluate and brine as concentrate allows to reduce significantly the internal electrical resistance, keeping an high salinity gradient as driving force for the RED process. This concept was the basic idea of the EU-funded REAPower project (*Reverse Electrodialysis Alternative Power*), whose main goal was to demonstrate the potential of RED technology using sea/brackish water and brine as feed solutions [29]. In particular, the final accomplishment of the REAPower project has been the installation of a demonstration prototype plant in the South of Italy

(Figure 1.3). The installation site is located in a saltwork area in Marsala (Trapani, Italy), an ideal location for a RED plant, providing a large amount of both solutions required for power production.

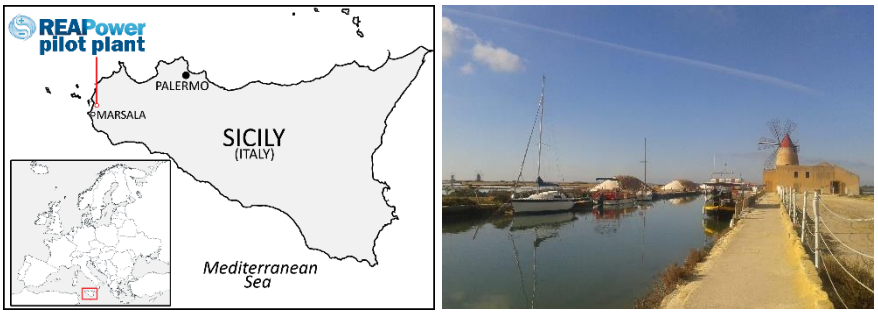

Figure 1.3. Location of the REAPower pilot plant in Marsala (Trapani, Italy). A picture of the windmill hosting the RED pilot plant is shown on the right.

The presence of highly concentrated solutions inside the system strongly affects the membranes properties, such as permselectivity and electric resistance. Therefore, significant R&D efforts are necessary to achieve high process performance. For this reason, the following R&D activities have been identified and addressed within the REAPower project:

i. Development of new components (such as membranes, spacers, electrode rinse solution, stack) tailored to the new process requirements;
ii. Development and validation of a suitable process simulator, so as to provide a predictive modelling tool for investigation on scaled-up units;
iii. Experimental investigation of the developed RED system through laboratory-scale testing;
iv. Design, construction and testing of a RED pilot plant operating with natural solutions in a real environment;
v. Economic analysis of the process, thus identifying the environmental impact and next R&D activities necessary to develop further the RED technology.

The research efforts presented in this thesis have been strongly related to the activities of the REAPower project, especially points (ii)-(iv). In particular, the

development of a multi-scale model for RED process under seawater-brine conditions is described in Chapter 3, while the model predictions and simulations of the pilot plant are presented in Chapter 4. The experimental campaign carried out on a laboratory RED unit at VITO (Flemish Institute for Technological Research) is described in Chapter 5. Finally, the phases of design, construction and testing of the REAPower pilot plant are described in detail in Chapters 6-7.

2 FUNDAMENTALS OF ELECTRO-MEMBRANE PROCESSES

Abstract

Any chemical process requiring the use of ion exchange membranes (IEMs) is strongly influenced by the properties of the membranes themselves. Therefore, a fundamental study of the relevant features of ion exchange membranes is required to understand fully the technological challenges of reverse electrodialysis process.

Focus of this chapter is to provide some fundamentals on the properties of ion exchange membranes. According to their structure and preparation procedures, ion exchange membranes are normally classified as homogeneous and heterogeneous IEMs. The most relevant properties are the ion exchange capacity, permselectivity, and electrical resistance. Among these, permselectivity and resistance are strongly affected by the solutions properties, apart from the chemical structure of the membrane.

The study of transport phenomena through IEMs involves in fact both ions and solvent transport. In particular, water can be transported according to two mechanisms: osmosis and electro-osmosis. This latter is related to the transport of water molecules bounded to ions in the hydration shells, thus is linked to ions transport through IEMs.

2.1 Introduction to electro-membrane processes

The term *electro-membrane processes* refers to any chemical process that involves transport phenomena through ion exchange membranes (IEMs). In fact, such term covers a wide class of processes, which can be notably different by goals, applications and relevance on the industrial scale.

The history of ion exchange membranes can be dated back to 1890, when Ostwald discovered that a membrane can be impermeable for any electrolyte if it is impermeable either for its cation or anion [53]. This phenomenon was confirmed and theoretically modelled in 1911 by Donnan, who described for the first time the electrical potential that arise across membranes (so-called "Donnan exclusion potential" [54,55]).

Generally, the electro-membrane processes are classified into three categories (Table 2.1):

1. *Separation processes.* Adopted for the removal of potential or true electrolytes (i.e. acids, bases or salts) from a solution by application of an electric field. The driving force for the process can be either an electric potential (e.g. as in electrodialysis), or a concentration gradient (e.g. diffusion dialysis, Donnan dialysis).
2. *Synthesis processes*. The aim of these processes is the production of chemical compounds (both organic and inorganic) through the application of an electric field and suitable conditions at the electrodes. Therefore, an electrochemical reaction is involved in these processes. In this field, the largest industrial application is the chloro-alkali process, with a global production of more than 48 millions of tons of NaOH and more than 42 millions of tons of Cl_2 [56].
3. *Energy conversion processes*. In this case, the aim is the conversion of chemical potential of a system into electric energy, as in the RED process. The most important industrial applications in this field are fuel cells, although other new processes such as capacitive deionization and reverse electrodialysis are gaining interest.

Table 2.1. Applications of electro-membrane processes. Adapted from [11].

Process	**Applications**	**Advantages**	**Main drawbacks**
Separation processes			
Electrodialysis	Brackish water desalination	Low cost High recovery rate	Low Feed concentration
	Waste water treatment	Recovery of components	Membrane and process costs
	Salt production from seawater	More economic than evaporation	Membrane costs and selectivity
Electrodialysis with bipolar membranes	Acid and base production	No toxic waste products	Low product purity Membrane costs and life
	pH control in bioprocesses	No additional salt	Membrane and process costs
Diffusion dialysis	Acid and base recovery	Less waste disposal	Product concentration Membrane costs
Donnan dialysis	Counter current ion transport	Less waste disposal	Process costs Product water quality
Continuous Electrodeionization	Ultra-pure water production	Less waste disposal	Product water quality
Capacitive deionization	Water deionization	No toxic waste products	Electrode surface area and costs
Synthesis processes			
Electrolysis	Chloro-Alkali production	Low energy costs	Membrane costs
	Hydrogen production	Unlimited feed stock	Process and energy costs
Energy conversion processes			
Fuel cells		High efficiency	Feed supply
Redox-flow cell		Costs	Membrane selectivity
Reverse electrodialysis		Large feed stock supply	Membrane costs

Looking at the relevance in the industrial scale applications, all these technologies present notable difference. In particular, the separation processes undoubtedly represent the most investigated category among the electro-membrane processes. However, during last decades the development of innovative membranes with better performance led to the spreading of new research field and interesting scenarios for future large-scale applications.

2.2 Physical properties of Ion Exchange Membranes

Ion exchange membranes are the key element of all electro-membrane processes: the overall efficiency of the process, as well as plant shutdown operation, pre-treatment and maintenance costs are largely dependent on the properties of the IEMs. The IEMs currently available in the market can be classified into three categories:

- *Anion exchange membranes (AEMs)*. polymeric membranes containing positively charged groups, such as $–NH_3^+$, $–NRH_2^+$, $–NR_2H^+$, $–NR_3^+$, $–PR_3^+$, $–SR_2^+$. They allow the passage of anions, rejecting cations.
- *Cation exchange membranes (CEMs)*. They contain negatively charged groups, such as $–SO_3^-$, $–COO^-$, $–PO_3^{2-}$, $–PO_3H^-$, $–C_6H_4O^-$, fixed to the membrane backbone. They allow the passage of cations, thus rejecting anions.
- *Bipolar membranes (BPM).* These membranes are constituted by a layered ion exchanged structure composed of a cation selective layer and an anion selective layer. The development of these new type of membranes is bringing to significant novelties for IEMs applications, such as separation of mono- and divalent ions, anti-deposition, anti-fouling and water dissociation [53]. In particular, electrodialytic water splitting using bipolar membranes is a very energy-efficient way to produce acids and bases from the corresponding salts [38].

The main properties of some ion exchange membranes commercially available are listed in Appendix A.

2.2.1 Ion exchange capacity

The ion exchange capacity (IEC) represents the amount of charges per unit weight of dry membrane, and is normally determined by tritation [11,34]. For cationic membranes, the test is carried out by equilibrating the membrane sample in a 1 N HCl solution for 6 hours. Likewise, the test for anion exchange membrane is performed uising a 1 N NaOH solution. The samples are then rinsed with deionized water to

remove Cl^- or Na^+ from the solution. The IEC is therefore measured by back tritation with 0.1 NaOH or HCl, for CEMs and AEMs, respectively. Finally, the samples are dried and IEC (meq/g) can be determined as

$$IEC = \frac{c_{total}}{m_{dry}} \tag{2.1}$$

where c_{tot} (meq) is the total charge measured by tritation (i.e. product of burette reading and the concentration of the solution), and m_{dry} is the dry weight of the membrane sample (g). Typical values of IEC for homogeneous membranes are in the range of 0.9-2.5 meq/g. Some data for membranes available in the market are reported in Appendix A.

Ion exchange capacity can be also used to determine the concentration of fixed charges (X^m) as number of sites per unit volume of wet membrane [34]:

$$X^m = \frac{\tau (IEC)\rho_d}{\Delta V} \tag{2.2}$$

where ρ_d is the density of dry membrane, ΔV is the volume increase due to water adsorption per unit volume of dry membrane, and τ is the membrane porosity, i.e. the volume of free water within membrane per unit volume of wet membrane.

2.2.2 Permselectivity

Permselectivity is an important parameter to quantify the selectivity of ion exchange membranes towards the passage of either cations or anions. It can be seen as a measure of the Donnan exclusion of the membrane, i.e. the ability to reject co-ions from the membrane phase and allow the flux of only counter-ions.

According to its definition, the permselectivity of an ion exchange membrane (α_{IEM}) is given by:

$$\alpha_{IEM} = \frac{T_i^m - T_i}{1 - T_i} \tag{2.3}$$

where T_i^m and T_i are the transport number of counter-ion inside the membrane phase and in bulk solution, respectively. As shown by eq. (2.3), the permselectivity approaches zero when counter-ions have similar transport numbers into the membrane and in solution. However, the transport number of counter-ions in membrane is generally higher than in solution, thus α_{IEM} tends to unity. Typical values of α_{IEM} in conventional applications for electrodialysis are in the range of 96-99% when measured between 0.01 M and 0.5 M NaCl solutions (Appendix A). On the other hand, such values decrease significantly when different conditions are applied, e.g. increasing the concentration in the bulk solution [57]. In fact, permselectivity is influenced by both membrane and solution properties, in particular by the concentration of fixed ions, and by both valence and concentration of ions in solution.

The IEM permselectivity can be determined either through the evaluation of transport numbers (Hitorf's method), or by means of membrane potential measurements.

According to Hitorf's method, transport numbers are calculated in electrodialysis experiments measuring the concentration change in dilute and concentrate compartments when a certain amount of current is applied to the system [58]. In this way, the transport of solvent is also taken into account, and the "true" permselectivity is calculated. However, the Hitorf's method is rather time-consuming, and affected by concentration polarization phenomena [11].

A faster method to evaluate IEM permselectivity is based on the determination of membrane potential [59]. In this case, the IEM under investigation is placed between concentrate and dilute compartments, and the electric potential arising across the membrane is measured by two Haber-Lugging capillaries (Figure 2.1). Therefore, the permselectivity is evaluated as the ratio of the measured potential (ΔV_{meas}) and its theoretical value (ΔV_{theo}):

$$\alpha_{IEM} = \frac{\Delta V_{meas}}{\Delta V_{theo}} \tag{2.4}$$

The theoretical membrane potential is commonly estimated from the Nernst equation [60]:

$$\Delta V_{theo} = \frac{RT}{F} \ln\left(\frac{a_{HIGH}}{a_{LOW}}\right) \tag{2.5}$$

where R is the universal gas constant, T the absolute temperature, F the Faraday constant, a_{HIGH} and a_{LOW} are the activities of concentrate and diluate, respectively.

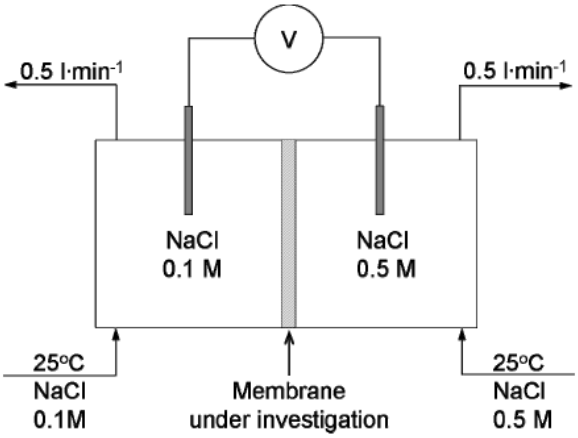

Figure 2.1. Set-up for the evaluation of permselectivity by membrane potential measurement [23]. The typical investigation conditions are shown, i.e. using 0.1 M and 0.5 M NaCl solutions.

Unlike the Hitorf's method, the evaluation of permselectivity by membrane potential does not take into account transport of solvent (neglected in eq. (2.5)). As a result, the permselectivity evaluated by this method is generally referred as "apparent" permselectivity, and is always larger than the true permselectivity [11]. On the other hand, the difference between true and apparent permselectivity is generally very small, and this method is widely adopted for characterising membranes in manufacturing processes.

2.2.3 Electrical resistance

The electrical resistance of membrane can play a notable role in determining the overall process performance, even though the IEM resistance is lower than the resistance of the dilute compartment in many practical applications [11,34]. Membrane resistance is commonly expressed as "areal" resistance (Ω cm^2), which is a more convenient unit than specific resistance (Ω cm) from an engineering point of view. The electric resistance of a membrane is influenced by a number of factors, which can be related to both IEM structure and solutions properties. Among the most relevant influencing factors, the ion exchange capacity and the mobility of ions within the membrane matrix play a significant role. The mobility of ions depends on a number of properties of the solute (such as ion size, valence, hydration number), and on the water content of the membrane. Lower IEMs resistance is favoured by small ion size, low ion valence and high external concentration [33]. On the other hand, the concentration of the external solution can have a complex influence on IEM resistance, as some authors showed that IEMs conductivity can decrease in the presence of highly concentrated solutions [61,62]: such phenomenon might be due to a shrinking of the membrane matrix by osmosis, thus causing an increase in the membrane resistance. Regarding the membrane structure, high charge density and low degree of cross linking are preferable to reduce the IEMs resistance [34].

The electric resistance of IEMs can be determined by direct current (DC) measurements or by applying alternating current (AC) conditions.

The experimental test-rig for DC measurements is constituted by a six-compartment cell (Figure 2.2). The membrane under investigation is placed between the two central compartments of the stack, together with two Haber-Lugging capillaries. Typically, a 0.5 M Na_2SO_4 solution is used in the electrode compartments [63]. The NaCl solution is fed in the central compartments and in two lateral compartments to avoid any influence of the electrode solution on the measurement. During the measurements, the potential drop across the membrane is determined as a function of the current (I-V curve). The slope of the I-V curve in the first region (i.e. before limiting current conditions) gives the resistance of the IEM plus the non-compensated ohmic resistance between capillaries. Such last contribution is

determined in a second measurement without the membrane sample (blank) and subtract to the first measurement to obtain only the IEM resistance.

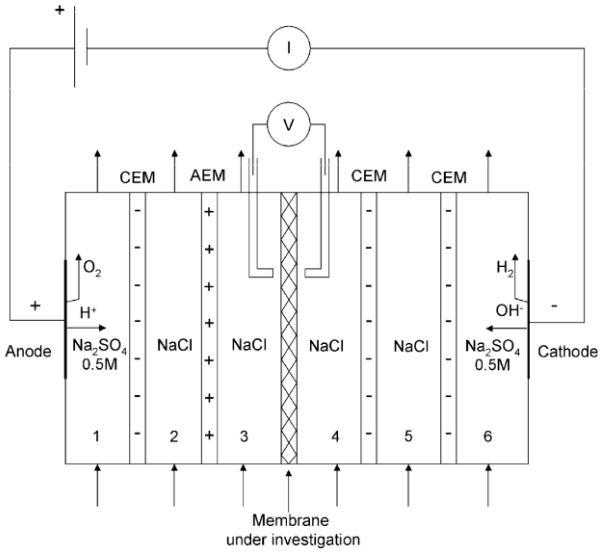

Figure 2.2. Experimental setup for IEM electric resistance measurements. Adapted from [23].

The electric resistance of IEMs can also be determined in AC conditions, by means of electrochemical impedance spectroscopy (EIS [64,65]). The measuring cell is similar to the test-rig shown in Figure 2.2. During the measurement, an alternating sinusoidal current or voltage (depending on the system) of a given frequency and amplitude is applied to the system, while the response of the system is monitored. Therefore, the voltage drop is measured as a function of time, and the phase shift (ϕ) can be determined with respect to the input signal. The impedance (Z) is then calculated by Ohm's law as:

$$Z = \frac{E(t)}{I(t)} \tag{2.6}$$

where *E(t)* and *I(t)* are the voltage and current as a function of time, respectively. The measurement is repeated at different frequencies. Substituting the expression for *E(t)* and *I(t)*, and by applying Euler's formula, the impedance can be expressed as [65]:

$$Z(\omega) = \frac{E_0 e^{j\omega t}}{I_0 e^{(j\omega t + \varphi)}} = |Z|\cos\varphi - j|Z|\sin\varphi \tag{2.7}$$

The real part of impedance in eq. (2.7) is attributed to ohmic resistance (i.e. essentially the membrane resistance), while the imaginary part is linked to non-ohmic contributions, such as diffusion boundary layer resistance [44,65].

In order to link the real part of the impedance to the resistance of IEM, an equivalent circuit is adopted. In fact, the main drawback of EIS is the definition of such equivalent circuit, which should reflect suitably the electrical behaviour of the investigated system.

Typical values of electric resistance of IEMs range between 1 and 3.5 Ω cm^2. Some relevant data for IEMs commercially available are reported in Appendix A.

2.3 Transport of solvent through IEMs: osmosis and electro-osmosis

The transport of water through IEMs is attributed to two different mechanisms: osmosis and electro-osmosis. While osmosis is related to the transfer of solvent by osmotic pressure difference, electro-osmosis refers to the transport of water molecules by drag or bounded in the hydration shell of transported ions [11]. Such transport mechanism has been experimentally demonstrated to be relevant especially in electrodialysis, where water is manly transported by electro-osmosis [66,67].

Unlike the osmotic flux, which is always directed from dilute to concentrate, the electro-osmotic flux can be directed towards either diluate or concentrate, according to the process conditions. In particular, under electrodialysis conditions, such flux is directed towards the concentrated compartment, i.e. in the same direction of the osmotic term. Conversely, in a current-less condition (such as in reverse

electrodialysis), both the ion and electro-osmotic fluxes are directed towards the diluate compartments, due to the concentration gradient [68]: as a result, the osmotic and electro-osmotic terms are counteracting.

Both osmotic and electro-osmotic fluxes can be relevant in practical applications, despite ion exchange membranes are designed to be ideally permeable only to solutes. Unlike osmosis, which is proportional to the osmotic pressure difference and can be easily estimated, electro-osmosis is difficult to evaluate quantitatively. The general approach is to consider the electro-osmotic flux proportional to the ion flux [68]. Therefore, the ratio of electro-osmotic and ion flux can be assumed as equal to the hydration number of the electrolyte, i.e. the number of water molecules firmly bounded in the hydration shells. The hydration numbers of Na^+ and Cl^- in bulk solutions have been estimated as 3.5 and 2, respectively [68]. Although these numbers decrease within the membranes due to steric hindrance [66], constant values can be assumed for practical reason, thus evaluating the electro-osmotic flux as proportional to the ion flux through the membranes.

3 DEVELOPMENT OF A MULTI-SCALE MODEL FOR RED PROCESS*

Abstract

In this chapter, a comprehensive model is proposed for RED process using seawater (or brackish water) and concentrated brine as feed solutions. The modelling goals were (i) reliably describing the physical phenomena involved in the process and (ii) building a simulation tool for evaluating the operation of a pilot plant. To this end, the model has been developed at two different scales of description: a lower scale for the repeating unit of the system (*cell pair*), and a higher scale for the entire equipment (*stack*).

For the first time, proper correlations were used to evaluate the physical properties of highly concentrated solutions, such as activity/osmotic coefficients and equivalent conductivity. Furthermore, a number of non-ideal effects have been taken into account, such as solvent transport through membranes (i.e. osmotic and electro-osmotic fluxes) and parasitic currents (ionic currents through manifolds and not through membranes).

Finally, the model has been implemented in an equation-based solver software (gPROMS) to build a process simulator. The simulator presents a graphical user interface allowing the user to set all the stack parameters and experimental conditions, in order to simulate the performance of the RED unit in a wide range of operating conditions.

* Part of this chapter has been published in revised form as:

- M. Tedesco, A. Cipollina, A. Tamburini, W. van Baak, G. Micale, *Modelling the Reverse Electrodialysis process with seawater and concentrated brines*, Desalination and Water Treatment, 49 (2012), 404-24.
- M. Tedesco, A. Cipollina, A. Tamburini, I. D. L. Bogle, G. Micale, *A simulation tool for analysis and design of Reverse Electrodialysis using concentrated brines*, Chem. Eng. Res. Des., 93 (2015) 441–456.

3.1 State-of-the-Art of RED process modelling

The earliest modelling works regarding RED process were presented by Weinstein and Leitz in 1976 [16], and Forgacs in 1979 [69]. These authors calculated the Gibbs free energy from the mixing of two saline solutions, providing for the first time an estimation of the amount of energy obtainable by reverse electrodialysis. As an example, Forgacs estimated that 0.44 kWh could be ideally produced by mixing 1 m^3 of seawater (0.5 M NaCl) and 1 m^3 of river water (0.005 M NaCl) using 100% permselective membranes. According to this model predictions, the theoretical energy production increases by more than one order of magnitude if concentrated brine (5 M NaCl) is used instead of seawater [69]. However, such models were based only on the estimation of the gross power, notwithstanding crucial process parameters such as membrane properties and operating conditions. For instance, molar concentrations were used instead of activities, and any influence of salt concentration on membrane/solutions properties was neglected. Moreover, relevant phenomena such as concentration polarisation and solvent transport by osmosis/electro-osmosis were not taken into account. Despite the simplicity of this approach, Forgacs already provided significant indications for enhancing the process performance, such as the development of membranes with very low resistance (0.4 – 0.6 Ω cm^2), or the importance of a careful investigation of optimal flow velocity (less than 1 cm/s) to maximise the net power.

The first comprehensive model for RED process was proposed by Lacey [70], who suggested a novel approach for estimating the power output in terms of voltage and resistance of a single cell pair. In his model, the cell pair voltage is calculated as the algebraic sum of voltage components (diffusion and membrane potentials) and voltage drops through the resistive elements of a cell pair (membranes, bulk solutions, diffusion boundary layers). The Nernst idealization of static boundary layers and completely mixed bulk solutions was adopted, while diffusion boundary layer thickness was taken from experimental data previously collected by the same author on electrodialysis experiments. The reported values are in the range of 130 – 30 μm, with a flow velocity increasing from 2 up to 20 cm/s, respectively. On the other hand, the electrodialysis units adopted for the experimental investigation had rather thick

compartments (640 μm), thus the highest values reported for the flow velocity cannot be taken into account for practical applications. Above all, three different factors were identified as crucial by Lacey for enhancing the process performance:

- The dilute compartment thickness, which should be as small as possible (~100 μm);
- Membrane resistance, preferably lower than 1 Ω cm^2;
- High salinity ratio (i.e. ratio between brine and dilute concentration), e.g. using 4 M – 0.1 M NaCl solutions.

The novelty of such work lies also in demonstrating that the RED process might be economically attractive, though the economic analysis performed is rather optimistic (a total cost of electricity of 0.043 $/kWh is estimated for a 20 MW RED plant operating with 4 M – 0.1 M NaCl solutions [70]).

Although Lacey's work presents several improvements in RED process modelling, it is still affected by strong simplifying assumptions in the estimation of physical properties of solutions (conductivity, activity coefficients). Moreover, the transport of solvent through membranes by osmosis/electro-osmosis is neglected.

Lacey's model was later modified by Brauns [71], and implemented in a solver software to investigate the effect of specific parameters on power output. In particular, Brauns analysed the possibility of using two different thicknesses for dilute/concentrate compartments, i.e. reducing the cell pair resistance by using a thinner diluate compartment thickness. A number of process parameters were investigated, such as membrane thickness, inlet solutions concentration and temperature. Brauns showed how the power output is largely affected by membrane thickness, demonstrating that the development of new thinner membranes can give a significant enhancement of process performance.

More recently, a new model for RED cell pair was proposed by Veerman *et al.* using river water and seawater [39]. In this work, the cell pair voltage is evaluated accounting for both mass balance within compartments and transport phenomena through membranes. Two significant phenomena are taken into account by the model: co-ions transport (i.e. transport of ions of the same type of fixed charges through membranes), and osmosis (solvent transport from dilute to concentrate compartment).

The model was calibrated through data from lab-scale stacks (10x10 cm^2 and 75x25 cm^2), using two different type of commercial membranes (homogeneous and heterogeneous).

Veerman suggested that a co-current flow is preferable inside the RED unit to avoid the risk of leakage for high local pressure difference. In fact, both the experimental and modelling results showed no significant difference between co-current and counter-current arrangement. Furthermore, he investigated the use of segmented electrodes, showing that an increase in power output (+11%) is obtainable by using a system with three electrodes [39].

The model proposed by Veerman *et al.* represents one of the most comprehensive work in the relevant literature. However, some of the assumptions, which are valid in the range of river water – seawater applications, cannot be applied to a higher range of salt concentration. For instance, it is well known that the use of constant equivalent conductivity, or the application of Debye-Hückel theory, are not reliable when salt concentration is higher than 0.5 M NaCl [72]. Moreover, such model is limited to a single cell pair, although an electric model was developed by the same author for estimating the effect of parasitic currents in another work [46].

Based on the literature review it seems clear how, although notable efforts have been done already in the development of models for the RED process, these works are only related to the use of river water and seawater as feed solutions, while none of them has considered the use of concentrated brines, which could dramatically affect the model formulation. Moreover, all presented approaches are based on a number of simplifying assumptions that could be overtaken by using a "multi-scale" approach [73], where different modelling scales are used to simulate different aspects of the process. In this way, both transport phenomena inside cells and electrical phenomena within the entire stack can be estimated by the model.

In this chapter, a novel model is proposed based on Veerman's approach, aiming to extend the previous model to a wider range of concentration, and develop a more general simulation tool for RED process.

3.2 Multi-scale modelling approach

One of the first steps of modelling is the choice of a scale of description for the system, according to the modelling goal and level of details reasonably achievable. Whenever the features of the system require more than one scale of description, different models may be adopted, building "a model hierarchy driven by characteristic sizes": such approach is called multi-scale modelling [73].

Multi-scale modelling is especially suitable for design and optimisation of chemical processes of noteworthy complexity, such as electrochemical processes. For this reason, a multi-scale modelling approach has been adopted for the RED system (Figure 2). According to this method, a lower-scale model describes the physical phenomena in a single repeating unit of the stack (*cell pair*). The second level of description refers to the whole equipment (*stack*), including all cell pairs and the relevant interconnections. Finally, a model for the whole plant has been implemented, allowing simulating more stacks interconnected with different layouts.

3.3 Model Development

The modelling goals are (i) reaching a comprehensive description of all the physical phenomena involved in the RED process and (ii) building a simulation tool for simulating the operation of a pilot plant. For these purposes, the model has been firstly developed at two different scales of description (Figure 3.1):

- A low-hierarchy scale (*cell pair*), outlining the physical phenomena inside the repeating unit of the RED system.
- A high-hierarchy scale (*stack*) for the entire equipment, describing the interaction among all cell pairs and providing information on the performance of the equipment.

The cell pair model proposed by Veerman *et al.* [39] for RED process with river/sea water was adopted as starting point for the lower scale modelling.

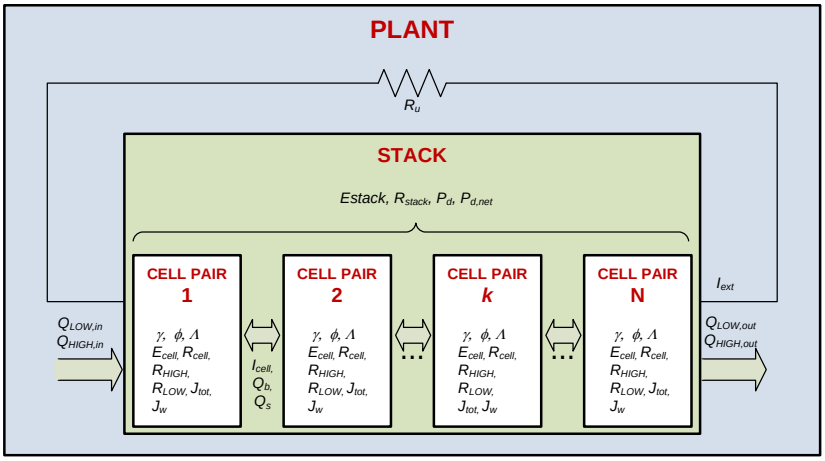

Figure 3.1. Structure of the proposed model.

A final model for the whole plant has been developed afterwards together with the process simulator, as will be explained in paragraph 3.4.

3.3.1 Low-hierarchy model (*cell pair*)

The modelling approach firstly focused on the repeating unit of the stack (*cell pair*, Figure 3.2). The following assumptions have been made:

- Feed streams are modelled as purely sodium chloride aqueous solutions, i.e. disregarding the other ions usually present in real seawater/brine.
- The computational domain is discretised only along the flow path length. This assumption initially allowed to reduce the model complexity: however, it has been removed later, in order to build a bi-dimensional model and simulate asymmetric stacks (paragraph 3.3.2).
- Parasitic currents within the circuit of the electrode rinse solution are negligible. This hypothesis is fully verified if the pipe used for the recirculation of the electrode rinse solution (acting as a salt bridge between anode and cathode compartment) is long enough, thus increasing the electric resistance in the hydraulic circuit [46].

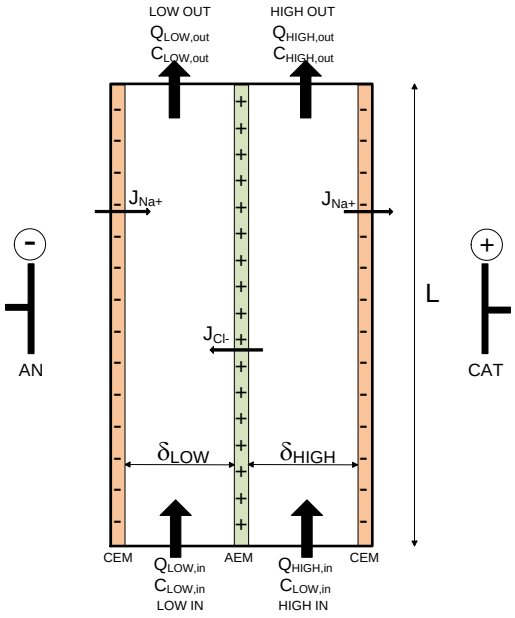

Figure 3.2. Repeating unit of a RED stack (*cell pair*). A cell pair is constituted by a Cation Exchange Membrane (CEM), a diluate (LOW) compartment, an Anion Exchange Membrane (AEM) and a concentrate (HIGH) compartment.

Since most of the process variables (both solution properties and electric variables) are functions of salt concentration, a distributed model has been implemented at this scale of description. In fact, all of these variables vary along the channel length because of the mass transport from concentrate to dilute compartment through membranes.

Thermodynamic properties of solutions

Salt concentration significantly affects the physical behaviour of electrolyte solutions, especially in the high concentration range. For this reason, the relevant thermodynamic properties of NaCl solutions were estimated through appropriate correlations from literature. In particular, both activity ($\gamma_{\pm}$) and osmotic (φ) coefficients were calculated using the virial equations proposed by Pitzer [74,75]:

$$ln\gamma_{\pm} = -A_1\left[\frac{\sqrt{I'}}{1+b'\sqrt{I'}} + \frac{2}{b'}ln\left(1+b'\sqrt{I}\right)\right] + mB^{\gamma} + m^2C^{\gamma} \tag{3.1}$$

$$\varphi - 1 = -A_1\frac{\sqrt{I}'}{1+b'\sqrt{I'}} + mB^{\varphi} + m^2C^{\varphi} \tag{3.2}$$

where I' and m are the ion strength and molality of the electrolyte, respectively; A_1 is the modified Debye-Hückel constant (A_1 = 0.3915 at 25°C), and b' is a correlation constant (b' =1.2 for 1:1-valence electrolyte). The other virial coefficients in eq. (3.1-3.2), i.e. B^{γ}, C^{γ}, B^{φ} C^{φ} are only functions of the nature of the electrolyte and have been already evaluated for the most common electrolytes. Their definitions are reported in the Appendix B.

The salt concentration affects also the equivalent conductivity of solutions; this term was estimated for both seawater and brine through a correlation proposed by Islam *et al.* [76]:

$$\Lambda(x) = \left[\Lambda^0 - \frac{B'_2(c)\sqrt{c}}{1+B'(c)a\sqrt{c}}\right]\left[1 - \frac{B'_1(c)\sqrt{c}}{1+B'(c)a\sqrt{c}}F'(c)\right] \tag{3.3}$$

where Λ^0 is the equivalent conductivity of NaCl at infinite dilution and c is the molar concentration. The other terms in eq. (3.3) (whose definition can be found in Appendix B), are functions of salt concentration and other solution properties, such as viscosity and dielectric constant. For these properties, a linear variation with the concentration was assumed, as well accepted in the literature [72].

The cell pair voltage arising across each membrane can be evaluated by the Nernst's equation [60]:

$$E_{cell}(x) = \alpha_{CEM}\frac{RT}{F}ln\frac{\gamma^{Na}_{HIGH}(x)C_{HIGH}(x)}{\gamma^{Na}_{LOW}(x)C_{LOW}(x)} + \alpha_{AEM}\frac{RT}{F}ln\frac{\gamma^{Cl}_{HIGH}(x)C_{HIGH}(x)}{\gamma^{Cl}_{LOW}(x)C_{LOW}(x)} \tag{3.4}$$

where R, T, and F have their usual meaning, α_{AEM}, α_{CEM} are the permselectivity of both IEMs [11], and the subscripts *HIGH* and *LOW* refer to concentrate and dilute solutions, respectively.

The electrical resistance of a single cell pair is given by the sum of the resistances through solutions and membranes:

$$R_{cell}(x) = R_{HIGH}(x) + R_{LOW}(x) + R_{CEM,eff} + R_{AEM,eff} \tag{3.5}$$

where R_{HIGH} and R_{LOW} are the electrical resistances of concentrate and diluate compartments, respectively; $R_{HIGH,eff}$ and $R_{LOW,eff}$ are the membranes resistance inside the stack. The solution resistances are evaluated as a function of salt concentration as:

$$R_{LOW}(x) = f_y \frac{\delta_{LOW}}{\Lambda_{LOW}(x) C_{LOW}(x)} \tag{3.6}$$

$$R_{HIGH}(x) = f_y \frac{\delta_{HIGH}}{\Lambda_{HIGH}(x) C_{HIGH}(x)} \tag{3.7}$$

where δ_{HIGH}, δ_{LOW} are the two compartments thicknesses and f_y (*shadow factor*) is a geometric constant which accounts for the increase of electrical resistance due to the presence of a non-conductive spacer inside the channels, as will be described in paragraph 3.3.2 .

When piled into a stack, membranes are in contact with two different solutions, which affect their electrical resistance. For this reason, the effective electrical resistance of membranes was evaluated as:

$$R_{AEM,eff} = f_m R_{AEM} \qquad R_{CEM,eff} = f_m R_{CEM} \tag{3.8,3.9}$$

where R_{CEM} and R_{AEM} are the IEMs nominal electrical resistance measured in standardised condition (in this case for 0.5 M NaCl and 4 M NaCl solutions at 25°C

in a six-compartments setup [62]), and f_m (*resistance correction factor*) is a correction factor to predict the actual resistances of membranes in process conditions, as will be discussed in paragraph 4.1.1.

It is worth noting that the current density through membranes, which is related to all cell pairs, has been declared in the higher hierarchy model (paragraph 3.3.2), in order to integrate the relevant equations also with the model for parasitic currents.

Salt transport through IEMs

In the ideal case of 100% selective membranes, only counter-ions (ions with opposite charge to the fixed ionic charges in the membrane) can pass through each IEM. In fact, a real IEM cannot completely reject co-ions (i.e. ions with the same sign as the fixed charges), especially when highly concentrated solutions are used. Therefore, in real conditions co-ions will also pass through membranes to some extent. The salt flux (expressed as NaCl molar flux per cell pair area) outgoing from a concentrate compartment to the closest dilute compartments is evaluated as the sum of counter-ion and co-ion transport through both IEMs [39]. Counter-ion flux can be related to the net ions flux related to the current density (Na^+ through the CEM and Cl^- through the AEM), plus the counter-ion flux coupled with co-ions flux, which, conversely, do not generate any net electrical current (being related to the movement of a neutral salt). This can be expressed as the total salt flux according to:

$$J_{tot}(x) = \frac{j(x)}{F} + 2\frac{D_{NaCl}}{\delta_m}\left[C_{HIGH}(x) - C_{LOW}(x)\right] \tag{3.10}$$

where j is the ionic current density, δ_m is IEMs thickness (assumed as equal for AEM and CEM) and D_{NaCl} is the salt permeability coefficient. The factor 2 accounts for the two IEMs in a cell pair. Regarding the coupled counter/co-ion flux, the salt permeability coefficient (D_{NaCl}) has been set to a constant value of 10^{-12} m^2/s from literature [39]. However, this assumption does not affect the process performance in a range of variation of two order of magnitudes (as will be shown in Figure 4.3).

Water transport through membranes

The water transport through membranes is due to two opposite contributions: (i) the osmotic flux (opposite to the salt flux) and (ii) the electro-osmotic flux, in the direction of salt transport and essentially due to the solvent molecules firmly bound in hydration shells. The first term was estimated evaluating the real osmotic pressure difference across each membrane:

$$J_{osm}(x) = -2 L_p \Delta\Pi^* = -2 L_p \left[\nu R T \left(\varphi_{HIGH} C_{HIGH}(x) - \varphi_{LOW} C_{LOW}(x) \right) \right] \quad (3.11)$$

where L_p is the water permeability coefficient of IEMs, $\Delta\Pi^*$ is the real osmotic pressure difference and φ_{HIGH}, φ_{LOW} are the osmotic coefficients for concentrate and dilute solution, respectively (eq. (3.2)).

The electro-osmotic flux was calculated assuming a total hydration number (n_h) for Na^+ and Cl^- of 7, as reported in the literature [72]:

$$J_{eosm}(x) = n_h J_{tot}(x) \quad (3.12)$$

Therefore, the net water transport through membranes is given by

$$J_w(x) = J_{osm}(x) + J_{eosm}(x) \quad (3.13)$$

It is worth noting that J_{osm} has been defined as a negative flux (eq. (3.11)), therefore the net water flux (J_w) in eq. (3.13) is an algebraic sum of two opposite contributions.

Mass balance in dilute-concentrate compartments

Mass balances for NaCl in both compartments have been developed taking into account also the effect of solvent transport on salt concentration [39]:

$$\frac{dC_{LOW}(x)}{dx} = \frac{b}{Q_{LOW}} J_{tot}(x) - C_{LOW}(x) \frac{b}{Q_{LOW}} J_w^{'}(x) \tag{3.14}$$

$$\frac{dC_{HIGH}(x)}{dx} = -\frac{b}{Q_{HIGH}} J_{tot}(x) + C_{HIGH}(x) \frac{b}{Q_{HIGH}} J_w^{'}(x) \tag{3.15}$$

where Q_{HIGH}, Q_{LOW} are the solution flow rates in each compartment, b is the membrane width, and J'_w is the volumetric flux of solvent through membranes (i.e. the molar flux from eq. (3.13), J_w, multiplied by the water molar density). Since the osmotic flux is higher than the electro-osmosis in these process conditions (i.e. using brine as concentrated solution), the net water flux is opposite to the salt flux, giving a further reduction of concentration in the concentrate compartment, as well as an increase in the dilute compartment.

Concentration polarisation phenomena

Following the cell pair voltage definition in eq. (3.4), the potential difference arising across each membrane depends on the actual salt concentration on membrane surface. Therefore, eq. (3.4) can be rewritten as:

$$E_{cell}(x) = (\alpha_{CEM} + \alpha_{AEM}) \frac{RT}{F} ln \left[\frac{\gamma_{HIGH}^{int}(x) C_{HIGH}^{int}(x)}{\gamma_{LOW}^{int}(x) C_{LOW}^{int}(x)} \right] \tag{3.16}$$

where c^{int} is the actual salt concentration at membrane-solution interface, γ^{int} is the mean activity coefficient of NaCl evaluated at interface concentration; subscripts *HIGH* and *LOW* refer to concentrate and dilute solutions, respectively. Note that the two terms on the right-hand side of eq. (3.4) have been lumped together since the system contains only one symmetric electrolyte ($\gamma_+ = \gamma_- = \gamma_\pm$).

Polarisation phenomena lead to a change of the salt concentration at membrane-solution interface with respect to the bulk conditions. This is due to the ion transport through the membranes, which requires the same ions transport between the channel bulk and the interface. Therefore, such transport phenomena are related to the

generation of a gradient between bulk and interface, leading (in the case of RED process) to a reduction of the salt concentration on the HIGH-side and increase of the salt concentration on the LOW-side of each membrane (Figure 3.3). As a result, the overall effect is a reduction of the available driving force for electric potential, which can be quantified defining "polarisation coefficients" as [77]:

$$\vartheta_{HIGH} = \frac{C_{HIGH}^{int}}{C_{HIGH}^{bulk}} \qquad \vartheta_{LOW} = \frac{C_{LOW}^{bulk}}{C_{LOW}^{int}} \qquad (3.17,3.18)$$

These coefficients can be seen as a measure of the effect of polarisation phenomena on the available driving force for the RED process (note that both θ_{HIGH} and θ_{LOW} are defined to be always ≤ 1).

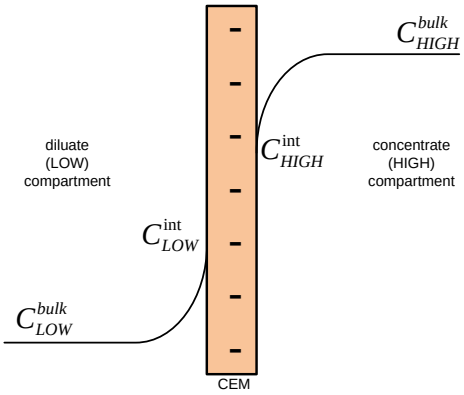

Figure 3.3. Schematic representation of concentration profiles close to a cationic membrane surface.

Substituting eq. (3.17,3.18) into eq. (3.16), the cell pair voltage becomes

$$E_{cell}(x) = (\alpha_{CEM} + \alpha_{AEM}) \frac{RT}{F} ln \left[\vartheta_{HIGH}\, \vartheta_{LOW} \frac{\gamma_{HIGH}^{int}(x) C_{HIGH}^{bulk}(x)}{\gamma_{LOW}^{int}(x) C_{LOW}^{bulk}(x)} \right] \qquad (3.19)$$

In order to calculate the polarisation coefficients, eq. (3.17,3.18) can be also written as:

$$\vartheta_{HIGH} = \frac{C_{HIGH}^{int}}{C_{HIGH}^{bulk}} = \frac{C_{HIGH}^{bulk} - \Delta C_{HIGH}^{*}}{C_{HIGH}^{bulk}} \tag{3.20}$$

$$\vartheta_{LOW} = \frac{C_{LOW}^{bulk}}{C_{LOW}^{int}} = \frac{C_{LOW}^{bulk}}{C_{LOW}^{bulk} + \Delta C_{LOW}^{*}} \tag{3.21}$$

where ΔC^{*}_{HIGH}, ΔC^{*}_{LOW} are the concentration drops in the diffusion boundary layer for concentrate and dilute solutions, respectively. These quantities depend on the ionic flux through membranes (i.e. on the current density), as well as on the flow velocity inside channels. ΔC^{*}_{HIGH}, ΔC^{*}_{LOW} values were predicted by means of Computational Fluid Dynamics (CFD) simulations in a wide range of different operating conditions in order to get all the information necessary to implement eqs. (3.17)-(3.21) in the present model formulation (Figure 3.4) [12,77].

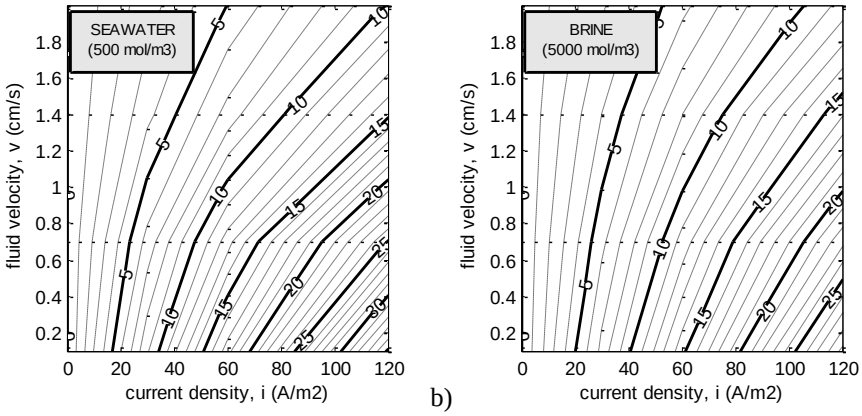

Figure 3.4. Effect of current density and fluid velocity on the concentration drop in diffusion boundary layer (mol/m^3). Case a) seawater (0.5 M NaCl); case b) brine (5 M NaCl). Model predictions from CFD simulations with 270 μm polyamide woven spacer (Deukum GmbH, Germany) [12,77].

The fluid velocity (v) in Figure 3.4 is defined as the mean feed flow velocity inside the spacer-filled channel and is equal to:

$$v = \frac{Q}{\delta b \varepsilon_{sp}} \tag{3.22}$$

where Q is the volumetric flow rate, δ is the spacer thickness, b is the channel width and ε_{sp} is the spacer porosity.

The concentration drop in the diffusion boundary layer (DBL) was estimated adding the correlations derived from CFD simulations (Figure 3.4) to the proposed model. Therefore, both polarisation coefficients were calculated by eq. (3.20)-(3.21) (Figure 3.5).

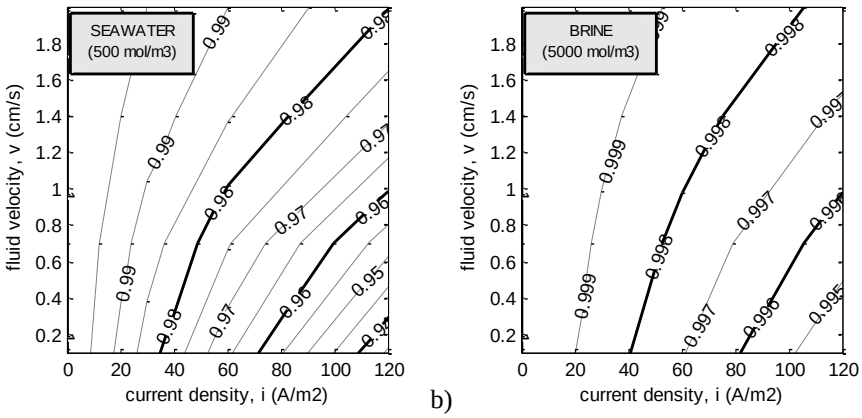

a) b)

Figure 3.5. Effect of current density and fluid velocity on polarisation coefficients. Case a) seawater (0.5 M NaCl); case b) brine (5 M NaCl). Model predictions from CFD simulations with 270 μm polyamide woven spacer (Deukum GmbH, Germany) [12,77].

It is worth noting that the concentration drop in DBL is similar for both solutions (Figure 3.4), with only slightly larger values predicted for the dilute solution (Figure 3.4.a). On the other hand, the higher bulk concentration for the brine solution gives rise to a polarisation coefficient close to unity, i.e. negligibly affecting the cell potential (Figure 3.5.b).

3.3.2 High-hierarchy model (*stack*)

In the "stack" model, the system is constituted by a series of N cell pairs and two electrode compartments at the ends (Figure 3.1). The modelling goal at this level of

description is to describe the interactions among the repeating units of the system in terms of electrical behaviour, pressure drops and overall performance. Unlike the cell pair, which is modelled as a distributed system, in this section the system has been modelled as a lumped system, averaging each variable in the flow direction.

Cell pair current density and parasitic currents through manifolds

The electric current collected by an external load is related to the ionic current, i.e. the ions transport through membranes driven by the salinity gradient. However, other "shortcut" paths can be imagined for ions to flow from high potential to low potential compartments. For instance, inlet and outlet manifolds act as salt bridges among cell pairs, allowing ions to flow through manifolds instead of membranes. Such currents represent in fact a dissipation of the electrical energy generated inside the system. The effect of parasitic currents may be described assuming an equivalent electrical circuit for the RED system, in which the cell pair is assumed as the repeating energy generation unit (including an "internal resistance"), while compartments and manifolds are the secondary electrical circuits. A graphical representation of the electrical circuit here adopted is shown in Figure 3.6, based on the circuit proposed by Veerman *et al.* [46].

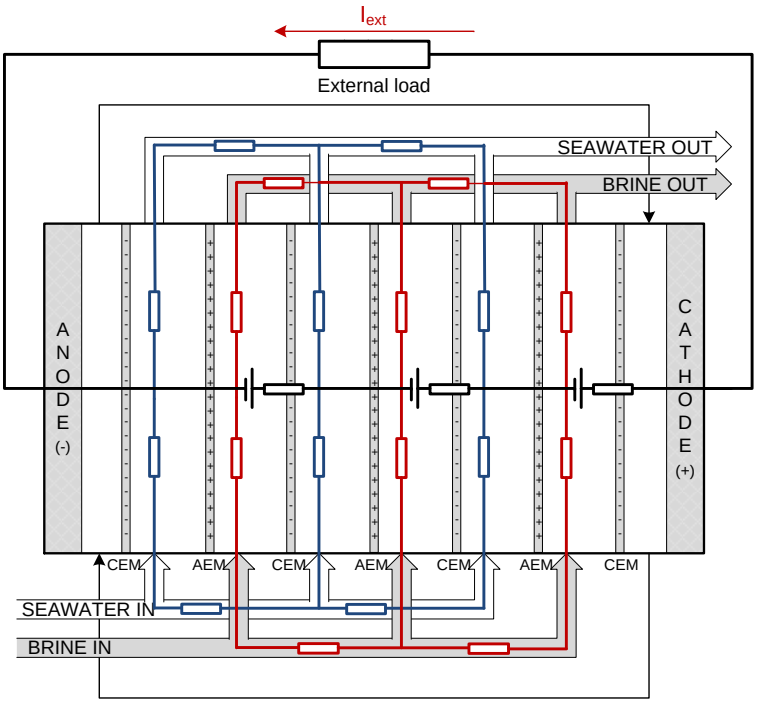

Figure 3.6. Equivalent circuit for parasitic currents in inlet/outlet manifolds and compartments. Black: main circuit; blue: parasitic currents in dilute solution (seawater) manifolds; red: parasitic currents in concentrate solution (brine) manifolds.

As shown in Figure 3.6, the parasitic currents in both compartments have been taken into account in the developed model. The electrical resistance inside a generic *k*-th channel is evaluated by the following terms (Figure 3.7):

- electric resistance in HIGH/LOW solutions distributors (i.e. inlet manifolds):

$$R_{HIGH}^{d} = \frac{\delta_{tot}}{\left(\Lambda_{HIGH} C_{HIGH}\right)_{x=0} S_d} \tag{3.23}$$

$$R_{LOW}^{d} = \frac{\delta_{tot}}{\left(\Lambda_{LOW} C_{LOW}\right)_{x=0} S_d} \tag{3.24}$$

where δ_{tot} is the total distributor length between two subsequent compartments ($\delta_{tot} = \delta_{HIGH} + \delta_{LOW} + 2\ \delta_m$) and S_d is the cross-sectional area of the distribution channels, supposed as a rectangular channel.

- electric resistance in HIGH/LOW solutions collectors (outlet manifolds):

$$R^c_{HIGH,k} = \frac{\delta_{tot}}{\left(\Lambda^c_{HIGH,k}\, C^c_{HIGH,k}\right) S_c} \tag{3.25}$$

$$R^c_{LOW,k} = \frac{\delta_{tot}}{\left(\Lambda^c_{LOW,k}\, C^c_{LOW,k}\right) S_c} \tag{3.26}$$

In the equations above, S_c is the cross-sectional area of collectors. The electrical resistance for the generic *k*-th compartment is a function of the salt concentration inside the collector ($C^c_{HIGH,k}$, $C^c_{LOW,k}$). This concentration can be estimated by a mass balance between two subsequent compartments:

$$Q^c_{HIGH,k} = Q_{HIGH,k} + Q^c_{HIGH,k+1} \tag{3.27}$$

$$Q^c_{LOW,k} = Q_{LOW,k} + Q^c_{LOW,k+1} \tag{3.28}$$

Rearranging the eq. 3.27-3.28, the concentration inside the collector at the outlet of the *k*-th compartment is given by

$$C^c_{\mathrm{HIGH},k} = \frac{C_{\mathrm{HIGH},k}\, Q_{\mathrm{HIGH},k} + C^c_{\mathrm{HIGH},k+1}\, Q^c_{\mathrm{HIGH},k+1}}{Q_{\mathrm{HIGH},k} + Q^c_{\mathrm{HIGH},k+1}} \tag{3.29}$$

$$C^c_{LOW,k} = \frac{C_{LOW,k}\, Q_{LOW,k} + C^c_{LOW,k+1}\, Q^c_{LOW,k+1}}{Q_{LOW,k} + Q^c_{LOW,k+1}} \tag{3.30}$$

In order to take into account the concentration change along compartments, the relevant electric resistances were split in two contributions, investigating the

difference from inlet ($x = 0$) to the centre ($x = L/2$), and from the centre to the outlet ($x = L$):

$$R'_{\mathrm{HIGH},k} = f_x \frac{L/2}{\left(\overline{\Lambda}'_{\mathrm{HIGH},k}\,\overline{C}'_{\mathrm{HIGH},k}\right) b\,\delta_{\mathrm{HIGH}}} \tag{3.31}$$

$$R'_{LOW,k} = f_x \frac{L/2}{\left(\overline{\Lambda}'_{LOW,k}\,\overline{C}'_{LOW,k}\right) b\,\delta_{LOW}} \tag{3.32}$$

$$R''_{\mathrm{HIGH},k} = f_x \frac{L/2}{\left(\overline{\Lambda}''_{\mathrm{HIGH},k}\,\overline{C}''_{\mathrm{HIGH},k}\right) b\,\delta_{\mathrm{HIGH}}} \tag{3.33}$$

$$R''_{s,k} = f_x \frac{L/2}{\left(\overline{\Lambda}''_{s,k}\,\overline{C}''_{s,k}\right) b\,\delta_{s}} \tag{3.34}$$

In these equations, $\overline{\Lambda}'_{HIGH,k}$, $\overline{C}'_{HIGH,k}$, $\overline{\Lambda}'_{LOW,k}$, $C'_{HIGH,k}$ are mean variables evaluated between inlet-centre, while $\overline{\Lambda}''_{HIGH,k}$, $\overline{C}''_{HIGH,k}$, $\overline{\Lambda}''_{LOW,k}$, $C''_{HIGH,k}$ are evaluated between centre and outlet; f_x is a shadow factor calculated from the spacer open area in the flow direction, as will be explained in detail in the following paragraph.

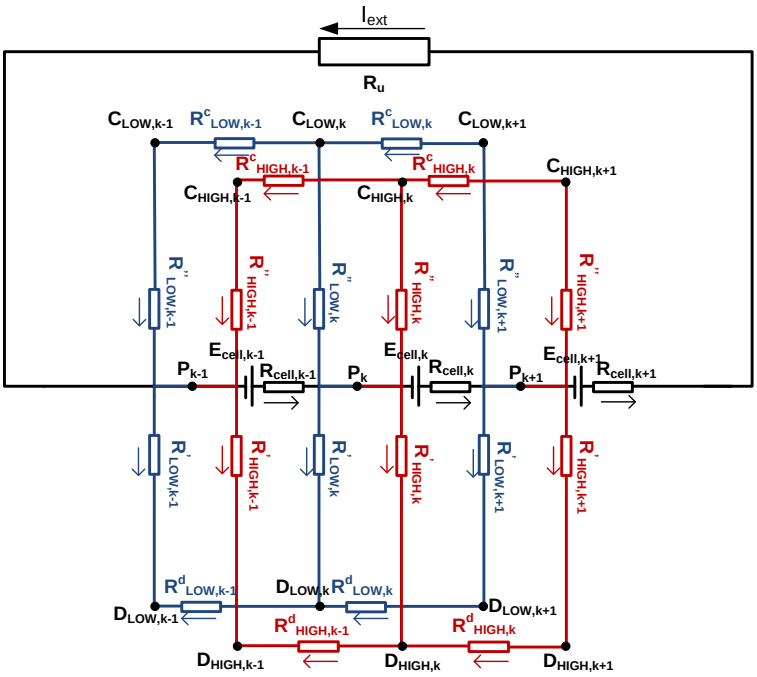

Figure 3.7. Equivalent circuit and electrical variables adopted for the prediction of parasitic currents in inlet/outlet manifolds and compartments.

Once the resistances shown in Figure 3.7 have been declared, all currents within cell pairs can be evaluated by Kirchhoff's law (eq. (3.35)) in the nodes (P_k, $D_{s,k}$, $D_{b,k}$, $C_{s,k}$, $C_{b,k}$) and Ohm's law (eq. (3.36)) over all the resistances.

$$\sum_k I_k = 0 \qquad\qquad R_k = \frac{\Delta V_k}{I_k} \qquad (3.35,3.36)$$

It is worth noting that, in the equivalent electrical circuit (Figure 3.7), the concentrate and dilute compartments converge towards a single node (P_k). This is, of course, not related to the real hydraulic circuits (the two channels are not converging into a common central point), yet it is a simplification of the electrical circuit for predicting the cell pair current and parasitic currents phenomena.

Evaluation of the spacer shadow effect

The electrical resistances of dilute and concentrate solutions perpendicular to the membrane have been calculated by eq. (3.7), while the resistances along the channel are described in eq. (3.31)-(3.34). The open area of a specific spacer, which increases the electrical resistance, may be different in the direction perpendicular/parallel to the membrane (Figure 3.8). For this reason, two different shadow factors have been defined, based on the geometric features of the spacer:

$$f_x = \frac{1}{a_{open,x}} \qquad f_y = \frac{1}{a_{open,y}} \qquad (3.37,3.38)$$

Both $a_{open,x}$ and $a_{open,y}$ vary between a certain minimum value (i.e. on a plane containing the centre of filaments) and 100% (on a plane tangent to the filaments surface), while typical values for commercial spacers are 40-60%. This variation was taken into account assuming an average value for $a_{open,x}$ and $a_{open,y}$.

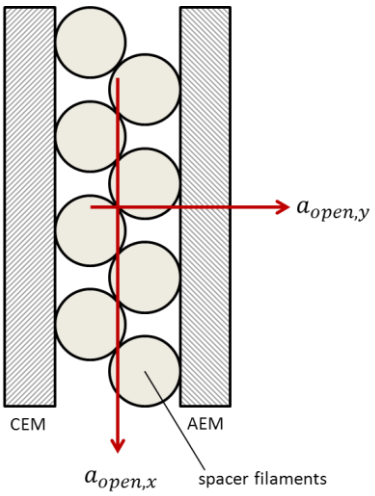

Figure 3.8. Spacer open area in direction perpendicular/parallel to the membrane.

Stack voltage and power density

The total stack resistance may be evaluated as:

$$R_{stack} = \left(\sum_{i=1}^{N} \bar{R}_{cell,\,i} \right) + R_{blank} \tag{3.39}$$

where R_{blank} is the resistance in the electrode compartments, estimated from experimental measurements.

The stack voltage is equal to the sum of all the electromotive force generated across each membrane pair (E_{cell}) minus the potential drops due to the internal cell resistance (for each cell pair) and the electrode compartments resistance:

$$\bar{E}_{stack} = \sum_{i=1}^{N} \left(\bar{E}_{cell,i} - \bar{R}_{cell,i} \frac{\bar{I}_{cell,i}}{A} \right) - R_{blank} \frac{I_{ext}}{A} \tag{3.40}$$

where $I_{cell,i}$ is the electric current flowing in the cell pair and I_{ext} is the electrical current collected in the external load, given by:

$$I_{ext} = \frac{\bar{E}_{stack}}{R_u} A \tag{3.41}$$

In eq. (3.41), R_u is the external load of the system (assumed as constant), multiplied by the cell pair area in order to be expressed in $\Omega\ m^2$, as all the other areal resistances defined within the model.

Finally, the specific power per cell pair area (power density) is evaluated as:

$$P_d = \frac{1}{N} \left(\frac{I_{ext}}{A} \right)^2 R_u \tag{3.42}$$

It is worth noting that the above defined power density refers to m^2 of cell pair, while in some other literature works it is defined per m^2 of total membrane.

Pressure drops

Pressure drops for the salt solutions inside the stack can be split into two main contributions:

- *Concentrated pressure drops*, related to the manifolds and inlet/outlet sections of each compartment; this term is strongly dependent on both stack and spacer geometry (for inlet/outlet drops).
- *Distributed pressure drops*, which depend on the spacer geometry and are typically proportional to the flow velocity (assuming a laminar flow regime).

A detailed analysis of the fluid flow behaviour inside spacer-filled channels using Computational Fluid Dynamics (CFD) modelling has been already presented by Gurreri *et al.* [12] and is beyond the scope of the present thesis. However, in order to estimate the pressure drops and evaluate the required pumping power, both distributed and concentrated pressure drops for diluate and concentrate were experimentally measured [77] inside a channel filled with a 270 µm polyamide woven spacer (Deukum GmbH, Germany) (Figure 3.9). The regression laws from fitting of the experimental data at different fluid velocity were added to the model.

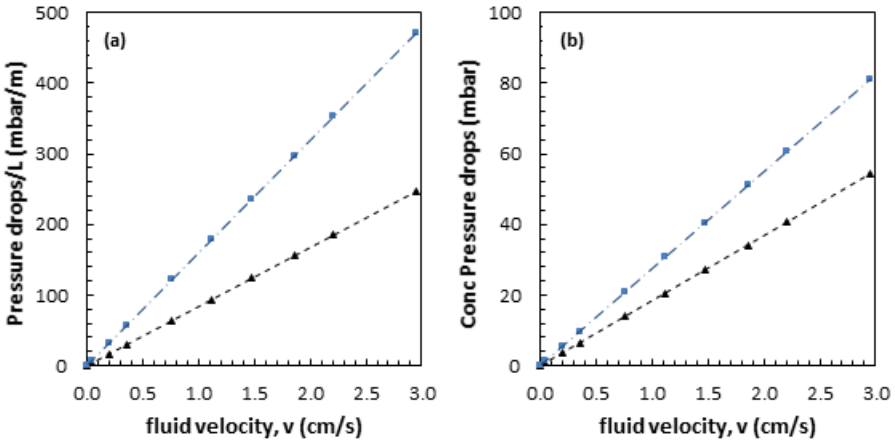

Figure 3.9. Distributed (a) and concentrated (b) pressure drops for a channel filled with 270 µm polyamide woven spacer. Experimental measurements performed inside a single channel using pure water (▲) and 4 M NaCl solution as brine (■).

The required power for pumping the salt solutions through the stack is calculated by:

$$P_{pump} = \frac{\Delta P_{HIGH}\, Q_{HIGH}^{tot} + \Delta P_{LOW}\, Q_{LOW}^{tot}}{\eta_p} \tag{3.43}$$

where Δp is the total pressure drop, Q^{tot} is the flow rate of both solutions, and η_p is pump efficiency (set by default to 75%); subscripts *HIGH* and *LOW* refer to concentrate and dilute solution, respectively.

Finally, the performance of the RED process can be evaluated through the net power density, i.e. the obtainable electric power normalised for the cell pair area after the subtraction of the pumping power:

$$P_{d,net} = P_d - \frac{P_{pump}}{N\,A} \tag{3.44}$$

It is worth noting that in eq. (3.44) the pumping power (P_{pump}) has been divided by the cell pair area ($N\,A$) to be dimensionally consistent with the power density.

3.4 Development of a process simulator

The final set of equations (eq. (3.1)-(3.44)) was implemented into an equation-based solver software to build a simulator for RED process. With this regard, gPROMS Model Builder (Process System Enterprise Ltd, UK) was adopted as modelling tool. Such software allows to add user-defined equations, providing also a built-in flowsheeting environment, similar to the common software used in process system engineering.

The flowsheet for the main section of a RED plant implemented within gPROMS environment is shown in Figure 3.10. This section includes the RED unit, plus two feed pumps for salt solutions and the electrical connection of the system to the external load. A graphical user interface was developed, allowing the user to define

design/operating conditions for the process, in order to simulate a number of possible scenarios.

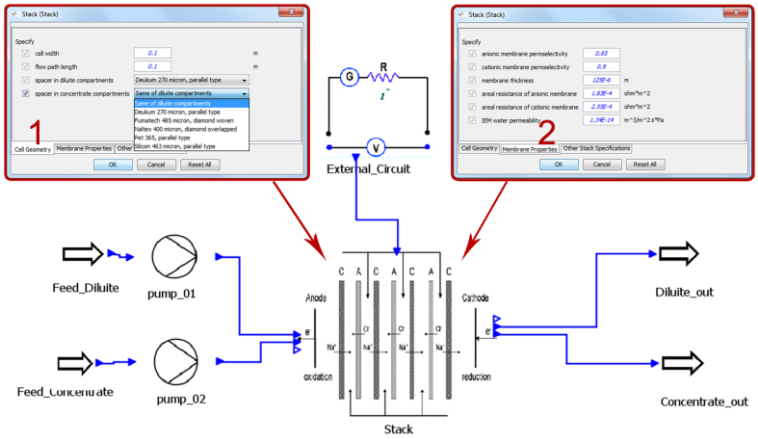

Figure 3.10. Graphical User Interface (GUI) of the developed process simulator on gPROMS 3.6. Two dialog boxes for the stack specifications are shown as example.

In particular, the specifications for the RED stack were divided into the following tabs:

- *Cell Geometry*: width, length, spacer thickness for both compartments; by default, the same spacer is used for both compartments, although different spacers can be specified among a list of commercial spacers.
- *Membrane Properties*: permselectivity, resistance, hydraulic permeability. Values of Fujifilm membranes (AEM 80045-01/CEM 80050-04) were set as default.
- *Other Stack Specifications*: number of cell pairs, distributor/collector thickness and geometry (different for co-current/cross-flow arrangements).

The required computational time depends on the size of the stack (i.e. the membrane size and the number of cell pairs specified by the user) and the machine power. For instance, the simulation of a stack with 100 cells required about 10-15

minutes on a machine equipped with Microsoft® Windows® XP Professional (SP3) - Intel® Core™2 Duo Processor E6600, 2.40 GHz, 3 GB RAM.

The developed model has been validated with experimental data collected on laboratory-scale unit, and then adopted for a wide theoretical analysis, as will be described in detail in the next chapter.

4 MODEL PREDICTIONS AND RESULTS*

Abstract

The proposed model has been validated against original experimental data and then used to investigate the influence of the main operating factors on power output. A good matching was found between predictions and experiments for a wide range of inlet concentrations, flow rates and feed temperatures.

For the investigated system, optimal feed conditions have been found employing brackish water (0.08-0.1 M NaCl) as diluate and brine (4.5-5 M NaCl) as concentrate to generate the highest power density at 40°C temperature.

The use of asymmetric stack has been addressed, being the model able to simulate different flow path lengths for dilute and concentrate streams. Increasing the aspect ratio from 1 (i.e. 20x20 cm^2 symmetric stack) up to 5 (20x100 cm^2 stack), a decrease from 7% to 20% in the power density is registered, with larger effects observed when increasing the diluate channel length.

The model can be used to explore the full potential of the RED technology, especially for any investigation regarding the future scale-up of the process.

* Part of this chapter has been published in revised form as:

- M. Tedesco, A. Cipollina, A. Tamburini, I. D. L. Bogle, G. Micale, *A simulation tool for analysis and design of Reverse Electrodialysis using concentrated brines*, Chem. Eng. Res. Des., 93 (2015) 441–456.
- M. Tedesco, P. Mazzola, A. Tamburini, G. Micale, I. D. L. Bogle, M. Papapetrou, A. Cipollina, *Analysis and simulation of scale-up potentials in reverse electrodialysis*, Desalination and Water Treatment (2014), doi:10.1080/19443994.2014.947781.

4.1 Model calibration and validation procedure

The experimental data used for model validation were collected during an extensive experimental campaign performed at VITO (Flemish Institute for Technological Research, Mol – Belgium), as will be described in Chapter 5. A newly designed lab-scale stack with 10x10 cm^2 of active membrane area and equipped with 50 cell pairs (REDstack BV, The Netherlands) was used for this purpose. The RED unit was designed with a cross-flow configuration to improve the flow distribution inside channels and reduce the effect of parasitic currents through the manifolds. It is worth noting that, although the model has been implemented for a co-current flow distribution, the experimental data collected with the cross-flow stack can be effectively used for calibration. In fact, given the small residence time and negligible variation of streams properties along compartments, no significant difference can be found between the two operating configurations [39].

The electrode compartments consisted of two Ru-Ir mixed metal oxide electrodes (Magneto Special Anodes BV, The Netherlands) rinsed by a 0.1 M $K_3Fe(CN)_6$ + 0.1 M $K_3Fe(CN)_6$ aqueous solution with 2.5 M NaCl as supporting electrolyte. These species give good performance and high stability under the operating conditions of the RED process [35,47].

The stack was equipped with a 270 µm polyamide woven spacer (Deukum GmbH, Germany) and Fujifilm ion-exchange membranes (Fujifilm Manufacturing Europe BV, The Netherlands). Those membranes were purposely developed for highly concentrated salt solutions. The relevant physical properties of IEMs are listed in Table 4.1.

Peristaltic pumps (Hosepump Masterflex PW, Burt Process Equipment Inc., USA) were used for circulating both salt solutions, as well as the electrode rinse solution. Experimental measurements were carried out using a galvanostat (Autolab PGSTAT100, Metrohm, USA). The salt solutions were made using distillate water and technical grade NaCl (ESCO, The Netherlands).

Table 4.1. Physical properties of Fujifilm ion exchange membranes*.

Membrane	Thickness, μm	Permselectivity (0.5 M - 4 M)	Hydraulic permeability, ml/bar h m^2
AEM 80045-01	120	0.65	4.96
CEM 80050-04	120	0.90	4.72

* Data provided by the membrane manufacturer.

4.1.1 Definition and calibration of tuning parameters

The procedure adopted for the model tuning is sketched in Figure 4.1. During the experimental measurements, the galvanostat imposed a constant value for the external current, thus measuring the corresponding stack voltage. The same values of current has been set as input data for the model: therefore, the process simulator calculates the values of the tuning parameters that minimise the discrepancy between model predictions and experiments using a robust objective function (*Maximum Likelihood estimation* [78]).

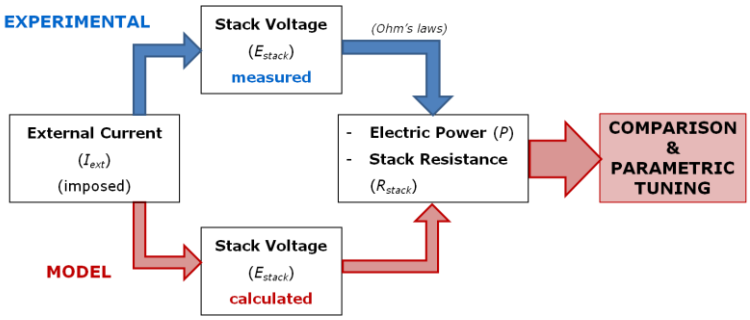

Figure 4.1. Logic scheme of the procedure adopted for model validation.

The tuning parameters were selected in order to evaluate the membrane properties under different feed concentration conditions. In particular, two different parameters were used:

- Permselectivity correction factor (β):

$$E_{cell}(x) = \beta\left(\alpha_{CEM} + \alpha_{AEM}\right)\frac{RT}{F} ln\left[\vartheta_{HIGH}\,\vartheta_{LOW}\,\frac{\gamma_{HIGH}(x)C_{HIGH}(x)}{\gamma_{LOW}(x)C_{LOW}(x)}\right] \quad (4.1)$$

  defined to take into account non-ideal behaviour of the system in terms of cell pair voltage (e.g. the effect of high salt concentration on IEM permselectivity).
- *Resistance correction factor (f_m)*: this factor accounts for the effect of solutions concentration on IEMs. Therefore, the effective IEMs resistances were evaluated as:

$$R_{AEM,eff} = f_m R_{AEM} \qquad R_{CEM,eff} = f_m R_{CEM} \quad (4.2,4.3)$$

Finally, a parametric variation study was performed, in order to investigate the dependence of β and f_m on the two solutions concentration. Experimental measurements carried out changing the diluate/concentrate concentration (Table 4.2) were used for the model calibration, in order to find the effect of salt concentration on the tuning parameters. The overall input data used for model calibration are reported in Table 4.2.

A parametric variation study was performed using the aforementioned parameters, in order to register the variation of these parameters with salt concentration. As a result, the following correlations were found, expressing the tuning parameters as a linear function of the inlet concentration for both solutions:

$$\beta = 1.212 - 0.281 C_{LOW} - 0.086 C_{HIGH} \quad (4.4)$$

$$f_m = 0.850 - 0.091 C_{LOW} - 0.052 C_{HIGH} \quad (4.5)$$

Finally, eq. (4.1-4.5) were added to the model, in order to reach a final comparison with the experimental results (Figure 4.2).

Table 4.2. Parameters used for model calibration.

	Parameter	**Unit**	**Value**
cell pair	Number of cell pairs, N	-	50
	membrane width, b	cm	9.5
	membrane length, L	cm	9.5
solutions	HIGH inlet concentration, C_{HIGH}	mol/l	1 – 5 M
	LOW inlet concentration, C_{LOW}	mol/l	0.1 – 1 M
	feed flow velocity, single channel	cm/s	1
membranes	CEM permselectivity, α_{CEM}	-	0.9
	AEM permselectivity, α_{AEM}	-	0.65
	CEM resistance, R_{CEM}	$\Omega \cdot cm^2$	2.96
	AEM resistance, R_{AEM}	$\Omega \cdot cm^2$	1.55
	AEM-CEM thickness, δ_m	µm	125
	AEM-CEM water permeability, L_p	$ml/bar \cdot h \cdot m^2$	4.84
spacer	spacer thickness, δ	µm	270
	mesh opening	µm	600
	wire diameter	µm	150
	open area, in direction perpendicular to membrane	-	0.64
	open area, in direction along to membrane	-	0.36
	relative spacer volume	-	0.175
	shadow factor perpendicular to membrane, f_y	-	1.212
	shadow factor along membrane, f_x	-	1.471

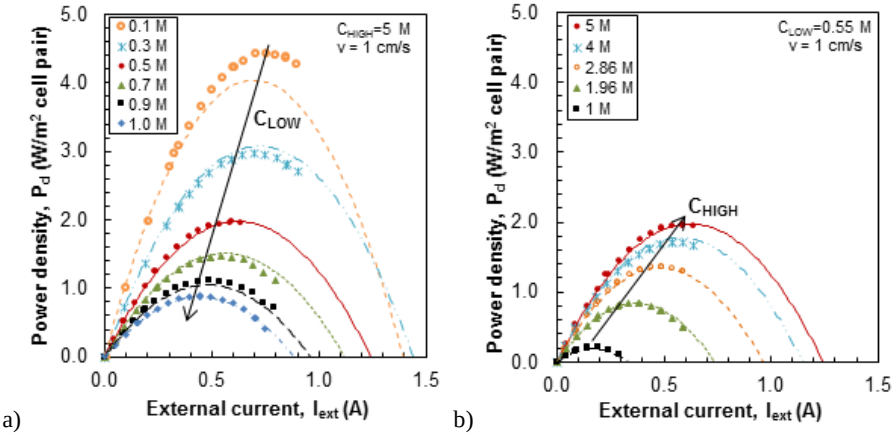

Figure 4.2. Effect of the inlet concentration on power density. Experimental (points) and simulated (lines) data for a 50 cell pairs stack equipped with Fujifilm membranes, 270 μm woven spacers. Feed flow velocity: 1 cm/s; T = 20°C. Case a) changing LOW concentration (C_{HIGH} = 5 M NaCl); case b) changing HIGH concentration (C_{LOW} = 0.55 M NaCl).

The good accordance between experimental and predicted data in Figure 4.2 shows that the model can be used as a predictive tool in a wide range of salt concentration. Therefore, a further validation step has been carried out under different conditions of feed flow rates and feed temperature.

Regarding the assumption of a constant value of NaCl permeability coefficient (D_{NaCl}), the sensitivity of the model towards this parameter has been investigated in order to assess how such a choice could affect the model reliability and robustness. Model output within a wide range of variation of D_{NaCl} (from 10^{-13} up to 10^{-11} m^2/s) was analysed, for fixed standard operating conditions (Figure 4.3).

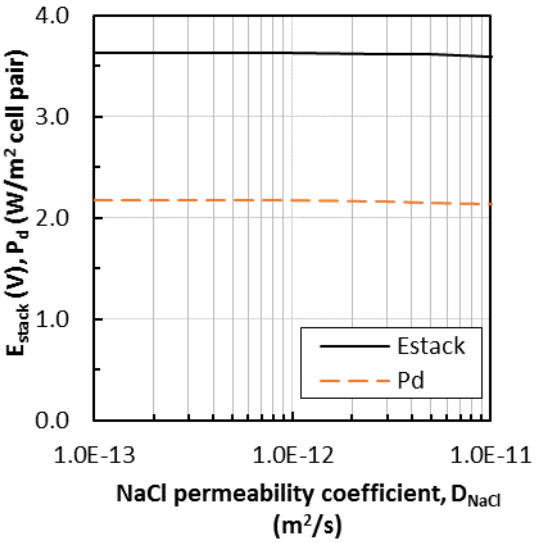

Figure 4.3. Effect of NaCl permeability coefficient on stack voltage and power density. Simulations of a 50 cell pairs stack equipped with Fujifilm membranes, 270 μm woven spacers. C_{HIGH} = 5 M; C_{LOW} = 0.5 M; feed flow velocity: 1 cm/s.

Figure 4.3 shows how model predictions are not affected by the variation of D_{NaCl}, even within the two orders of magnitude range of variation investigated. As a result, fixing the value of $D_{NaCl} = 10^{-12}$ m^2/s is a reliable assumption, which does not affect the model prediction capability. This is in accordance with physical expectations, as in such highly permselective IEMs, diffusion phenomena of co-ions are normally "minor" transport phenomena compared to the dominant transport phenomena of counter-ions.

4.2 Influence of feed flow rate

The effect of feed flow rates on process performance has been investigated, comparing model results with collected experimental information. In agreement with experiments, a concentration of 0.5 M NaCl and 5 M NaCl has been chosen for dilute and concentrated streams, respectively. Figure 4.4 shows the model predictions for the maximum power density achieved as a function of feed flow velocity inside a

single compartment, as well as the experimental results collected in the same conditions.

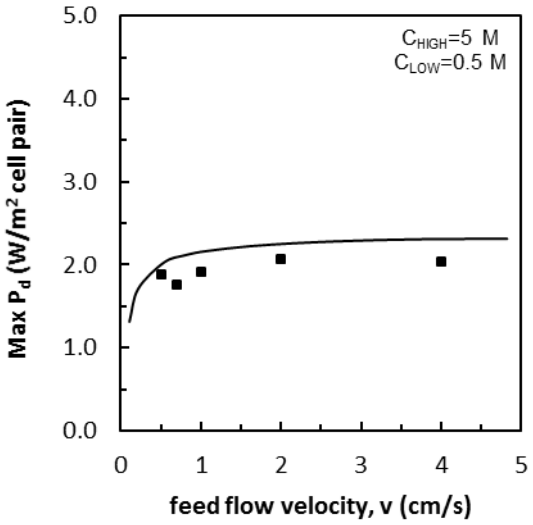

Figure 4.4. Effect of feed flow velocity on max power density. Experimental (points) and simulated (lines) data for a 50 cell pairs stack equipped with Fujifilm membranes, 270 μm woven spacers. C_{HIGH} = 5 M; C_{LOW} = 0.5 M; T = 20°C.

Looking at Figure 4.4, the model predicts well the experimental trend for the investigated cases. A higher velocity creates an increase in the maximum power density achievable, until a plateau is reached. The benefit of the increasing flow rate is attributed to two main reasons:

- Firstly, the higher the flow rate, the higher is maintained the concentration difference between solutions from inlet to outlet (i.e. the process driving force).
- Secondly, high flow rates reduce the effect of polarisation phenomena inside cells.

However, using seawater and brine as feed solutions, polarisation phenomena are relatively negligible [12]. Therefore, in such case the dominant effect of flow rates is the higher average driving force within channels.

4.3 Influence of feed temperature

Temperature can also significantly affect the transport properties of both membranes and solutions. In particular, the influence of increasing temperature on membrane resistance was experimentally observed by means of Electrochemical Impedance Spectroscopy (EIS) measurements [62]. The experimental information provided by EIS measurements was used to investigate the influence of temperature on system performance. Indeed, the developed model is able to predict the effect of temperature on cell potential and solutions properties. Results are shown in Figure 4.5, where the maximum power density reached by a 50 cell pairs stack is reported as a function of the feed temperature of both solutions.

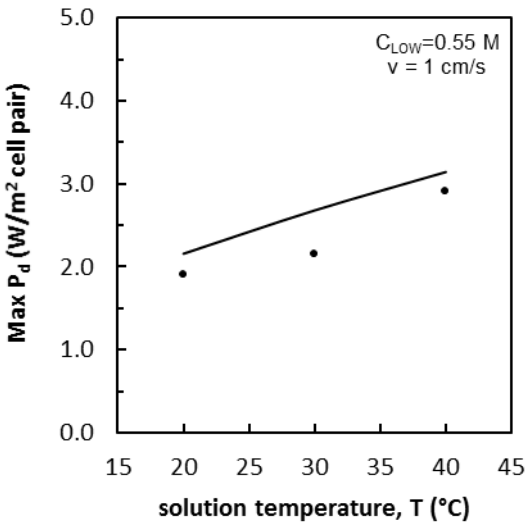

Figure 4.5. Effect of solution temperature on max power density. Experimental (points) and simulated (lines) data for a 50 cell pairs stack equipped with Fujifilm membranes, 270 μm woven spacers. C_{HIGH} = 5 M; C_{LOW} = 0.55 M; feed flow velocity: 1 cm/s.

Figure 4.5 clearly shows how the increase of temperature can notably enhance the process performance. In particular, increasing the temperature from 20 to 40°C the model predicts a 45% increase of the maximum power density. This influence is particularly interesting for those applications in which the salt solutions are already available at a temperature higher than 20°C, such as the case of using concentrated brines and seawater from salt ponds [28].

4.4 Optimal feed conditions for maximum power density

The choice of salt concentration of dilute/concentrated solutions is a crucial issue for optimisation of the RED process. In principle, the higher the salinity gradient between dilute-concentrate, the higher is the driving force for power production. On the other hand, this is not the only relation that controls the power output, as salt concentration affects also solution properties (e.g. activity coefficients, conductivity) and membrane features (permselectivity, resistance). The validated model has been used to predict the maximum power output obtained when different salt solutions are adopted, ranging from river water to seawater (0.01 – 0.55 M NaCl) as diluate, and from seawater to brine (0.5 – 5 M NaCl) as concentrate. A distribution map for power density (P_d) is shown in Figure 4.6, where contours show the values of P_d as a function of the inlet concentration for both diluate and concentrate.

Looking at Figure 4.6, the maximum power density predicted by the model for a 50 cell pairs stack is around 4 W/m^2 cell pair: this value can be achieved using a 70-90 mM NaCl solution as dilute (typical of brackish water) and 4.5-5 M NaCl solution as concentrate. It is worth noting that a further decrease of the dilute concentration can lead to a significant increase of the stack resistance. As a result, this would reduce the maximum power achievable, despite the higher concentration difference available within the RED stack.

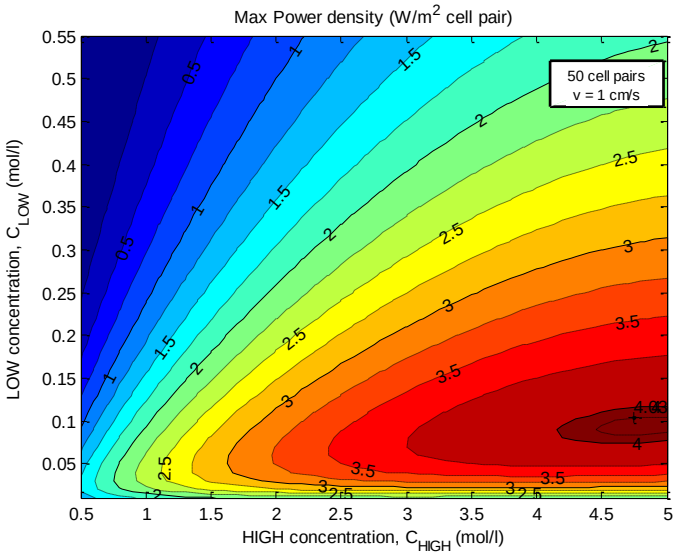

Figure 4.6. Effect of LOW/HIGH inlet concentration on maximum power density. Simulations of a 50 cell pairs stack (10×10 cm^2), equipped with Fujifilm membranes, 270 μm woven spacers; feed flow velocity inside channels: 1 cm/s. T = 20°C. Contours show max power density (W/m^2).

Furthermore, increasing the feed temperature from 20°C up to 40°C a 30% increase in the maximum power density can be achieved. This result is shown in Figure 4.7, where the maximum power density is plotted as a function of dilute feed concentration for 3 different values of feed temperature. In Figure 4.7 the brine concentration was set to 4.8 M NaCl, i.e. the value which maximises the P_d at 20°C (Figure 4.6). Interestingly, a power density of 5.3 W/m^2 is reached for the case of 40°C and 0.11 M NaCl feed concentration.

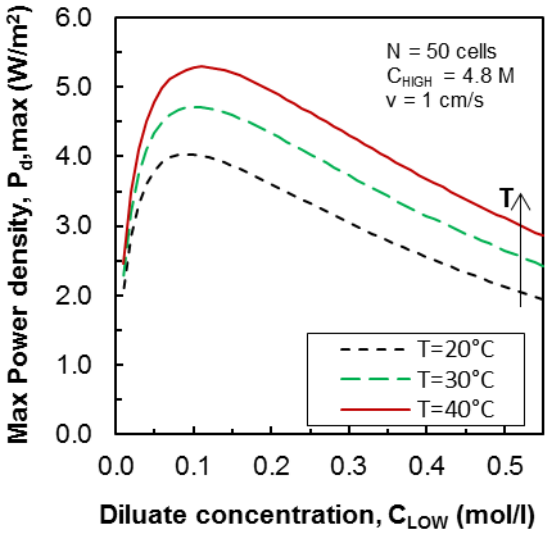

Figure 4.7. Simulations of a 50 cell pairs stack (10×10 cm^2), equipped with Fujifilm membranes, 270 μm woven spacers; feed flow velocity inside channels: 1 cm/s; C_{HIGH} = 4.8 M.

4.5 Effect of different path lengths for dilute/concentrate streams

4.5.1 Simulation of cross-flow arrangement

The model described so far (par. 3.3) was developed for a co-current flow distribution, where all the variables dependent on salt concentration (solution conductivity, cell pair voltage, etc.) vary only along compartment length. For this reason, a 1-D distributed model was considered, where the computational domain was discretised along the compartment length (Figure 4.8.A).

Such model was modified afterwards in order to account for a different flow arrangement, with cross-flow streams. In this case, the computational domain is defined in 2-Dimensions, where *x* and *y* are the flow directions for the concentrate and dilute solutions, respectively (Figure 4.8.B).

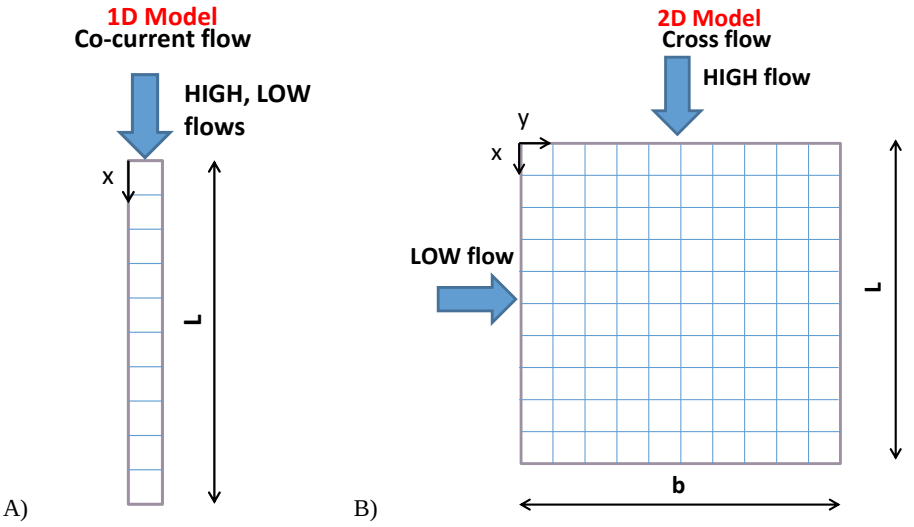

Figure 4.8. Computational domain of developed models: A) 1-D model (as described in par. 3.3). B) modified 2-D model.

The main advantage of such 2-D model approach is the high flexibility to simulate the use of asymmetric stack geometries, with one compartment longer and the other one wider, thus changing the aspect ratio of the system.

The new computational domain required a number of modifications within the model formulation previously introduced. In particular, all distributed variables described as *x*-dependent can vary along both *x* and *y* coordinates. Likewise, the mass balance in dilute and concentrate compartments (eq. (3.14)-(3.15)) need to be modified as follows:

$$\frac{\partial\left(Q_{HIGH}C_{HIGH}\left(x,y\right)\right)}{\partial x} = -J_{tot}\left(x,y\right)dy \tag{4.6}$$

$$\frac{\partial\left(Q_{LOW}C_{LOW}\left(x,y\right)\right)}{\partial y} = J_{tot}\left(x,y\right)dx \tag{4.7}$$

$$\frac{\partial\left(Q_{HIGH}\left(x,y\right)\right)}{\partial x} = -J_{w,\,net}\left(x,y\right)dy \tag{4.8}$$

$$\frac{\partial\left(Q_{LOW}\left(x,y\right)\right)}{\partial y} = J_{w,\,net}\left(x,y\right)dx \tag{4.9}$$

where Q is the volumetric flow rate in each compartment, C is the molar concentration, J_{tot} and $J_{w,net}$ are the salt and solvent fluxes through membranes, respectively.

It has been already highlight that the effect of diluate and concentrate on the overall stack resistance is sensibly different [21]. In order to simulate different path lengths for dilute and concentrate streams, the aspect ratio of the equipment has been defined as:

$$Aspect\ \ Ratio\left(AR\right) = \frac{HIGH\ \ path\ length\left(L\right)}{LOW\ \ path\ length\left(b\right)} \tag{4.10}$$

According to such definition, an aspect ratio < 1 gives a shorter compartment length for concentrate and a longer compartment length for diluate. The effect of aspect ratio on process performance is shown in Figure 4.9 and Figure 4.10 for a 100 cell pairs stack. Simulations were carried out assuming alternatively a fixed path length of 20 cm for one of the two streams, thus increasing the path length for the other up to 5 times (i.e. from 20 up to 100 cm). Flow rates of both solutions were adjusted accordingly, in order to keep the same fluid velocity (1 cm/s) within all compartments.

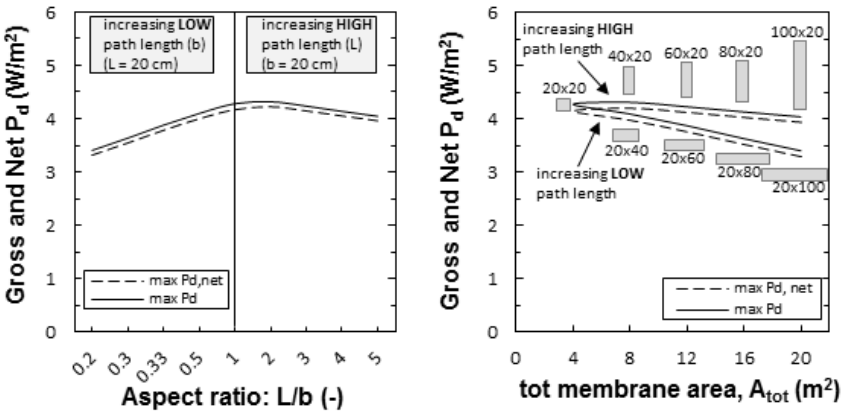

Figure 4.9. Influence of aspect ratio (L/b) on gross and net power density. Simulations of a 100 cell pairs stack equipped with Fujifilm membranes, 270 μm woven spacers; C_{LOW} = 0.1 M, C_{HIGH} = 5 M; v_{HIGH} = v_{LOW} = 1 cm/s; T = 20°C. Model predictions are shown as a function of aspect ratio (left plot) or total membrane area (right plot).

Figure 4.9 shows that the power density is negatively affected by a longer path length of the two streams, due to the increased residence time and consequent reduction in the average concentration gradient available. In particular, the increase in the diluate path length leads to a significant reduction in the power density generated. Conversely, a longer path length for concentrate has a weaker effect. In particular, increasing the paths length ratio from 1 (i.e. 20x20 cm^2 symmetric stack) up to 5 (20x100 cm^2 stack), a decrease in the power density of 20% and 7% are predicted by the model for the first and the second case, respectively.

A local maximum in the power density is predicted for AR = 2, where the P_d is slightly higher than for symmetrical stack. Such initial increase is likely related to a beneficial effect of the reduced mean concentration of the concentrate stream on membranes permselectivity. On the other hand, the global reduction is clearly related to the average reduction of driving force within the stack. On this basis, increasing the concentrate path length does benefit more the power output in terms of total net power produced (Figure 4.10), indicating how the use of asymmetric stack, using a shorter path for dilute, allows to enhance the power output and yield (defined with respect to the HIGH feed solution) of the RED process.

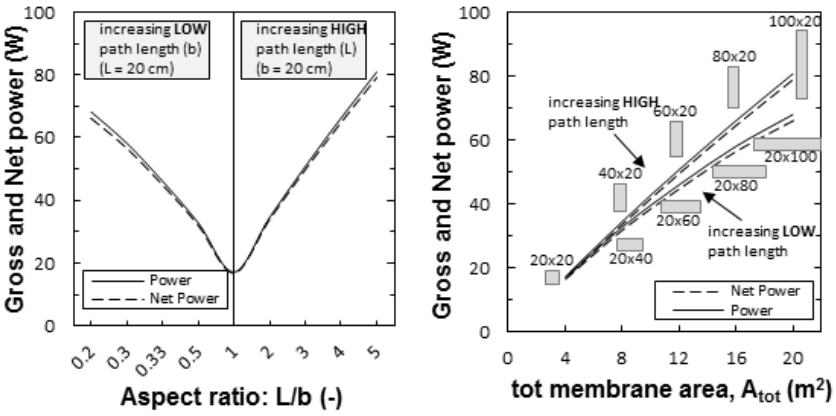

Figure 4.10. Influence of aspect ratio (L/b) on gross and net power. Simulations of a 100 cell pairs stack equipped with Fujifilm membranes, 270 μm woven spacers; C_{LOW} = 0.1 M, C_{HIGH} = 5 M; v_{HIGH} = v_{LOW} = 1 cm/s; T = 20°C. Model predictions are shown as a function of aspect ratio (left plot) or total membrane area (right plot).

4.6 Simulation of large unit (20x20 cm^2, 100 cell pairs)

4.6.1 Effect of salt concentration

The effect of inlet concentration for both dilute and concentrate has been investigated on a 20x20 cm^2 stack equipped with 100 cell pairs (Figure 4.11). It is worth noting that feed concentrations affect also the viscosity of solutions and, therefore, the pressure drops inside the stack. As a consequence, the effect of inlet concentration on net power density is slightly different (Figure 4.11b).

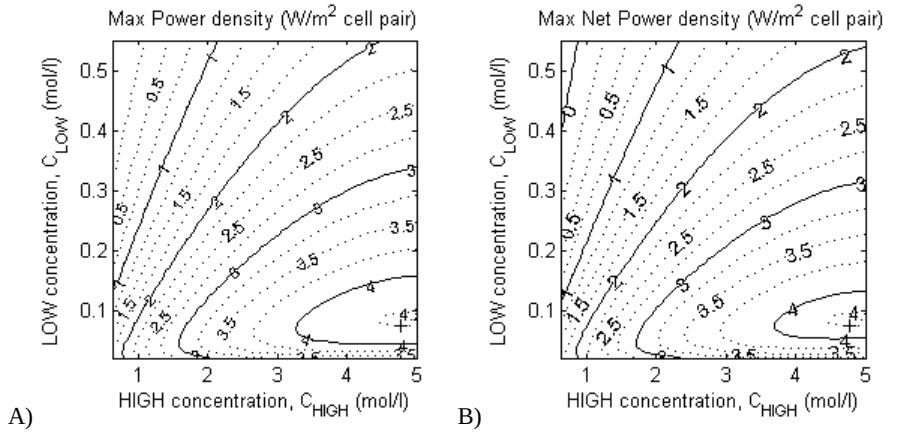

Figure 4.11. Effect of the inlet concentration on gross and net power density for a 100 cell pairs stack (20×20 cm^2), equipped with Fujifilm membranes, 270 μm woven spacers. Feed flow velocity: 1 cm/s; T = 20°C.

Interestingly, the maximum power density is achieved by the 20x20 cm^2 stack at inlet concentration of approximately 0.08 M NaCl and 4.7 M NaCl, which can be identified as optimal solutions for the investigated case. Such conditions lie in a similar concentration range as the one previously identified for the smaller 10x10 cm^2 RED unit (Figure 4.6). On the other hand, the net power density map (Figure 4.11b) shows a zone where negative values are predicted, thus indicating that the pumping power is greater than the gross power output.

4.6.2 Influence of feed flow rates

Starting from the optimal feed concentration shown in Figure 4.11, different conditions were explored to find the best flow rates for both solutions. Figure 4.12 shows gross and net power density for a 20x20 cm^2 stack with 100 cell pairs assuming a fluid velocity ranging from 0.1 up to 3 cm/s for both solutions.

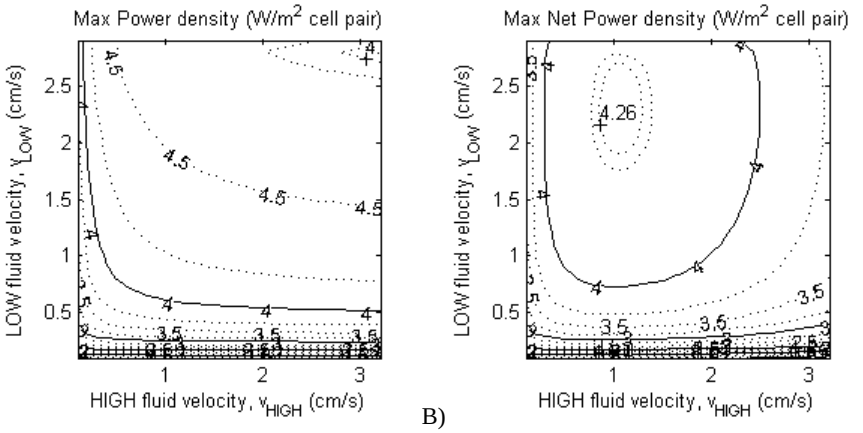

Figure 4.12. Effect of channel velocities on gross (A) and net (B) power density for a 100 cell pairs stack (20×20 cm^2), equipped with Fujifilm membranes, 270 μm woven spacers; C_{LOW} = 0.08 M, C_{HIGH} = 4.7 M; T = 20°C.

Clearly, the higher the fluid velocity, the higher is the gross power density (Figure 4.12a), due to the low residence time for both solutions inside the stack and relatively larger driving forces kept between the membranes. However, the maximum for the diluate velocity is not achieved at the boundary of the investigated range (Figure 4.12.A). In fact, the power density increases until an optimal velocity of about 2.7 cm/s is reached, then decreasing again for larger values of velocity. This is related to the increasing electrical resistance of the dilute solution, which is caused by the extremely small residence time.

On the other hand, when looking at the net power density (Figure 4.12.B), a maximum of 4.6 W/m^2 is predicted for a fluid velocity of 1 cm/s for concentrate and between 2 – 2.5 cm/s for diluate. Such operating conditions ensure high driving forces, and with acceptable pressure drops.

All the results shown above indicate that the performance of the process is sensibly affected by the properties of dilute stream. In order to explore in more detail the optimal operating conditions for a 100 cell pairs stack (20x20 cm^2), a further analysis was carried out changing both velocity and inlet concentration for the diluate. Results are shown in Figure 4.13, where gross and net power density are plotted as a function of the operating conditions for diluate, ranging from 0.1 to 3 cm/s for fluid

velocity, and from 0.01 to 0.55 M for inlet concentration. All the simulations were performed changing the concentrate fluid velocity accordingly with the dilute velocity.

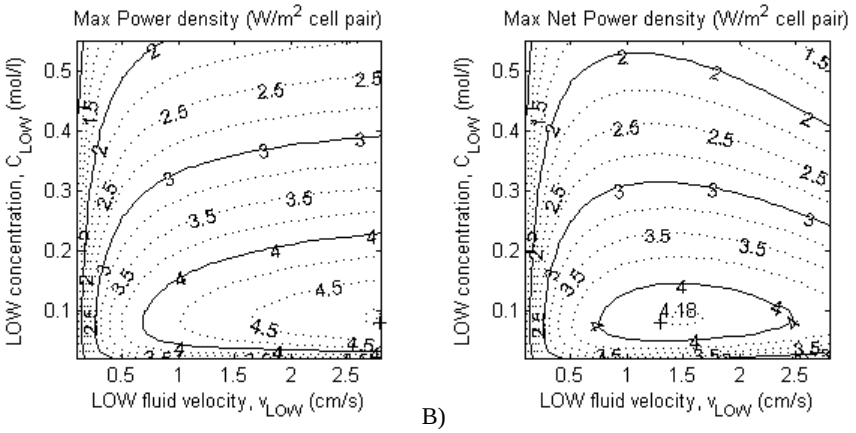

Figure 4.13. Gross (A) and net (B) power density as a function of operative conditions (inlet concentration in dilute compartment and fluid velocity). Simulations of a 100 cell pairs stack (20×20 cm^2), equipped with Fujifilm membranes, 270 μm woven spacers; C_{HIGH} = 4.7 M; v_{HIGH} = v_{LOW}; T = 20°C.

Given the assumption of equal fluid velocities for both streams, a maximum net power density of 4.18 W/m^2 is predicted by the model, in conditions slightly different from the previous cases, i.e. with a fluid velocity of 1.5 cm/s and a LOW inlet concentration close to 0.1 M NaCl (Figure 4.13.B).

4.7 Simulation of a pilot-scale unit

In order to simulate a larger RED unit (with reference, in particular, to the REAPower demonstration plant operating with saltworks brines in Marsala, Italy [29]), a number of different scenarios were taken into account starting from a 100 cell pairs stack (22x22 cm^2) as reference case (Table 4.3). All scenarios were designed to investigate the effect of scale-up on either symmetric or asymmetric stack design. A concentrated brine of 5 M NaCl and brackish water (0.1 M NaCl) were considered as feed solutions for all cases. When simulating asymmetric stacks, the concentrated

brine was always fed to the longer channel, given the better performance registered in the previously reported analysis for such flow configuration (par. 4.5).

Table 4.3. Summary of simulations carried out on large prototype unit.

Scenario #	Membrane size (cm)	N° cell pairs	Total membrane Area (m^2)	Description
1	22 x 22	100	4.8	Reference case (small prototype)
2	22 x 22	500	24.2	Larger number of cell pairs
3	44 x 44	500	96.8	Larger symmetric stack
4	22 x 88	500	96.8	Larger asymmetric stack, AR = 4
5	44 x 88	500	193.6	Larger asymmetric stack, AR = 2
6	22 x 88	500	96.8	asymmetric stack, different velocity (v_{LOW} = 1 cm/s, v_{HIGH} = 2 cm/s)

Figure 4.14 shows the gross and net power density for the investigated scenarios. As expected, the decrease in power density due to the longer HIGH path length is rather negligible. Moreover, increasing the number of cell pairs up to 500 (scenario 2), causes a slight reduction in power density, likely due to the following two counteracting effects: i) reduction of the influence of blank resistance on the overall performance; ii) increase of parasitic currents within the stack, thus reducing the power output.

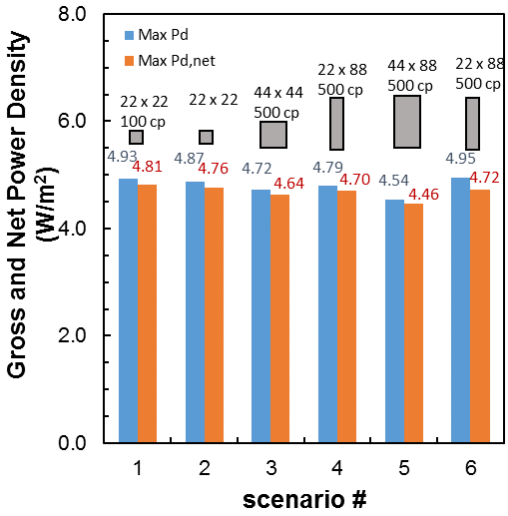

Figure 4.14. Gross and net power density for stacks equipped with Fujifilm membranes, 270 µm woven spacers; C_{LOW} = 0.1 M; C_{HIGH} = 5 M; v_{LOW} = v_{HIGH} = 1 cm/s, in scenario no. 6 v_{LOW} = 2 cm/s, v_{HIGH} = 1 cm/s; T = 30°C.

Figure 4.15 shows the predicted gross and net power output for the above-mentioned scenarios.

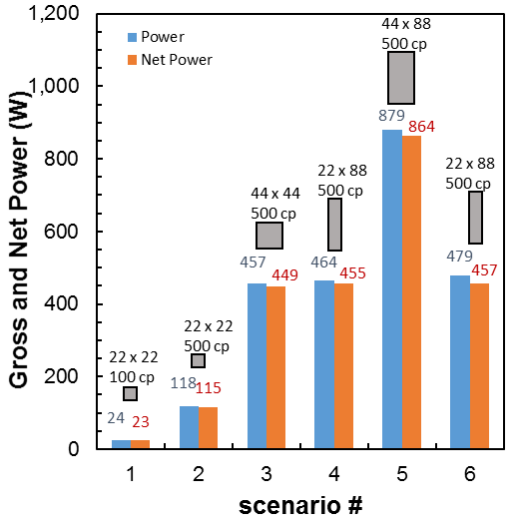

Figure 4.15. Gross and net power density for stacks equipped with Fujifilm membranes, 270 µm woven spacers; C_{LOW} = 0.1 M; C_{HIGH} = 5 M; v_{LOW} = v_{HIGH} = 1 cm/s, in scenario no. 6 v_{LOW} = 2 cm/s, v_{HIGH} = 1 cm/s; T = 30°C.

In the case of 44x88 cm^2 stack equipped with 500 cell pairs (scenario 5) a power output of almost 900 W has been predicted, which emphasize how the target of 1 kW can be reached with a single stack, provided that an active membrane area of 44x88 cm^2 is guaranteed.

4.8 Process simulation of a plant with 3 RED units

The developed process simulator was finally used to describe the operation of a RED plant with a train of 3 units, each one with a 44x44 cm^2 active membrane area and 500 cell pairs. The main goal of this modelling task was to simulate the possible plant layouts to be adopted for the REAPower demonstration plant, using concentrated brine and brackish water as feed solutions.

Aside from the stack design, the streams arrangement among the units can significantly affects the overall power output, as well as the performance of each single stack. In all simulations, a concentrate feed flow rate of 29.4 l/min was assumed, in order to guarantee a standard flow velocity of 1 cm/s. Conversely, three different scenarios were investigated for diluate feed flow rate, to analyse the effect of different flow rates availability in the real installation site. In particular, the flow rates of 20 l/min, 29.4 l/min (as in the HIGH channels) and 40 l/min were set in the three simulated cases. A diluate feed concentration of 0.03 M was adopted, according to the real availability of brackish water in the prototype installation site.

As previously shown, the residence time of concentrated brine has been found not to be dramatic for process performance. For this reason, a serial arrangement among units was adopted for the concentrate. Conversely, a number of possible distribution paths have been analysed for the diluate. In Figure 4.16 the three most promising configurations are shown, namely:

- *Layout A (serial arrangement,* Figure 4.16.A*).* In this case, the 3 stacks are fed in series for both diluate and concentrate, with a recycle for the diluate in the first stage. This allows the control of fluid velocity of 1 cm/s inside the first stack, even if the availability of brackish water is low. This arrangement also guarantees in the first stack a uniform concentration in the diluate

compartment, in a range closer to the previously identified optimal concentration.

- *Layout B (parallel arrangement*, Figure 4.16.B*)*. All stacks are fed in series for the concentrate stream and in parallel for the diluate, thus requiring a partial recycle of the exiting dilute stream in order to operate all the three stacks with a standard velocity of 1 cm/s. This configuration ensures a more homogeneous driving force for all units.
- *Layout C (parallel-serial arrangement*, Figure 4.16.C*)*. This hybrid configuration provides a parallel feed for diluate into the first two stacks, using the overall outlet to feed the third unit, where the fluid velocity is much larger than in standard conditions.

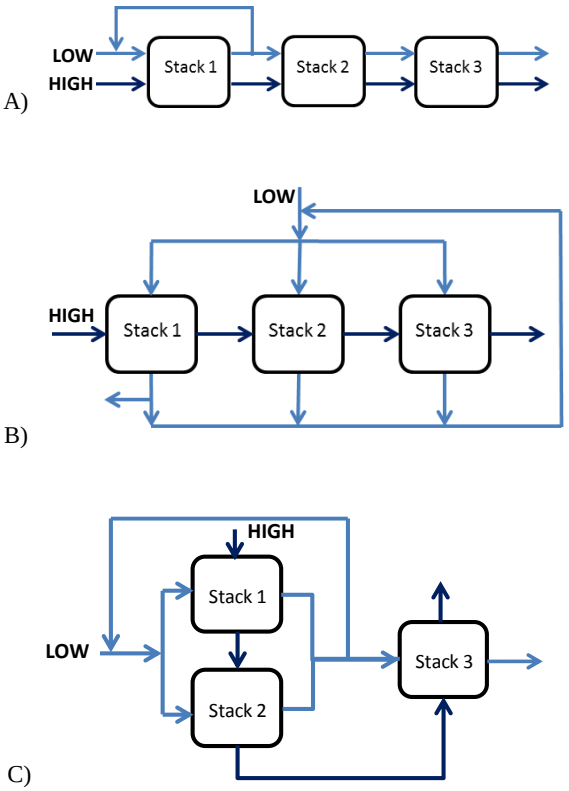

Figure 4.16. Investigated layouts for streams arrangements. A) Serial arrangement. B) Parallel arrangement. C) Parallel-serial arrangement.

The flowsheet implemented in gPROMS Model Builder environment was modified accordingly. The first layout is shown in Figure 4.17 as an example.

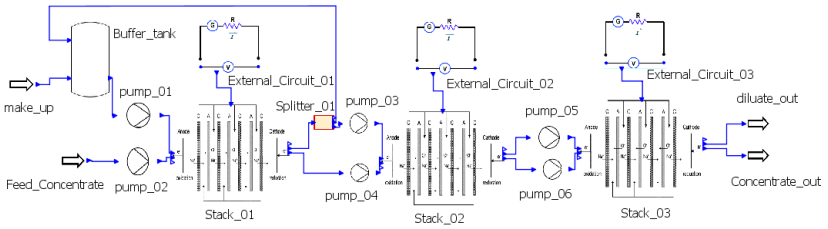

Figure 4.17. Implemented flowsheet for 3 RED units with serial arrangement (Layout A). Similar flowsheets (not shown in the figure) were built within the process simulator for Layouts B and C.

The first set of model predictions, relevant to the case of diluate feed flow rate of 20 l/min, are reported in Figure 4.18.

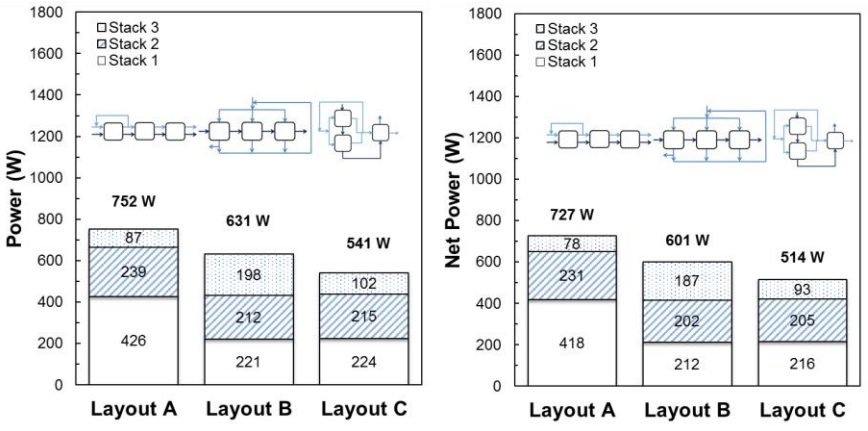

Figure 4.18. Gross and Net Power of 3 stacks (44×44 cm^2, 500 cell pairs) equipped with Fujifilm membranes and 270 µm woven spacers. Layout A: serial. Layout B: parallel. Layout C: parallel-serial for diluate feed; C_{HIGH} = 5 M; Q_{HIGH} = 29.4 l/min; brackish water inlet conditions: Q_{LOW} = 20 l/min, C_{LOW} = 0.03M.

For layout A (serial arrangement), a make-up of 20 l/min of brackish water is not sufficient to guarantee a flow velocity of 1 cm/s in all compartments. For this reason, a recycle of the outlet dilute is required at least after the first stack. It is worth noting

that layout B (parallel arrangement) is clearly the optimal configuration to ensure equal performance for all stacks. Nonetheless, layout A gives a higher power output (752 W), while the layouts B and C can provide (with 3 stacks) the same power output generated by the first two stacks in layout A.

In order to feed the plant with no recycle and keep a fluid velocity of 1 cm/s in all channels, the required brackish water flow rate is 29.4 l/min. Figure 4.19 shows model predictions for the investigated plant layouts, assuming the availability of 29.4 l/min of brackish water as make-up to the plant.

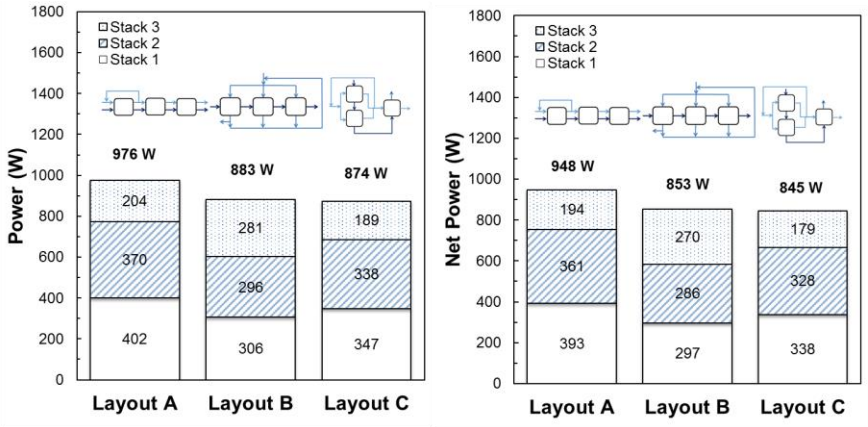

Figure 4.19. Gross and Net Power of 3 stacks (44×44 cm^2, 500 cell pairs) equipped with Fujifilm membranes and 270 μm woven spacers. Layout A: serial. Layout B: parallel. Layout C: parallel-serial for diluate feed. C_{HIGH} = 5 M; Q_{HIGH} = 29.4 l/min; brackish water inlet conditions: Q_{LOW} = 29.4 l/min, C_{LOW} = 0.03 M.

An increase of the dilute make-up allowed to reach a power output of 976 W for layout A (Figure 4.19). Moreover, a higher make-up of brackish water gives minor differences among the layouts in terms of power output, thus improving significantly the performances of layouts B and C.

The availability of brackish water is therefore a key factor for the performance of the RED plant. Assuming to double the original amount of brackish water available, the process simulator was used to predict the plant operation with a make-up of brackish water of 40 l/min (Figure 4.20).

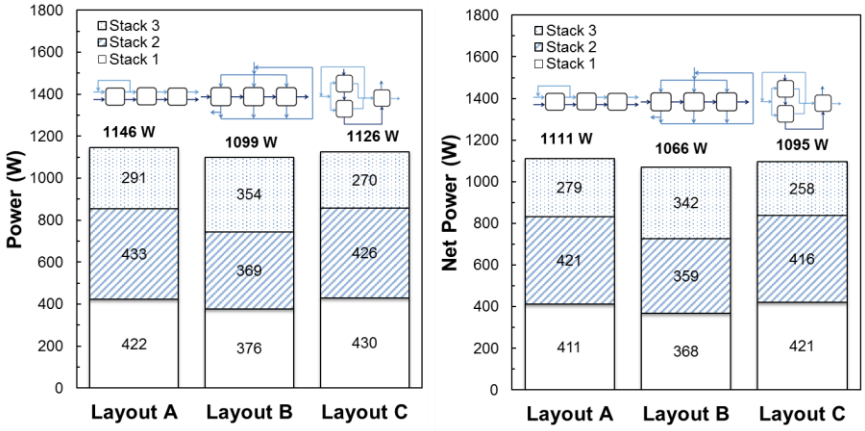

Figure 4.20. Gross and Net Power of 3 stacks (44×44 cm^2, 500 cell pairs) equipped with Fujifilm membranes and 270 µm woven spacers. Layout A: serial. Layout B: parallel. Layout C: parallel-serial for diluate feed. C_{HIGH} = 5 M; Q_{HIGH} = 29.4 l/min; brackish water inlet conditions: Q_{LOW} = 40 l/min, C_{LOW} = 0.03 M.

A brackish water availability of 40 l/min would allow reaching more than 1 kW with all of the investigated plant layouts. Interestingly, for layout A the power produced from the second stage (433 W) is slightly higher than the power from the first stage (422 W). This is because in the second stage the diluate inlet concentration is closer to its optimal value, as previously shown by the parametric analysis (Figure 4.12).

4.9 Outlook and final remarks

In this chapter, the model previously described was validated against original experimental data and used to simulate a variety of experimental conditions.

Using two tuning parameters to take into account the influence of feed concentration on the most relevant membranes properties (permselectivity and resistance), the model was able to predict the experimental behaviour for a wide range of operating conditions (inlet concentrations, flow rates, feed temperature).

After the tuning/validation task, the proposed model was used to predict the effect of different inlet concentrations on process performance. For the investigated system, the optimal feed solutions that maximise the power output are brackish water (0.8-0.9

M NaCl) as diluate and brine (4.5-5 M NaCl) as concentrate, which would lead to a maximum power density of 4 W/m^2 of cell pair for a 50 cells stack.

Regarding the stack design, the possibility of using asymmetric stack has been addressed, being the model able to simulate different flow path lengths for dilute and concentrate streams, adopting a 20x20 cm^2 stack with 100 cell pairs as reference case. Increasing the aspect ratio from 1 (i.e. 20x20 cm^2 symmetric stack) up to 5 (20x100 cm^2 stack), a decrease from 7% to 20% in the power density is registered, with larger effects observed when increasing the diluate path length. On the other hand, increasing the concentrate path length enhances almost proportionally the power output and the overall process yield (defined with respect to the concentrate stream) achieved.

In order to identify optimal operating conditions for a 20x20 cm^2 stack in terms of feed concentration and velocities, an optimisation analysis has been performed, highlighting the dominant influence of diluate compartment conditions on the overall unit performance.

Finally, the behaviour of larger prototypes was simulated, providing useful indications for the design and operation of the REAPower pilot plant. A number of possible layouts have been presented, considering three RED units equipped with 500 cells pairs of 44x44 cm^2 active membrane area. Three different conditions were considered in terms of availability of diluate feed. Interestingly, in the case of low availability of brackish water (20 l/min), a serial arrangement is preferable, as two stacks in series providing practically the same power output of 3 stacks differently connected.

5 LABORATORY INVESTIGATION OF RED PROCESS*

Abstract

This chapter describes the experimental investigation carried out with a reverse electrodialysis laboratory unit equipped with 10x10 cm^2 membrane area and 50 cell pairs. The experimental campaign was performed at VITO (Flemish Institute for Technological Research – Mol, Belgium) using a fully equipped test-rig. Two different sets of membranes were tested, analysing various operating conditions in terms of feed concentration, temperature and flow rate. Aside from providing data for modelling validation, these tests allowed to identify experimentally the best performance achievable by the adopted RED system, optimising the operation within the planned experimental range. Combining the most favourable conditions, a power density of 12 W/m^2 of cell pair was reached using 0.1 M NaCl as diluate and 5 M NaCl as concentrate at 40°C. These results, which are among the highest values so far reported in the literature, demonstrate that a careful analysis of the operating conditions and membrane properties can significantly improve the overall performance of the RED technology.

* Part of this chapter has been submitted in revised form as:

- M. Tedesco, E. Brauns, A. Cipollina, G. Micale, P. Modica, G. Russo, J. Helsen, *Laboratory scale-up of Reverse Electrodialysis for power production from seawater and brine*, submitted to Journal of Membrane Science (2015).

5.1 Introduction

The first experimental demonstration of RED process dated back to 1955, when a power output of 15 mW (i.e. 0.05 W/m^2 of membrane) was reported by Pattle [14]. Conventional ED stacks, i.e. built with membranes and spacers commonly used for electrodialysis, were initially exploited for this purpose. In this way, a power density of 0.4 W/m^2 of membrane was achieved by Audinos [15]. In fact, the power obtainable from those early systems were limited by the lack of suitable ion exchange membranes [14–17]. The following availability of new membranes and a deeper investigation on process conditions allowed to increase significantly the power produced by RED systems (Table 5.1). Using artificial river water (0.017 M NaCl) and seawater (0.5 M NaCl) as feed solutions, Veerman et al. obtained a power density of 0.93 W/m^2 of membrane on a 50 cell pairs stack [20]. This work demonstrated that the use of low resistance membranes and a proper stack design (i.e. small compartments thickness, good sealing) are crucial aspects for enhancing the process performance.

The selection of redox couple for the electrode compartments plays also a role for ensuring stable performance and improving the system, especially on a laboratory-scale. The redox species commonly adopted for RED applications are iron redox couples, such as $FeCl_3$ / $FeCl_2$, $K_3Fe(CN)_6$ / $K_4Fe(CN)_6$ and Fe(III)-EDTA / Fe(II)-EDTA. In particular, $K_3Fe(CN)_6$ / $K_4Fe(CN)_6$ is widely used in RED, thanks to its good stability in process conditions, when contact with oxygen and light is avoided [35]. The kinetics of electrochemical processes in such systems is generally controlled by mass transfer in the electrolyte, thus a concentration of the redox couple higher than 0.05 M is preferable to avoid high power losses [79].

Table 5.1. Power density (expressed as W/m^2 of membrane) experimentally obtained in RED system.

year	Authors	Power density (W/m^2)	spacer thickness and experimental conditions	Source
1955	Pattle	0.05	1 mm spacers, 39°C	[14]
1976	Weinstein and Leitz	0.17	1 mm spacers, 0.02 M – 0.57 M	[16]
1983	Audinos	0.40	1 mm spacers, 4.3 M	[15]
1986	Jagur-Grodzinski and Kramer	0.41	250 µm spacers, tap water and seawater	[17]
2007	Turek and Bandura	0.46	190 µm spacers, 0.01 M – 0.55 M	[18]
2008	Turek et al.	0.87	190 µm spacers, 0.01 M – 1.9 M	[19]
2008	Veerman et al.	0.93	200 µm spacers, 0.017 M – 0.5 M	[20]
2011	Vermaas et al.	2.20	60 µm spacers, 0.017 M – 0.5 M	[26]
2014	Daniilidis et al.	5.30	100 µm spacers, 0.01 M – 5 M, 40°C	[21]
2014	Daniilidis et al.	6.70	100 µm spacers, 0.01 M – 5 M, 60°C	[21]

A notable reduction of the stack resistance has been obtained by using conductive spacers instead of common (uncharged) spacers. Długołecki et al. showed that the use of ion-conductive materials allow to halve the resistance when river water and seawater are used as feed, thus increasing the power density by a factor of 3 [43]. Starting from these results, further efforts have been focused on the construction of profiled membranes, were the spacers are substituted by properly structured IEMs. In this way, a reduction of the overall resistance was detected, yet increasing the influence of concentration polarisation phenomena on the process. As a result, only a slight increase in the power density was observed, essentially at high flow velocity [44]. This might be attributed to the structure geometry, which is in fact not optimised for the process. With this regard, using pillar-structured membranes, Güler et al. reached a 38% increase of power density (up to 1.3 W/m^2 of membrane) with respect to the flat membranes at high Reynolds numbers [80]. Therefore, the use of profile

IEMs might be very promising in the future, especially thanks to the lower pressure drops achieved.

Although it is worth reducing the resistance of spacers and membranes, the largest contribution to the overall resistance is given by the diluate compartment, which represents about 45% of the whole resistance when using river water – seawater [20]. Clearly, the use of thinner compartments significantly improves the process performance in such conditions. In this way, a power density of 2.2 W/m^2 of membrane (i.e. 4.4 W/m^2 cell pair) was reached using 60 µm spacers [26]. Despite the significant improvement in the power output, the use of very thin channels is not reliable in practical applications, due to the high pressure drops and the increasing risk of fouling [52].

These drawbacks may be overcome using seawater (or brackish water) as diluate, and saturated brine as concentrate [27–29]. The use of brine is also beneficial to increase the salinity gradient for power production. The first experimental demonstration of this potential was given by Turek et al., who reached 0.87 W/m^2 of membrane using fresh water (0.01 M NaCl) and coal-mine brine (1.9 M NaCl) [19]. More recently, Daniilidis et al. achieved a power density of 5.3 W/m^2 within a small laboratory stack equipped with 5 cell pairs and extremely thin spacers (100 µm), using fresh water (0.01 M NaCl) and brine (5 M NaCl) at 40°C. Moreover, increasing the temperature up to 60°C, a maximum power density of 6.7 W/m^2 of membrane was obtained [21], though such temperature levels are impractical in a real operating plant.

All of these results clearly demonstrate that there is still large room for improvement in RED technology, and an accurate investigation of the process conditions is still required for enhancing the performance in the technology scale-up.

In this work, an extensive experimental campaign has been carried out adopting a reverse electrodialysis laboratory unit fed with highly saline solutions. The unit consisted in a 50 cell pairs stack, with an innovative cross-flow configuration [40], equipped with two different sets of membranes (thickness of 120 µm and 20 µm, respectively) and spacer thickness of 270 µm. A number of different dependencies on the main operating conditions were analysed, such as feed solutions' velocity,

concentration, temperature and composition of the electrode rinse solution. The operating ranges were selected in order to fit the physical expectances for a pilot plant to be operated with real brines. In particular, the experimental investigation presented in this chapter can be considered as a pre-piloting campaign, as it provided useful indications for the construction and testing of the RED pilot plant discussed in the following chapters (6-7).

5.2 Experimental apparatus and procedures

The experimental campaign was performed at the Flemish Institute for Technological Research (VITO – Mol, Belgium) using a fully equipped test-rig (Figure 5.2). This section describes the experimental setup used, the developed control software and the experimental procedure adopted during the tests.

For the sake of clarity, the definitions of the most relevant process variables are here reported, though a detailed modelling description of the RED process has been already presented in Chapter 3.

5.2.1 Experimental apparatus

A fully automatized test-rig was built to monitor all the operating variables of solutions (flow rate, temperature, pressure, conductivity) and the electric variables of the RED system. The dilute feed solution (LOW) and the concentrate (HIGH) are pumped to the RED unit from two tanks with a capacity of 200 l each (Figure 5.2). Each tank is equipped with a stirrer and a temperature regulation system consisting in a heating and a cooling immersed coil.

Both LOW and HIGH circuits are equipped with two different pumps: (i) a centrifugal pump (Iwaki Magnet Pump 400CV5-D), with an automatic flow rate control; (ii) a peristaltic pump (Watson Marlow 604U) for tests at low flow rates. Peristaltic pumps were adopted to control the LOW and HIGH feed concentrations (or restore them to the set values when operating with a recycle of feed solutions). This was, in fact, performed by adding demineralized water into the dilute tank, or saturated NaCl brine to the HIGH tank.

The electrode rinse solution (ERS) is pumped to the stack from a 30 l tank using a peristaltic pump (Watson Marlow 604U). The ERS tank is also equipped with a stirrer (IKA RW 28) and a level control system. During the operation, the transparent parts in the ERS circuit were covered with aluminum foil to avoid decomposition of the redox couple due to UV exposure [35,47].

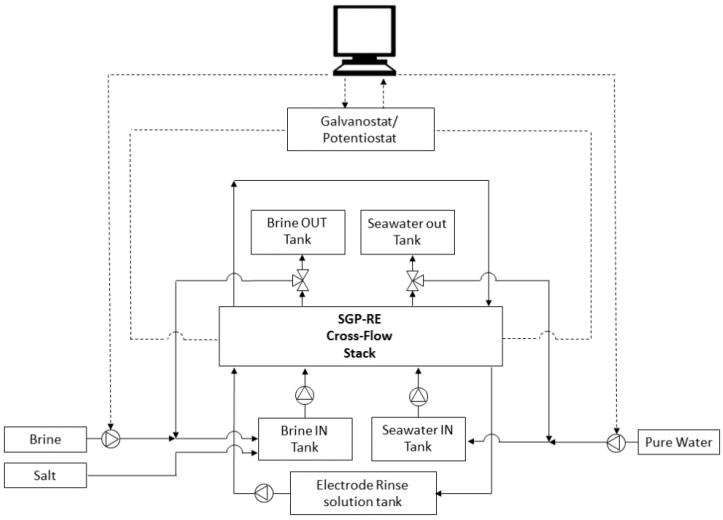

Figure 5.1. Scheme of RED experimental apparatus.

Conductivity meters (Mettler Toledo InPro 7100) and pressure transducers (Endress+Hauser Cerabar M) were installed both at inlet-outlet for each solutions. A picture showing the three loops for HIGH, LOW and ERS is reported in Figure 5.2.

Figure 5.2. Experimental setup at VITO. The three hydraulic loops for dilute (LOW), concentrate (HIGH), and electrode rinse solution (ERS) are shown.

A dedicated control software, called MeFiAS, was developed at VITO using LabVIEW™ environment (National Instruments, USA). All the solutions properties (flow rate, temperature, pressure, conductivity) for the three solutions and electric variables can be monitored from the main panel of the software.

Reverse electrodialysis stack

A RED unit with 10x10 cm^2 membrane area (REDstack BV, The Netherlands) was used for all the tests. The stack was equipped with 50 cell pairs, using 270 µm polyamide woven spacers (Deukum GmbH, Germany). Two Ru-Ir oxide coated Ti electrodes were used in the end-compartments (Magneto Special Anodes BV, The Netherlands). A cross-flow arrangement was adopted for feeding solutions (Figure 5.3).

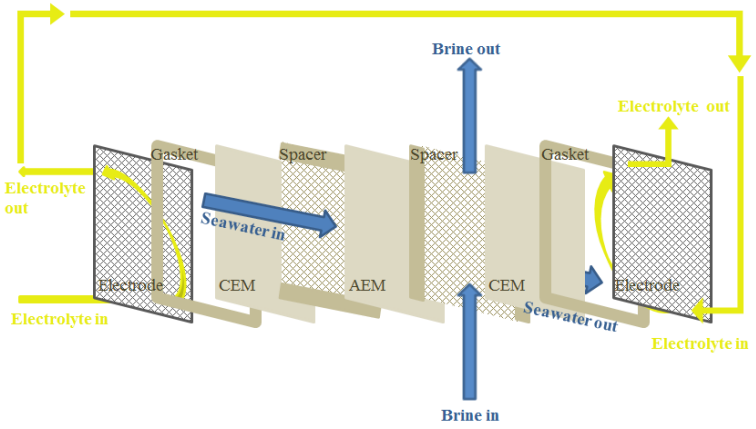

Figure 5.3. Description of cross-flow arrangement.

Two different sets of ion-exchange membranes were used: a first set with 120 µm thickness (Fujifilm Manufacturing Europe BV, The Netherlands), and a second set of 20 µm-thick membranes (FuMatech GmbH, Germany). The most relevant properties of both sets of membranes are reported in Table 5.2.

Table 5.2. Properties of the membranes sets adopted in the experiments.

SET	Membranes	Thickness (µm)	Electrical areal resistance [a] (Ω cm^2)	Permselectivity[b] (%)
1	Fujifilm AEM 80045-01	120	1.83	96 %
	Fujifilm CEM 80050-04	120	2.55	96 %
2	Fumasep FAS-20	20	0.5	95.5 %
	Fumasep FKS-20	20	1.7	99.02 %

[a] electrical resistance measured in 0.5 M NaCl solution at 25°C.
[b] permselectivity measured in river water (0.017 M NaCl) – seawater (0.5 M NaCl) conditions.

It is worth noting that the use of thinner membranes required additional efforts for avoiding their mechanical breakage and internal leakages of the stack. In particular, it was necessary to glue each membrane to the spacer's gasket using a common adhesive, which made impossible the stack disassembly. This procedure was not required for the thicker membranes.

Artificial salt solutions were prepared using demineralised water and technical grade NaCl (ESCO, The Netherlands). The aqueous electrode rinse solution contained 0.1 M $K_3Fe(CN)_6$, 0.1 M $K_4Fe(CN)_6$ and 2.5 M NaCl as supporting electrolyte.

A standard reference test was defined for all measurements (Table 5.3), while dependencies were investigated changing one operating variable per time.

Table 5.3. Standard conditions adopted for the reference test.

Parameter	**Standard test value**
Number of cell pairs	50
dilute concentration	0.5 M NaCl
concentrate concentration	5 M NaCl
fluid velocity	1 cm/s
temperature	20°C
Electrode rinse solution properties:	
composition	0.1 M $K_3Fe(CN)_6$, 0.1M $K_4Fe(CN)_6$, 2.5 M NaCl
conductivity	200 mS/cm
flow rate	30 l/h
temperature	20°C

5.2.2 Experimental procedures

Power density measurements

Power measurements tests were carried out in galvanostatic mode using a potentiostat/galvanostat (AMEL 2044), fully controlled by the MeFiAS software. A current ramp in the range of 0 – 1 A was used, with 50 mA current step. The MeFiAS software acquires the current (I) and stack voltage (E_{stack}) data during the experiment via respectively a Seneca T201DC100 and T201DC101 module. Therefore, the stack resistance can be calculated from Ohm's law:

$$E_{stack} = OCV - R_{stack}\ I \tag{5.1}$$

where *OCV* is the Open Circuit Voltage, and R_{stack} is the electrical resistance of the stack. The output power (*P*) is given by:

$$P = E_{stack}\ I \tag{5.2}$$

The power density is defined as the power produced per cell pair area:

$$P_d = \frac{P}{N\ A} \tag{5.3}$$

where *N* is the number of cell pairs and *A* is the area of one cell pair (in this case, 10x10 cm^2).

The net power density has been evaluated as the measured power output minus the theoretical pumping power required, calculated in terms of hydraulic loss (assuming 100% pump efficiency), and divided by the total cell pair area of the stack:

$$P_{d,net} = \frac{P - \Delta p_{HIGH} Q^{tot}_{HIGH} - \Delta p_{LOW} Q^{tot}_{LOW}}{N\ A} \tag{5.4}$$

where Δp is the pressure drop inside the stack, Q^{tot} is the total flow rate, while subscripts *HIGH* and *LOW* refer to concentrate and dilute stream, respectively.

Evaluation of blank resistance and corrected power density

The amount of energy that can be harvested from an RED system is also affected by the resistance of the electrode compartments, often known as blank resistance (R_{blank}). This contribution can be significant for lab-scale units, where a relatively small number of cell pairs is used. On the other hand, when scaling-up the process to a stack with a large number of cell pairs (e.g. higher than 100-200), the power loss at the electrodes will be negligible [31]. Thus, in order to correct the measured power output accounting for such effect, a correction procedure can be implemented based

on the measured value of OCV, and the resistance of stack and electrode compartments. In particular, R_{blank} can be experimentally estimated by evaluating the stack resistance when varying the number of cell pairs, thus identifying R_{blank} as the intercept of the regression line with the y-axis [46]. For this purpose, measurements were performed with 10, 30 and 50 cell pairs (Figure 5.4).

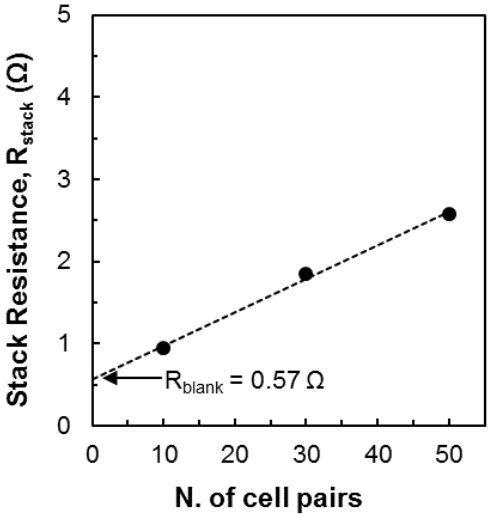

Figure 5.4. Evaluation of stack resistance at different cell pairs number. A blank resistance R_{blank} = 0.57 Ω is estimated as the intercept with *y*-axis. Stack equipped with Fujifilm (120 µm) membranes, 270 µm woven spacers. C_{LOW} = 0.5 M NaCl, C_{HIGH} = 5 M NaCl, v = 1 cm/s, T = 20°C.

Following such procedure, a blank resistance of 0.57 Ω was estimated for the investigated conditions (Figure 5.4). On this basis, the stack voltage can be corrected subtracting from the OCV the voltage drops due to the cell pairs internal resistance:

$$E_{stack,corr} = OCV - R_{cells}\, I_{corr} \tag{5.5}$$

where R_{cells} is the electrical resistance of the membrane pile (i.e. $N \cdot R_{cell}$), calculated as:

$$R_{cells} = R_{stack} - R_{blank} \tag{5.6}$$

The corrected current (I_{corr}) is equal to

$$I_{corr} = \frac{E_{stack,corr}}{R_u} \tag{5.7}$$

where R_u is the external load. Substituting eq. (5.7) into eq. (5.5), and finally in eqs. (5.2) and (5.3), the corrected power density ($P_{d,corr}$) is given by:

$$P_{d,corr} = \frac{OCV^2}{AR_u\left(1+\frac{R_{cells}}{R_u}\right)^2} \tag{5.8}$$

Eq. (5.8) evaluates the power density obtainable with a RED unit operating under the same conditions of the lab stack, but with a larger number of cell pairs (i.e. with a negligible effect of the blank resistance), thus allowing a prediction of power output potentials in scaled-up units.

Estimation of non-ohmic resistances

As a first estimation, the stack resistance of a RED unit can be evaluated as the sum of the ohmic resistances of membranes and bulk solutions. However, different non-ohmic losses can be identified, which are normally due to concentration polarisation phenomena and the effect of reducing driving force due to salt transport through IEMs [26,65].

In order to determine non-ohmic resistances, chronopotentiometric experiments have been performed [26,81]. Starting from the open-circuit condition, a constant current is applied to the system following a stepwise function, in which the current is interrupted between each step and the voltage response is recorded at a frequency of 25 Hz. This potential drop (Figure 5.5) can be attributed to two terms:

$$\Delta V_{tot} = \Delta V_{ohmic} + \Delta V_{non-ohmic} \tag{5.9}$$

The first (steep) voltage drop (ΔV_{ohmic}) is due to the ohmic resistance, i.e. membranes and bulk solutions; the following (time-dependent) voltage drop ($\Delta V_{non-ohmic}$) is attributed to non-ohmic phenomena (Figure 5.5).

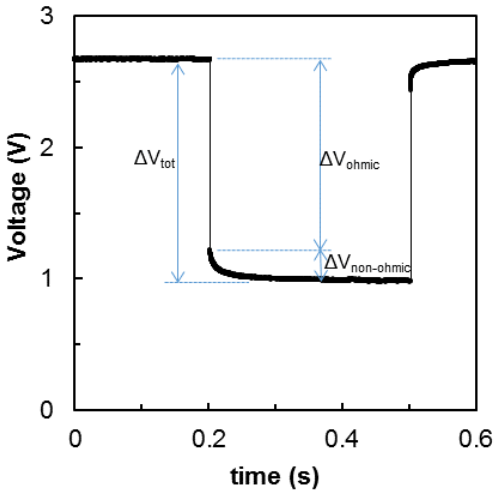

Figure 5.5. Voltage response during a chronopotentiometry test. 50 cell pairs stack equipped with Fujifilm (120 µm) membranes, 270 µm woven spacers. C_{HIGH} = 5 M; C_{LOW} = 0.5 M; T = 20°C; v = 0.3 cm/s. A single step current (I = 0.4 A) is shown as example.

Dividing each term in eq. (5.9) by the relevant current variation, the same relationship can be expressed in terms of resistances as:

$$R_{tot} = R_{ohmic} + R_{non-ohmic} \tag{5.10}$$

Each term in eq. (5.10) can be evaluated graphically as the ratio of voltage drop and current. The ohmic resistance was also theoretically estimated as:

$$R_{ohmic} = N\left(R_{HIGH} + R_{LOW} + R_{AEM} + R_{CEM}\right) + R_{blank} \tag{5.11}$$

where N is the number of cell pairs, R_{blank} is the blank resistance, R_{AEM} and R_{CEM} are the membranes resistance, R_{HIGH} and R_{LOW} are the contributions of concentrate and diluate, respectively.

Two different contributions can be identified in the non-ohmic resistance [26]:

$$\boldsymbol{R}_{non-ohmic} = \boldsymbol{R}_{BL} + \boldsymbol{R}_{\Delta C} \tag{5.12}$$

R_{BL} is the resistance due to the diffusion boundary layer, while $R_{\Delta C}$ is due to the reduction of the concentration gradient along the compartments (from inlet to outlet). The latter can be theoretically estimated by evaluating the cell voltage as:

$$E_{cell} = \beta\left(\alpha_{CEM} + \alpha_{AEM}\right)\frac{RT}{F} ln\left[\frac{\gamma_{HIGH}\, C_{HIGH}}{\gamma_{LOW}\, C_{LOW}}\right] \tag{5.13}$$

where R is the universal gas constant, T the absolute temperature, F the Faraday constant, α_{AEM} and α_{CEM} are the IEMs permselectivity, γ is the activity coefficient; β is a correction factor accounting for the effect of high salt concentration on permselectivity [82]. Therefore, the voltage drop due to concentration change within compartments ($\Delta V_{\Delta C}$) is given by:

$$\Delta V_{\Delta C} = \left(E_{cell}\right)_{in} - \left(E_{cell}\right)_{av} \tag{5.14}$$

where $(E_{cell})_{in}$ is the cell voltage calculated through eq. (5.13) at inlet conditions (corresponding to OCV), while $(E_{cell})_{av}$ is evaluated at inlet-outlet average concentrations. As a result, $R_{\Delta C}$ can be theoretically calculated, and R_{BL} can be estimated from eq. (5.12).

All the tests were performed in the range of 0 – 700 mA, with a current step of 100 mA. Each current value was applied for five minutes, in order to allow the system to reach equilibrium conditions. Voltage values were acquired by a data logger (DaqPRO©) at 25 Hz frequency.

5.3 Results and discussion

The influence of fluid flow velocity, feed solutions concentration and temperature on process performance was analysed for both sets of membranes tested. The investigated ranges were selected in order to fit the expected operating conditions for a pilot plant operating in a real environment, where brine is supplied from a saltworks basin (thus achieving saturation concentration and temperatures up to 40°C) and sea or brackish water from a shoreline well [29]. Furthermore, the first type of membranes (thickness 120 μm) was also used for a more detailed investigation, focusing on the effect of redox couple concentration on the power output. Finally, both sets of membranes were tested under the identified optimal conditions to maximise the power output. A summary of the experimental conditions in all tests is reported in Table 5.4.

Table 5.4. Summary of all tests performed in the experimental campaign.

Membrane type	Investigated variable	Investigated values
Fujifilm 120 µm	Flow velocity	v = 0.5 – 4.0 cm/s
	Concentrate (HIGH) concentration	C_{HIGH} = 1.0 – 5.0 M NaCl
	Diluate (LOW) concentration	C_{LOW} = 0.1 – 1.0 M NaCl
	Feed temperature	T = 20 – 40 °C
	Redox couple concentration	C_{ELEC} = 0.1 – 0.4 M
Fumasep 20 µm	Flow velocity	v = 0.5 – 4.0 cm/s,
	Diluate (LOW) concentration	C_{LOW} = 0.1 – 0.5 M NaCl
	Feed temperature	T = 20 – 35 °C
Fujifilm 120 µm	Optimal conditions	C_{HIGH} = 5.0 M NaCl, C_{LOW} = 0.1 M NaCl, T = 40 °C, v = 2 and 4 cm/s
Fumasep 20 µm		

5.3.1 Tests performed with thicker (120 µm) membranes

Influence of velocity

The fluid velocity (v) is defined as the mean feed flow velocity inside a single spacer-filled channel. It can be estimated as:

$$v = \frac{Q}{N\ \delta\ b\ \varepsilon_{sp}} \tag{5.15}$$

where Q is the total volumetric flow rate (l/h), N is the number of cell pairs (equal to 50), δ is the spacer thickness (270 µm), b is the compartment width (9.5 cm) and ε_{sp} is the spacer porosity (82.5% for the woven spacers used in this study).

Fluid velocity was varied from 0.5 to 4 cm/s in both dilute and concentrate compartments (Figure 5.6). The increase in fluid velocity slightly enhances the gross power density achieved in the stack. This is mainly due to the reduction in residence

time and the improvement of mixing phenomena inside compartments, although the latter play a minor role when seawater and brine are used [12].

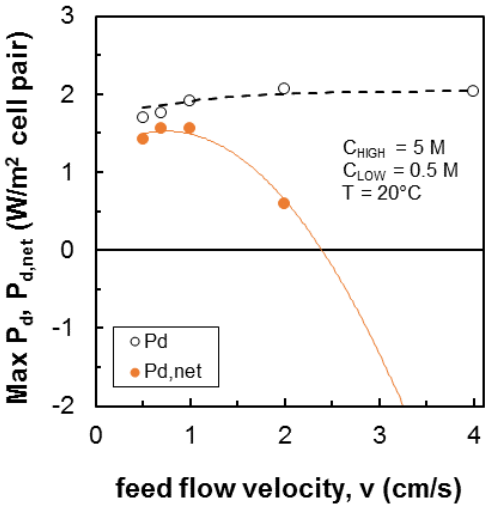

Figure 5.6. Effect of feed flow velocity on the measured gross and net power density. Experimental data for a 50 cell pairs stack equipped with Fujifilm (120 µm) membranes, 270 µm woven spacers. C_{HIGH} = 5 M; C_{LOW} = 0.5 M; T = 20°C. The net power density at 4 cm/s (-4.4 W/m^2) is not shown in the graph.

The most important influence is registered on the net power density, which dramatically falls for flow velocities above 1 cm/s due to the significant increase in hydraulic losses. In fact, the net power density becomes negative (i.e. the pumping power exceeding the gross power produced by the RED unit) for flow velocities between 2-3 cm/s. A flow velocity of 1 cm/s was found to give a good balance between gross and net power output, thus it was selected as the standard velocity for the reference tests.

Influence of salt concentration

The effect of the concentration of feed solutions was assessed in two different sets of experiments, changing the HIGH and LOW concentration alternatively. Figure 5.7 shows the influence of brine concentration (C_{HIGH}) on power density. As expected,

the increase in C_{HIGH} from 1 M to 5 M NaCl leads to an increase in power density. This is explained by the double beneficial effect of enhancing the process driving force (i.e. OCV) and reducing the stack resistance (Figure 5.7.A). In particular, the maximum gross power density achieved at C_{HIGH} = 5 M, corresponding to the standard conditions test, is around 2 W/m$^2_{\text{cell pair}}$. The net power density follows a similar trend, being consistently 0.5 W/m$^2_{\text{cell pair}}$ lower than the gross power density.

The apparent permselectivity can be calculated as the ratio between the measured OCV (Figure 5.7.A) and the theoretical OCV (evaluated by eq. 5.13 assuming ideal permselectivity). In this way, an apparent permselectivity varying between 0.8 and 0.4 was observed, passing from HIGH concentration of 1 M to 5 M NaCl. This highlights how IEMs lose their permselectivity when in contact with very concentrated brines, as already reported in previous literature works [11,57].

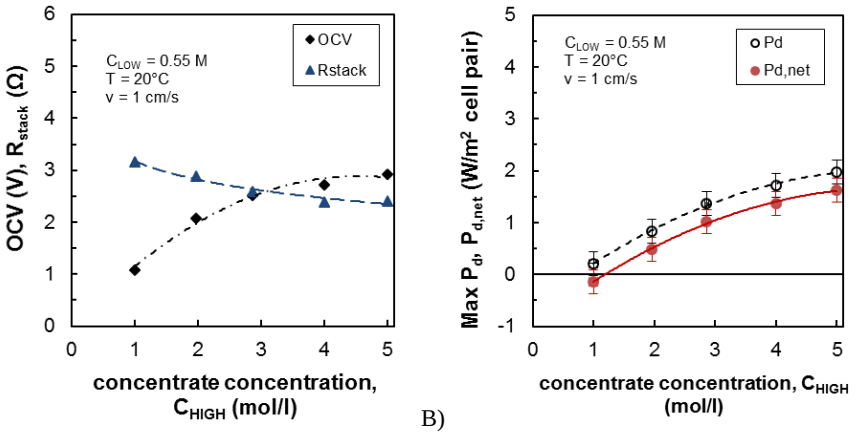

A) B)

Figure 5.7. Influence of concentration of concentrated solution (C_{HIGH}) on process performance. A) OCV and stack resistance. B) Net and gross power density. Experimental data for a 50 cell pairs stack equipped with Fujifilm (120 µm) membranes, 270 µm woven spacers. C_{LOW} = 0.55 M; T = 20°C, v = 1 cm/s.

A more interesting trend has been observed when the diluate concentration (C_{LOW}) was varied between 0.1 M and 1 M NaCl. Figure 5.8.B shows how lower C_{LOW} values lead to higher power densities, achieving a maximum of about 4.5 W/m$^2_{\text{cell pair}}$ at 0.1 M. When lowering C_{LOW} and keeping C_{HIGH} constant, two opposite effects arise: an increasing stack resistance and a higher stack potential (Figure 5.8.A). An optimal

value of C_{LOW} would result from a trade-off between these two effects, leading to a maximum of the curve slightly below 0.1 M NaCl [82]. However, such effect depends on the compartment thickness: using smaller thickness, the compartment resistance becomes less relevant than the membrane resistance. Therefore, the optimal C_{LOW} may shift towards lower values. Conversely, a smaller IEMs resistance makes the compartment resistance more relevant, thus likely moving the optimal C_{LOW} towards larger values. The apparent permselectivity is dramatically reduced by the presence of the extremely concentrated brine also in this case, ranging from values of 0.35 to 0.5 when passing from LOW concentration of 1 M to 0.1 M NaCl.

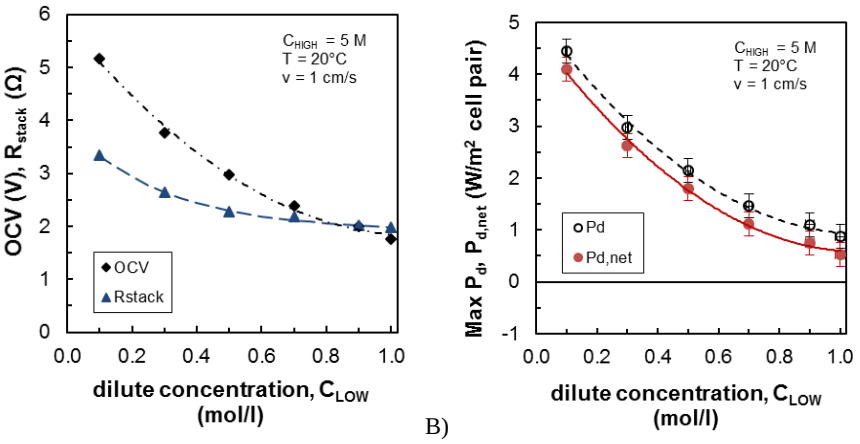

Figure 5.8. Influence of concentration of dilute solution (C_{LOW}) on process performance. A) OCV and stack resistance. B) Net and gross power density. Experimental data for a 50 cell pair stack equipped with Fujifilm (120 µm) membranes, 270 µm woven spacers. C_{HIGH} = 5 M; T = 20°C, v = 1 cm/s.

Influence of temperature

Starting from the standard conditions test (Table 5.3), the inlet temperature was increased to 30°C and 40°C. A 50% increase of both gross and net power density has been registered with respect to the standard conditions value (Figure 5.9). Such behaviour can be related to the strong dependence of membrane resistance on the system temperature, which can lead to a reduction between 30% and 50% when increasing the temperature from 20°C to 40°C [62]. This result clearly indicates a

promising way of enhancing the process performance when adopting brines from saltworks basins, typically operating at temperatures between 30°C and 40°C.

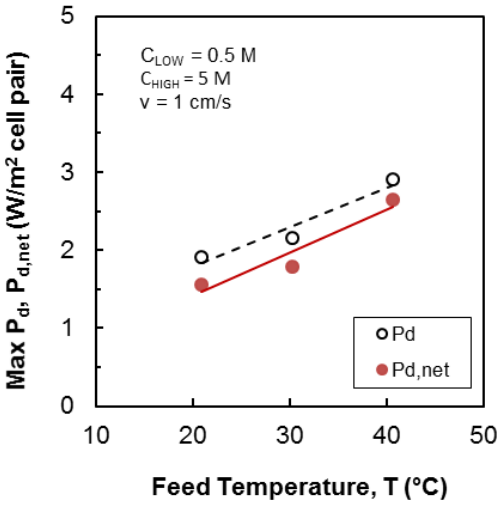

Figure 5.9. Influence of solutions temperature on the measured net and gross power density. Experimental data for a 50 cell pair stack equipped with Fujifilm (120 µm) membranes, 270 µm woven spacers. C_{HIGH} = 5 M; C_{LOW} = 0.5 M, v = 1 cm/s.

Influence of redox couple concentration

The influence of electrode compartments on process performance is usually neglected in large-scale electro-membrane processes. In fact, the relevance of electrode phenomena becomes less important when the number of cell pairs is higher than 200 [31]. Nevertheless, for laboratory-scale investigation with the use of small stacks and a reduced number of cell pairs, the characterisation of dependencies concerning the electrode compartment becomes crucial for understanding the stack behaviour. This analysis was performed by varying redox couple concentration (C_{ELEC}) from 0.1 M (standard) to 0.4 M (Figure 5.10).

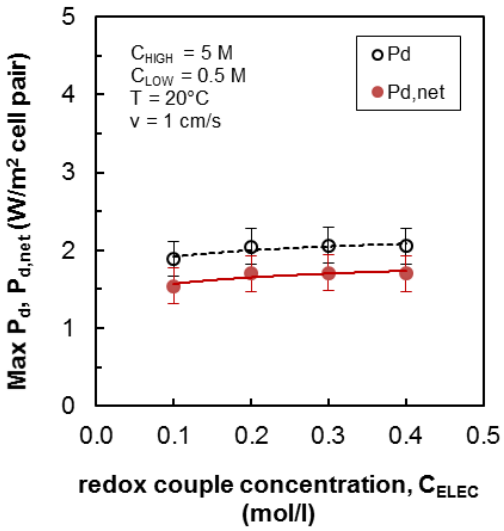

Figure 5.10. Influence of redox couple concentration (C_{ELEC}) in the electrode rinse solution on the measured net and gross power density. Experimental data for a 50 cell pair stack equipped with Fujifilm (120 µm) membranes, 270 µm woven spacers. C_{HIGH} = 5 M; C_{LOW} = 0.5 M, T = 20°C, v = 1 cm/s.

Figure 5.10 shows only a slight increase in power density passing from 0.1 M to 0.2 M, while beyond this point there is no positive effect from increasing the concentration. This is likely related to the slight increase in electrodes redox reaction kinetics, reducing the blank resistance of the system.

Such finding is not surprising, as the choice of redox couple concentration and ERS flow rate was done in order to keep a mass flow rate of redox couple in the electrodes compartments about 100 times larger than the reaction rate at the electrodes. Moreover, despite electrode kinetics in RED units are often controlled by mass transfer phenomena, the use of redox species concentration above 0.05 M can normally guarantee the minimisation of limiting current conditions [79], at least in the investigated operating conditions.

Evaluation of non-ohmic resistances

The chronopotentiometric measurements were performed at fluid velocities ranging from 0.3 up to 2 cm/s. Increasing the velocity, a reduction of the overall

resistance is initially observed (Figure 5.11.A), while the effect is negligible when the velocity is higher than 1 cm/s (see also Figure 5.6). The applied current only slightly affects the overall resistance. In particular, the ohmic resistance remains almost constant, thus the effect of current on the overall resistance is essentially related to the non-ohmic contributions (Figure 5.11.B).

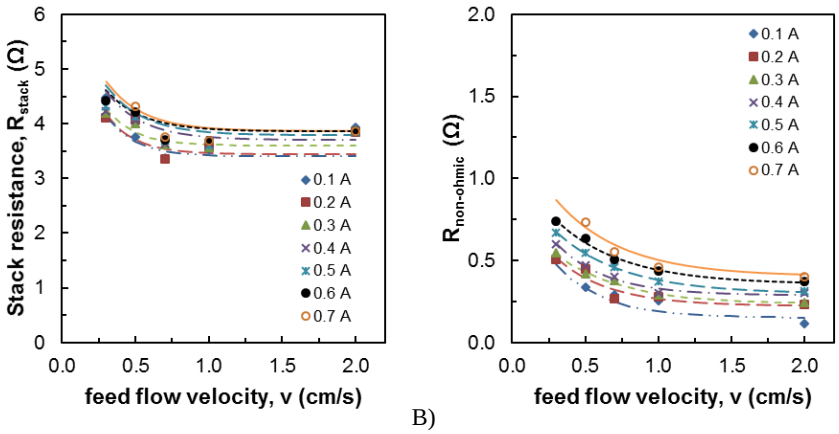

A) B)

Figure 5.11. Influence of fluid velocity and current density on ohmic and non-ohmic losses. Chronopotentiometry measurements on a 50 cell pairs stack equipped with Fujifilm (120 µm) membranes, 270 µm woven spacers. C_{HIGH} = 5 M; C_{LOW} = 0.5 M; T = 20°C. A) overall resistance. B) Non-ohmic losses.

When flow velocity increases from 0.3 up to 2 cm/s, the non-ohmic losses are estimated to be between 15 – 7% of the total resistance, respectively (Figure 5.11). In particular, $R_{non\text{-}ohmic}$ represents the 9% of the total resistance at 1 cm/s. This relatively low impact is due to the use of seawater and brine as feed solutions (instead of fresh water – seawater). In fact, when using such highly concentrated solutions, the effect of polarisation phenomena on process performance is rather negligible [12]. Conversely, when river water is used as diluate, the system is more sensible to concentration polarisation, thus resulting in a higher impact of the non-ohmic resistances [26].

The non-ohmic resistance due to the concentration change within compartments ($R_{\Delta C}$) was calculated through eq. (12-13). Therefore, the remaining part of $R_{non\text{-}ohmic}$ can be attributed to the diffusion boundary layer (R_{BL}). These contributions are shown

in detail in Figure 5.12, where a constant current of 600 mA was applied during the test. The theoretical evaluation of R_{ohmic} (eq. (10)) is also shown in the same plot (Figure 5.12.A).

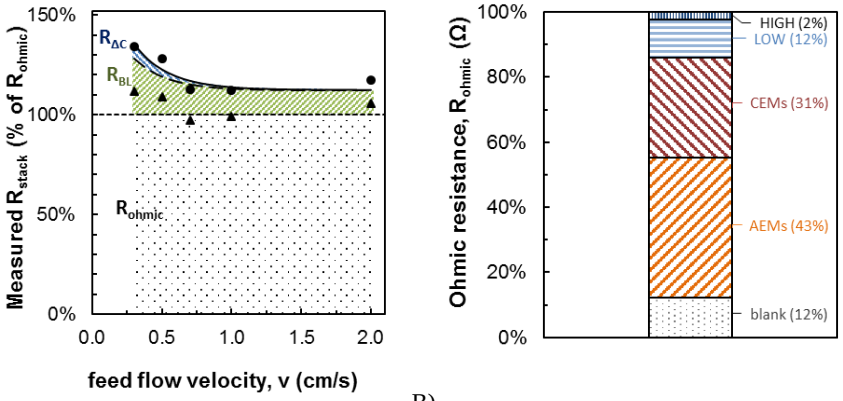

Figure 5.12. A) Measured resistance stack resistance as percentage of theoretical ohmic resistance. B) Theoretical estimation of ohmic resistance (evaluated according to eq. 5.11). Chronopotentiometry measurements on a 50 cell pairs stack equipped with Fujifilm (120 µm) membranes, 270 µm woven spacers. C_{HIGH} = 5 M; C_{LOW} = 0.5 M; T = 20°C; applied current: 600 mA.

For the sake of simplicity, the nominal value of membranes resistance (Table 5.2) were used for the theoretical estimation of R_{ohmic}, thus neglecting the effect of salt concentration on IEMs resistance. However, such influence is relevant especially when a very dilute solution (i.e. river water) is used for RED process [33].

Despite its simple approach, eq. (4.11) provided a good estimation of the ohmic resistance of the system (Figure 5.12). The good agreement with the experimental results clearly shows that both solutions and membranes resistances can be theoretically calculated with reasonable accuracy. It is worth noting that, using seawater and brine as feed solutions, the membranes resistance constitutes more than 70% of the ohmic resistance (Figure 5.12.B). Clearly, a reduction of these terms is desirable to reduce significantly the overall resistance.

5.3.2 Tests performed with thinner (20 µm) membranes

The second experimental study was carried out with the same stack and equipment, yet using a different type of membranes with lower thickness (20 µm). The three main dependencies on the fluid velocity, diluate feed concentration and temperature were analysed and results compared to the case of thicker membranes.

Influence of velocity

The effect of fluid velocity for a stack equipped with 20 µm-thick membranes is shown in Figure 5.13. The same trend of the first case (Figure 5.6) was observed, with an initial increase of the gross power density with the velocity up to 1 cm/s, and a subsequent plateau at higher flow rates. A further increase of the velocity beyond 2.5 cm/s gives a negative net power density (Figure 5.13.B).

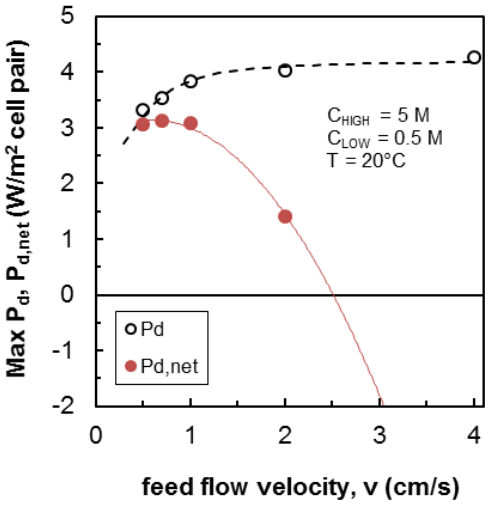

Figure 5.13. Effect of feed flow velocity on the measured gross and net power density. Experimental data for a 50 cell pairs stack equipped with Fumasep (20 µm) membranes, 270 µm woven spacers. C_{HIGH} = 5 M; C_{LOW} = 0.5 M; T = 20°C. The net power density at 4 cm/s (-6.7 W/m^2) is not shown in the graph.

Using 20 µm membranes, a more evident influence of velocity was registered, likely due to a more important effect of reduction in the non-ohmic resistances [26,83] given by the lower resistance of the membranes themselves.

Interestingly, a doubled power density was obtained compared to the use 120 µm-thick membranes in the same experimental conditions.

Influence of diluate concentration

Based on the results collected with the first set of membranes, only the effect of diluate concentration was further investigated for the 20 µm-thick membranes. In fact, the diluate concentration has a stronger impact on process performance. Therefore, the power measurements were performed using 5 M NaCl solution as concentrate, focusing on how the variation of diluate concentration can enhance the power output (Figure 5.14).

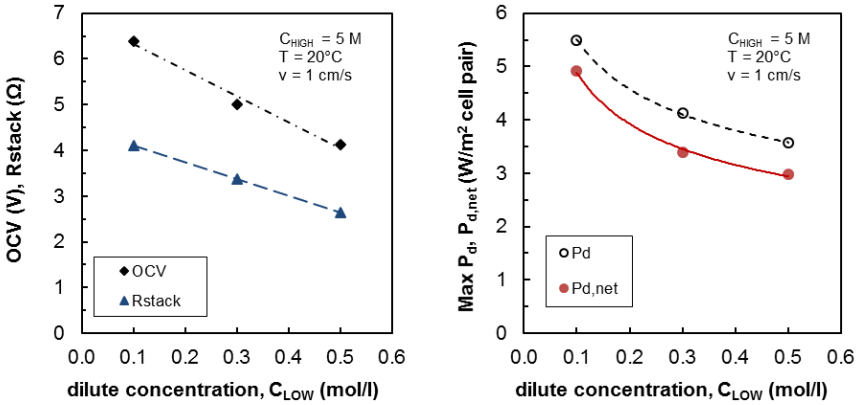

Figure 5.14. Influence of concentration of dilute solution (C_{LOW}) on process performance. A) OCV and stack resistance. B) Net and gross power density. Experimental data for a 50 cell pairs stack equipped with Fumasep (20 µm) membranes, 270 µm woven spacers. C_{HIGH} = 5 M, T = 20°C, v = 1 cm/s.

The dependence of stack resistance and OCV with the LOW concentration is reported, showing how reducing the diluate concentration leads to the counteracting effect of an increased stack resistance (Figure 5.14) and a higher OCV generated. As

in the previous case, the reduction in the diluate concentration leads to a continuous increase in the power output in the whole investigated range, with a maximum power density of 5.5 W/m^2 of cell pair achieved using 0.1 M NaCl solution, i.e. registering a 55% increase compared to standard conditions.

When comparing OCV values with those reported for the first set of membranes (Figure 5.8), these appear to be higher, thus indicating a better apparent permselectivity (i.e. roughly 0.6). This is in accordance with the IEMs specifications reported by suppliers for river water – seawater conditions (Table 5.2), though the presence of a highly concentrated brine dramatically reduces the nominal permselectivity.

Surprisingly, the measurements resulted in a stack resistance increase compared to the first set of membranes, notwithstanding the significant difference in thickness and in the nominal values of IEMs areal resistance. In fact, such nominal values are much lower for the thinner membranes in river water – seawater conditions (Table 5.2). This finding can likely be attributed to a different behaviour of the two membranes when in contact with highly concentrated solutions, which can generate swelling and ions sorption phenomena, affecting the ionic conductivity of the IEMs [62].

Influence of temperature

The effect of temperature was studied feeding the system in standard conditions at the different temperature of 20°C, 30°C and 35°C. In this case, a rough 40% increase of both gross and net power density was registered for temperature rising from 20 to 35°C, similarly to what found for the thicker membranes. In particular, comparing the results shown in Figure 5.15 with the previous case (Figure 5.9), it can be seen that the use of thinner membranes allowed to increase the produced power by 70-80% (from about 2.9 up to 5 W/ m^2 $_{\text{cell pair}}$) in similar operating conditions.

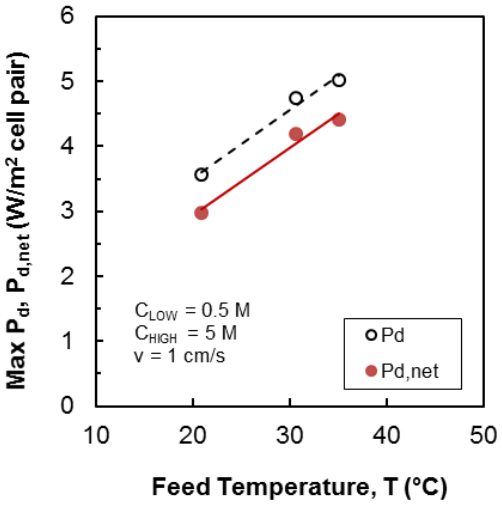

Figure 5.15. Influence of solutions temperature on the measured net and gross power density. Experimental data for a 50 cell pairs stack equipped with Fumasep (20 µm) membranes, 270 µm woven spacers. C_{HIGH} = 5 M, C_{LOW} = 0.5 M, v = 1 cm/s.

5.3.3 Investigating optimal conditions for maximum power

Based on the aforementioned results, a further test was performed aiming to the investigation of the performance of the RED system under the identified optimal operating conditions. In particular, both sets of membranes were tested using 0.1 M NaCl as dilute feed solution and 5 M NaCl as concentrate, with a feed temperature of 40°C and a fluid velocity of 2 and 4 cm/s. The concentration of redox couple in the electrode rinse solution was set to 0.3 M. Results of such tests are reported in Figure 5.16.

The values of power density reported in Figure 5.16 represent the real power output of the operating system. Moreover, the values of corrected power density have been estimated (as explained in par. 5.2.2) and are reported in the same plot, indicating the power output achievable by a stack with a larger number of cell pairs under the same operating conditions.

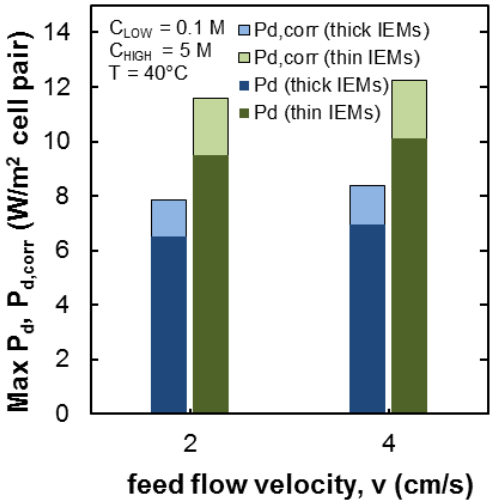

Figure 5.16. Investigation of optimal conditions for both sets of membranes: thick IEMs (Fujifilm 120 µm), thin IEMs (Fumasep 20 µm). Effect of feed flow velocity on power density (P_d) and corrected power density ($P_{d,corr}$). Experimental data for a 50 cell pairs stack equipped with 270 µm woven spacers. C_{HIGH} = 5 M; C_{LOW} = 0.1 M; T = 40°C. Redox couple concentration C_{ELEC} = 0.3 M.

Interestingly, a corrected power density of more than 8 W/m^2 of cell pair was observed with the thicker membranes. Moreover, using thinner membranes, a further increase was registered, reaching 12 W/m^2 of cell pair. Looking at the measured power density so far reported in the literature for RED systems (Figure 5.17), these results constitute the highest values so far achieved when operating a RED unit at temperatures up to 40°C.

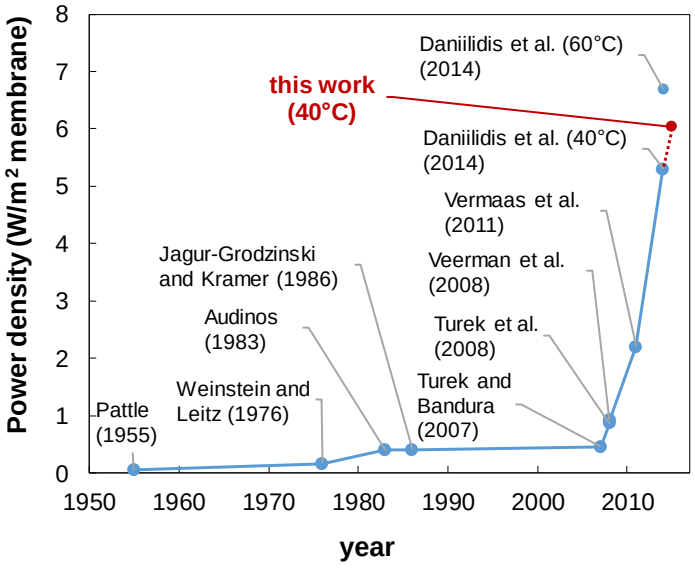

Figure 5.17. Power density (expressed as W/m^2 membrane) experimentally obtained in RED system. The maximum value achieved in this work is reported as a comparison with data from the literature. Sources: [14–21].

5.4 Outlook and final remarks

Focus of this work has been exploring the effect of different membranes and operating conditions on the performance of a lab-scale RED unit. Two different types of membranes were used, namely 120 µm-thick and 20 µm-thick membranes. A number of dependences have been analysed, in terms of fluid velocity (0.3 - 4.0 cm/s), feed temperature (20 – 40°C), and concentration of dilute (0.1 – 1 M) and concentrate (1 – 5 M).

For the first time in the open literature, a stack equipped with 50 cell pairs was tested under such operating conditions. These conditions were purposely selected to identify the best performance achievable in a pilot unit to be operated in a real environment with sea/brackish water and brines. The extensive tests allowed to quantify the effect of different process conditions on the overall performance in terms of both gross and net power density output.

Increasing the fluid velocity has been found to slightly increase the gross power output, though values above 2 cm/s often leads to unacceptable hydraulic losses. As a result, the optimal velocity can be identified in a range between 0.5 and 1 cm/s when adopting 270 µm spacers. A 50% increase in power output was observed passing from 20°C to 40°C feed temperature. A notable increase in power output was also observed reducing the dilute feed concentration from 0.5 M (i.e. seawater) to 0.1 M (brackish water), indicating this latter as the most suitable condition in the investigated range.

In all cases, the second set of membranes tested (20 µm-thick Fumasep FAS/FKS) led to an enhancement of power output between 70% and 100% compared to the first set of membranes (120 µm-thick Fujifilm AEM/CEM). However, the former gave rise to some crucial issues in the mechanical stability during the stack assembly, due to the extremely reduced thickness.

Finally, both IEMs sets were tested in the identified optimal operating conditions, i.e. 0.1 M NaCl and 5 M NaCl as feed solutions, 40°C and 4 cm/s fluid velocity. A power density of more than 8 W/m^2 of cell pair was reached with the first set of IEMs, and up to 12 W/m^2 of cell pair for the second set of membranes. Such results are among the highest values of power density so far obtained in reverse electrodialysis systems, and clearly demonstrate that a careful selection of process conditions and membranes properties can lead to a successful scale-up of the RED technology.

6 A RED PILOT PLANT FED WITH REAL BRINE: DESIGN, CONSTRUCTION AND START UP*

Abstract

Up to now, reverse electrodialysis has been broadly studied through laboratory experiments and modelling works, leading to significant improvements in the process performance. Therefore, a further scale-up is now required for testing the RED technology on real environment.

This chapter describes the activities carried out during the design, construction and start-up of the first RED pilot plant fed with real brackish water and saltworks brine. The plant, being built as the final accomplishment of the REAPower project, is located in a saltworks area in Marsala (Trapani, Italy). Such location is ideal for demonstrating the application of RED process in real environment, providing seawater, brackish water and concentrated brines as possible feed streams.

A first RED unit equipped with 125 cell pairs and 44x44 cm^2 membrane area was initially installed and tested. During the scale-up of the pilot plant, two larger units (44x44 cm^2, 500 cell pairs each) were afterwards installed in the same premises, then hydraulically connected in parallel with the first prototype.

The final configuration of the REAPower demonstration plant is constituted by three 44x44 cm^2 RED units, with more than 400 m^2 of total membrane area installed.

* Part of this chapter has been revised for publication as:

- M. Tedesco, D. Vaccari, A. Cipollina, A. Tamburini, G. Micale, *Operation and perspectives of the first pilot plant fed with brackish water and saltworks brines*, in preparation.
- M. Tedesco, D. Vaccari, A. Cipollina, A. Tamburini, G. Micale, *Performance analysis of the first reverse electrodialysis prototype plant operating with natural brackish water and saltworks brine,* in preparation.

6.1 State-of-the-art of RED process with natural solutions

Reverse electrodialysis has been already widely addressed as a promising technology to produce sustainable energy from salinity gradients. The potential of RED technology has been extensively demonstrated, both through experiments [14,16,17,19,20,44,84] and by modelling works [39,70,82,85,86].

Despite such notable literature, most of the studies presented so far are limited to the use of artificial river water (i.e. 0.017 M NaCl) and artificial seawater (0.5 M NaCl) as feed solutions, while very few examples are reported in the literature on the performance of RED process using natural solutions.

An experimental investigation in real environment has been recently performed at Wetsalt site in Harlingen (The Netherlands), using real fresh water and seawater on laboratory-scale RED units. Interestingly, a 40% reduction of the power output was observed during the first day of operation, when no pre-treatment was used except for a 20 μm filter [52]. The main cause of such performance reduction was attributed to colloidal and organic fouling, which is especially crucial for AEMs, being such foulants composed of large anions. The adoption of anti-fouling strategies is therefore necessary to ensure a suitable pre-treatment of such natural streams. With this regard, periodic air sparging and switching of feed streams have been proposed as valuable methods to reduce colloidal fouling [51].

The experimental campaign performed in Harlingen showed interesting sights on fouling phenomena in real environment. However, such campaign does not provide information on the scale-up of the RED technology, as only lab-scale RED units (10x10 cm^2, 5 cell pairs) were tested [51,52]. In fact, most of the experimental works on RED process reported so far are based on the use of small stacks (10x10 cm^2 active membrane area) with relatively low number of cell pairs (typically, 5-10, up to 50 [20]). The only exception of scaled-up unit is a RED stack with 75x25 cm^2 membrane area and 50 cell pairs reported by Post [36] and Veerman [87]: the unit was tested with artificial river water and seawater, showing a power output of 16 W (i.e. 0.6 W/m^2 of membrane area) [36].

The largest pilot-scale installation of RED process is the “Blue Energy” plant constructed by REDstack BV (The Netherlands). This pilot plant is located on the

Afsluitdijk, a 32 km-long dyke that separates the Ijssel Lake from the Wadden Sea. Such location provides both seawater (~28 g/l) and fresh water (0.2-0.5 g/l) as feed streams, while the outlet brackish water from the RED plant can be discharged directly into the sea. The only published information on the plant has been reported by Post et al. [36] in 2010, i.e. when the pilot was still in its early construction stage. According to the available information, the Blue Energy plant can be fed with seawater and fresh water at 220 m^3/h flow rate, with an expected power target capacity of 50 kW: this would require the installation of 100,000 m^2 of membranes with the current state-of-the-art power density. On the other hand, the Blue Energy plant has been officially opened in November 2014, and no data have been publicly reported to date.

Up to now, the effect of natural solutions on the performance of RED process is almost unexplored, though some recent studies have been focused on the effect of multivalent ions. In fact, apart from sodium chloride, natural solutions contain other salts affecting the behaviour of ion exchange membranes and, therefore, the performance of RED process. In particular, bivalent ions such as Mg^{2+}, Ca^{2+}, SO_4^{2-}, have lower mobility inside IEMs, thus increase the membranes resistance [88]. For this reason, new mono-selective IEMs for RED process has been proposed to overcome such limitation, although these membranes are still in their early stage of development [89].

The effect of bivalent ions on RED performance has been recently investigated by Vermaas [90]. In particular, adding 10% $MgSO_4$ to the NaCl feed solutions, a power reduction ranging from 29 up to 50% (depending on membrane type) was observed [90]. The worst situation was registered using thicker membranes: this might be seen as a further clue that very thin membranes are preferable for RED applications [84].

Besides the use of seawater and fresh water, using highly concentrated solutions has been proven to enhance the performance of RED technology [21,70,91]. In fact, the use of seawater (or brackish) water and concentrated brines allows to reduce significantly the electrical resistance of the RED stack, therefore increasing the power output. This concept has been on the basis of the REAPower project [29], whose main

goal was to demonstrate the potential of RED process using concentrated brines and brackish water in a real environment.

The effect of such highly concentrated solutions on power density has been investigated on laboratory-scale tests by Tufa et al. [92]. Using artificial brackish water and brine with the same salt composition of real solutions, Tufa measured a 63% reduction in power density with respect to the reference case (0.1 M NaCl – 5 M NaCl) [92]. The main effect was attributed to the presence of Mg^{2+} ions, which drastically increase the overall resistance. On the other hand, magnesium was the most abundant cation aside from sodium in the brine, and the only bivalent ion present in relatively large amount.

As final accomplishment of the REAPower project, a RED pilot plant has been designed and constructed in a saltworks area in Marsala (Italy) to demonstrate the potential of RED process using concentrated brine. Such location provides both seawater and brackish water (from a shoreline well) as dilute solution, and saturated brine from saltworks as concentrate.

This chapter describes the R&D activities involved during the design, construction and start-up of the REAPower demonstration plant. A first prototype of 44x44 cm^2 single membrane active area equipped with 125 cell pairs has been initially installed and tested, using both real solutions (brine and brackish water) and artificial NaCl solutions. During the plant scale-up, two larger units have been installed later, thus reaching a final configuration of three RED modules with more than 400 m^2 of total membrane area. In this way, the REAPower plant represents in fact the largest RED installation currently operating in a real environment, as well as the first RED prototype installation using brackish water and brine.

6.2 The installation site: the Ettore-Infersa saltworks in Marsala

The Ettore-Infersa saltworks in Marsala (Trapani, Italy) represent an ideal area for demonstrating the feasibility of RED technology with highly concentrated solutions (Figure 6.1). This natural environment, situated on the west coast of Sicily, is one of the most important areas in the Mediterranean Sea for sea-salt production.

A saltworks is a delicate natural environment in which seawater is collected in several large basins, in order to create concentrated brine by evaporation and eventually crystallise sodium chloride with purity above 97%, i.e. food-grade or industrial-grade salt. Thanks to the evaporation caused by sun energy and wind, the seawater flowing through the basins increases its salt concentration, until reaching the saturation point of sodium chloride in the last basins. Salt solutions flow through the ponds mainly driven by gravity or small low-prevalence pumps, while the flow distribution is regulated by means of small canals and gates. A careful flow regulation is necessary to ensure that salts different from sodium chloride, such as calcium sulphates and carbonates, precipitate in the "preparation basins", thus achieving in the last basins the saturation for NaCl only. The final product has a purity in NaCl higher than 97% [28].

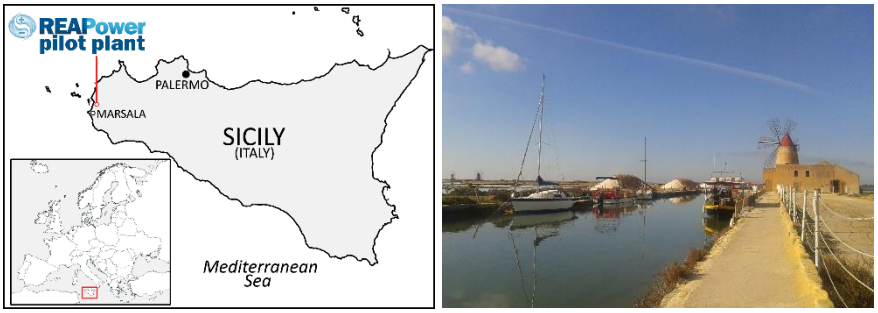

Figure 6.1. Location of the REAPower pilot plant in Marsala (Italy). A picture of the windmill hosting the RED units is shown on the right.

Clearly, any saltworks area is a feasible location for salinity gradient power production, providing a large amount of both solutions required, i.e. seawater and saturated brine. In particular, the Ettore-Infersa saltworks in Marsala has been selected as installation site of the REAPower pilot plant also for the presence of brackish water, which is available from a shoreline well situated in the same location. In fact, the use of brackish water is preferable to optimise the salinity gradient for power production [82]. Furthermore, brackish water in this environment is generally rather clean and practically free of suspended solids (Table 6.1), thus requiring minor pre-treatments, especially compared to what normally required by seawater.

The REAPower plant has been designed to take into account both seawater and brackish water as possible feed solutions (Figure 6.2). The RED unit can be fed with either sea or brackish water (or both solutions, reaching a more concentrated brackish water). The saturated brine is taken from four dedicated ponds, which are not involved in the salt production cycle of the saltworks.

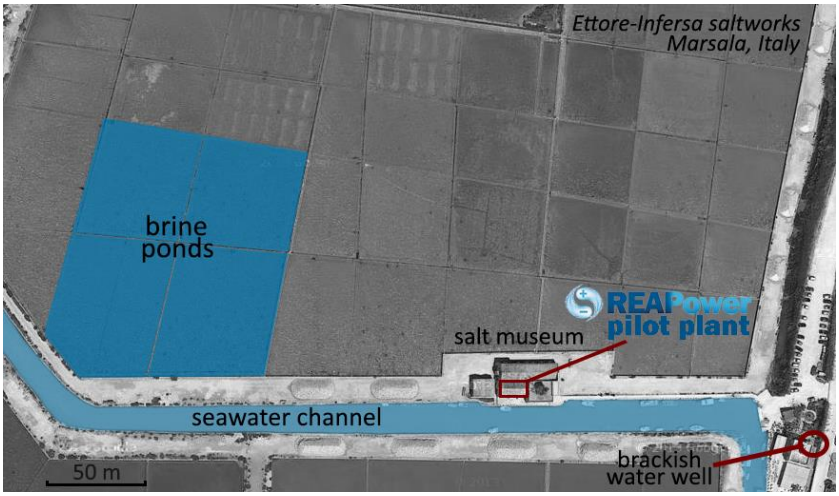

Figure 6.2. Satellite image of the REAPower plant installation site (*Ettore-Infersa* saltworks, Marsala, Italy). Three different solutions are available for power production by RED: saturated brine from ponds, seawater from an open channel and brackish water from a shoreline well.

The composition of brine, seawater and brackish water in Marsala are reported in Table 6.1. The brine concentration ranges between 4 and 5 M NaCl, according to the period of the year: a saturated solution is available in summer, while during winter the brine is slightly diluted by rainfalls. Conversely, the conductivity of brackish water is rather stable, equivalent to a 0.03 M NaCl solution.

Table 6.1. Composition of natural solutions at the REAPower plant in Marsala (Italy).

Solution	**Conductivity (mS/cm)**	**Molarity[a] (mol/l)**	**Suspended solids concentrations (mg/l)**
Brine	160-220	4-5	20
Seawater	49	0.5	74-200
Brackish water	3.4	0.03	-

[a] Apparent molarity calculated from measured conductivity assuming that only NaCl is present.

Although the plant accounts also for a seawater intake (Figure 6.3), seawater was used only during the commissioning and start-up phases, while the whole experimental campaign was performed using brackish water and brine as feed solutions. In fact, brackish water presents a number of advantages with respect to seawater, both in terms of salt concentration and amount of suspended matter. In particular, both model predictions [82,91] and laboratory experiments (Chapter 5) demonstrated that brackish water has a more suitable concentration to enhance the power output from RED systems. Moreover, brackish water (coming from a shoreline well) was practically free of suspended matter, while the quality of seawater was affected by the presence of very fine sand/clay particles from the bottom of the channel.

The ion composition of brine and brackish water is reported in Table 6.2. As shown in the table, a small amount of bivalent cations (Mg^{2+}, Ca^{2+}) was also found in brackish water.

Table 6.2. Ion composition of brackish water and brine in Marsala, Italy (expressed as mg/l). Adapted from: [92].

Solution	Na^+	K^+	Ca^{2+}	Mg^{2+}	Cl^-	HCO_3^-	SO_4^{2-}
Brackish water	1520	49.7	101	323	3560	0.523	335
Brine	66000	7740	242	37400	170000	50.0	64400

6.3 Plant design

Figure 6.3 shows the process flow diagram (PFD) of the REAPower pilot plant. The RED units and instrumentation are installed within a restructured old windmill that hosts today a salt Museum (Figure 6.1). Other plant facilities, such as storage tanks for brackish water, diluate filtration section and seawater intake pump, are installed in a warehouse near the main building.

The pilot plant was originally designed taking into account three intake lines (on the left in Figure 6.3). In particular, two intake pumps for seawater and for brine have been installed, while a direct connection from the well is used for brackish water. The dilute feed solution is firstly sent to a filtration section, then to two storage vessels (4 m^3 of total capacity) installed within the salt warehouse (Figure 6.3). These tanks ensure a proper availability of diluate when the system is fed with brackish water.

The brine filtration section is installed directly into the main building, where the RED prototypes are installed. The installation of storage tanks for brine was not necessary, thanks to the constant availability of brine from the basins. Two small buffer tanks (125 l capacity) for diluate and concentrate are positioned just before the main pumps feeding the saline solutions at the inlet of the RED unit.

All the external polyethylene pipelines were installed to guarantee the lowest visibility, being the site a natural reserve and protected area. The longest pipelines of

the plant are the brine intake/discharge lines, and the brackish water intake (roughly 200 m long each).

6.4 Installation of RED units and plant facilities

6.4.1 Reverse electrodialysis stacks

Three RED units with 44x44 cm^2 membrane active area and cross-flow arrangement were installed in the plant (REDstack BV, The Netherlands). Each prototype is equipped with ion exchange membranes purposely developed for highly concentrated solutions (Fujifilm Manufacturing Europe BV, The Netherlands). The main properties of such membranes are listed in Table 6.3.

Table 6.3. Physical properties of Fujifilm ion exchange membranes installed in the REAPower pilot plant.

Membrane	**Thickness, µm**	**Permselectivity (0.5 M - 4 M)**	**Electrical resistance, Ω cm^2**	**Hydraulic permeability, ml/bar h m^2**
AEM 80045-01	120	0.65	1.55	4.96
CEM 80050-04	120	0.90	2.96	4.72

All the stacks contain 270 µm woven spacers with integrated gaskets (provided by Deukum GmbH, Germany). Such spacer thickness and geometry were selected on the basis of CFD modelling predictions, in order to ensure a trade-off between reducing pressure drops and enhancing mass transfer phenomena [12,77].

The main difference among the RED units is the number of cell pairs used for each units. The relevant properties of each RED prototype are listed in Table 6.4.

Table 6.4. RED units installed in the REAPower pilot plant in Marsala.

RED unit	Membrane area (cm^2)	Cell pairs	Total cell pair area (m^2)
Small prototype (STACK 1)	44x44	125	24
1st Large prototype (STACK 2)	44x44	500	97
2nd Large prototype (STACK 3)	44x44	500	97

The electrode compartments of each RED unit contain four segmented electrodes made by Ru-Ir oxide coated Ti mesh (Magneto Special Anodes BV, The Netherlands). The electrode rinse solution (ERS) was selected in order to ensure the minimum environmental impact in the unlikely case of leakage from the electrode compartments into the diluate/concentrate compartments. For this reason, hexacyanoferrate compounds were avoided, although widely adopted for RED technology on laboratory-scale for their properties [13]. Conversely, iron salts ($FeCl_2/FeCl_3$) have been identified as suitable redox couple for such delicate environment [35]. Therefore, an aqueous solution of 0.3 M $FeCl_2$, 0.3 M $FeCl_3$ and 2.5 M NaCl as supporting electrolyte was used as electrode rinse solution. A small amount of HCl was added to keep the pH in the range of 2-3 and avoid precipitation of iron compounds [47].

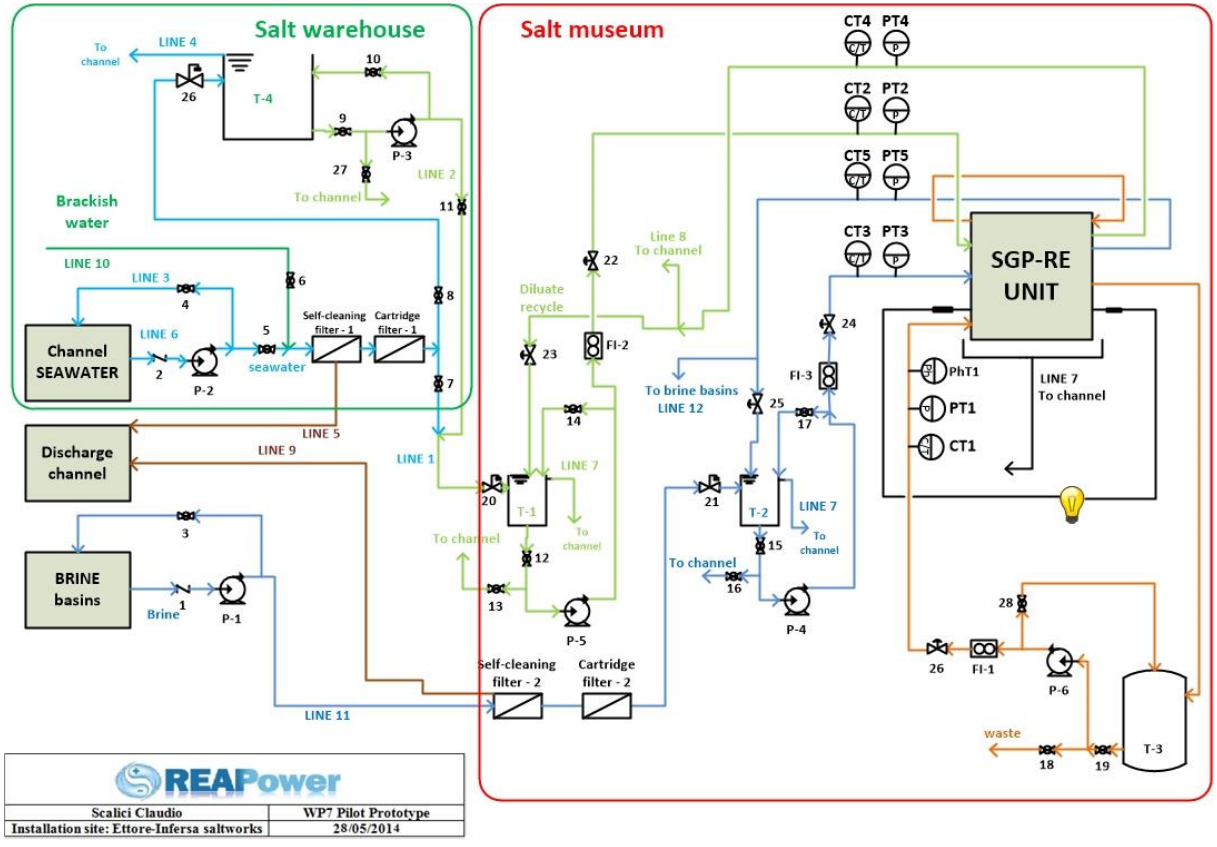

Figure 6.3. Process flow diagram of the REAPower pilot plant.

6.4.2 Pre-treatment section

As the only pre-treatment stage, two filtration units were installed, for dilute solution (sea or brackish water) and brine, respectively. Each filtration unit is equipped with a 50 µm cleanable filter and two cartridge filters of 25 µm and 5 µm.

During the plant commissioning, the filtration unit was tested measuring the flow rates for seawater and brine with/without filters (i.e. bypassing the filtration section). The dirtiest filter was the 25 µm cartridge filter. Therefore, the suspended particles in seawater have likely an average size between 50-25 µm. Conversely, brackish water was significantly clean and practically free of suspended matter. For this reason, the use of brackish water was preferred as diluate instead of seawater, in order to reduce the risk of fouling in the system.

A shocking treatment with sodium hypochlorite (5 ppm dosing, once per week) was implemented in the diluate storage tanks. This allows to prevent the growth of bio-fouling on the membranes facing the diluate compartments. The hypochlorite dosing was not necessary for brine, as bio-fouling is inhibited by the high salt concentration itself.

6.4.3 Pumps and instrumentation

Three centrifugal pumps with variable speed (Schmitt MPN 130, Kreiselpumpen GmbH & Co.KG, Germany) were used to feed all solutions (i.e. concentrate, diluate and ERS) to the RED units. Membrane pumps (Shurflo SH-4111-03) were adopted for pumping the diluate from the 4 m^3 storage vessels to the buffer tank in the main building. A similar pump was used for the seawater intake.

The brine from the ponds is pumped directly into the buffer tank placed in the main building using an immersed pump (centrifugal pump with open impeller), which is installed near the brine intake. The use of such pump, suitable for pumping solutions with suspended matter, was necessary during summer, when the brine reaches the saturation point and salt precipitation occurred. In fact, salt crystals were sucked by

the pump with the brine and blocked only in the filters, which required frequent filters washing to avoid their complete plugging by precipitated NaCl.

The measuring instrumentation is constituted by temperature/conductivity sensors/transmitters (Jumo CTI-500) and pressure transducers (Jumo Midas SW) for both inlet/outlet solutions. The inlet flow rate of both concentrate and diluate were measured by magnetic flowmeters (Khrone IFC 100 C). The properties of electrode rinse solution were also monitored in terms of conductivity, temperature, flow rate and pH by the same type of instrument. The stack voltage was acquired by a data logger, while the external current was measured by an external amperometer.

Figure 6.4. Front-end panel of the supporting tray. Five pipelines can be identified: HIGH inlet (1), LOW inlet (2), HIGH outlet (3), LOW outlet (4), ERS (5). A laboratory unit (22x22 cm^2, 109 cell pairs) and the small prototype (44x44 cm^2, 125 cell pairs) are shown on the tray.

The pumps, pipings and instrumentation were all installed on a compact supporting structure purposely designed for placing the small prototype (Figure 6.4). The front-end panel of the supporting tray is constituted by five separated pipelines, for inlet/outlet concentrate, inlet/outlet diluate and inlet electrode rinse solution.

The final view of the three RED prototypes installed in the salt museum is shown in Figure 6.5. The small prototype is placed on the supporting tray, and is hydraulically connected in parallel with the two larger units. The large prototypes are installed in the same room (Figure 6.5.B), and positioned on separated supporting trays.

After the plant start-up (March – April 2014), an experimental campaign over a period of six months (May – October 2014) has been performed at the REAPower pilot plant. The main results achieved will be described in details in the following chapter.

Figure 6.5. Final view of the REAPower demonstration plant. A) The small prototype (44x44 cm^2, 125 cell pairs) is visible on the left, on the supporting tray. B) Large prototypes (44x44 cm^2, 500 cell pairs) installed within PP boxes.

7 RED PILOT PLANT FED WITH REAL BRINE: OPERATION AND RESULTS*

Abstract

This chapter describes the experimental campaign carried out on the REAPower demonstration plant (Marsala, Italy) over a period of six months. A small prototype (44x44 cm^2, 125 cell pairs) has been initially tested with real brackish water (equivalent to 0.03 M NaCl) and saturated brine (~5 M NaCl), reaching a power output of 40 W (i.e. 1.4 W/m^2 of cell pair). Testing the prototype with artificial solutions, an increase of the power output up to 66 W (2.7 W/m^2 cell pair) was observed. Overall, the small prototype has been operating for five months without showing significant performance losses.

The plant was later scaled up through the installation of two larger prototypes (500 cell pairs each). These units were tested singularly and in parallel, using both real solutions (brackish water and brine) and artificial solutions. The overall capacity registered for the plant was almost 700 W using artificial solutions with the same conductivity of natural streams. Using real brine and brackish water, a power output of nearly 330 W was reached. Such reduction can be mainly attributed to the presence of different ions (especially Mg^{2+}) in the natural feed, thus indicating that Mg^{2+} removal could be necessary for improving future RED applications.

The experimental campaign reported in this chapter represents the first demonstration of power production from concentrated brines in a real environment, thus giving useful indications for the spreading of RED technology in the near future.

* Part of this chapter has been revised for publication as:

- M. Tedesco, D. Vaccari, A. Cipollina, A. Tamburini, G. Micale, *Operation and perspectives of the first pilot plant fed with brackish water and saltworks brines*, in preparation.
- M. Tedesco, D. Vaccari, A. Cipollina, A. Tamburini, G. Micale, *Performance analysis of the first reverse electrodialysis prototype plant operating with natural brackish water and saltworks brine,* in preparation.

7.1 Overview of the experimental campaign with small prototype

The start-up of the REAPower pilot plant was carried out using a laboratory RED unit (22x22 cm^2, 109 cell pairs) in March 2014. This was useful to check the proper operation for all auxiliary systems, before going through the installation and testing of the first prototype. Therefore, the first ("small") prototype with a membrane active area of 44x44 cm^2 and equipped with 125 cell pairs was delivered and installed on site. Such prototype has been exploited for the main experimental campaign. Aiming at the plant scale-up, two larger RED units with same membrane area and higher number of cell pairs have been installed and tested afterwards.

The RED systems were tested with both natural solutions (i.e. brackish water and brine) and with artificial NaCl solutions. In all cases, the system performance in terms of power generation was investigated connecting the RED units with an external load.

The power measurements were performed under both constant load and variable load conditions, in order to study the entire operating curve. For testing the small prototype, the external load was constituted by a variable resistor (0 – 22 Ω) in parallel with five lamps (10 V each).

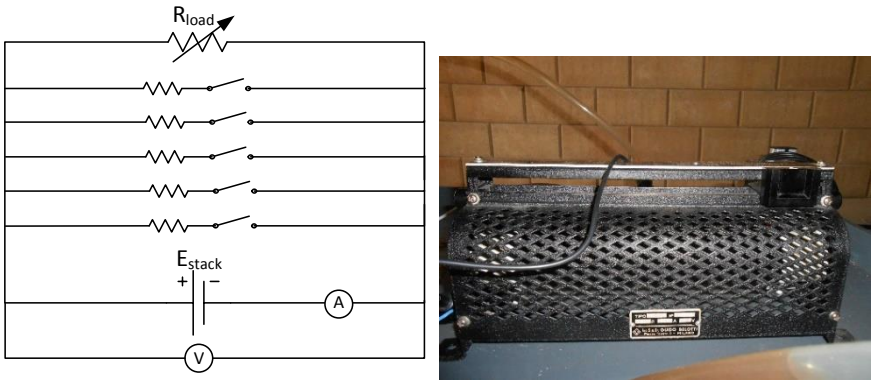

Figure 7.1. Schematic representation and picture of the variable resistor (R_{load} = 0 – 22 Ω) used for power measurements with the small prototype. Five lamps (10 V each) were connected in parallel to the variable resistor to increase the accuracy in the range of maximum power output (1 – 2 Ω).

The presence of a parallel external resistance allowed to reduce the current passing through the variable resistor, thus increasing the accuracy in the range of maximum power output, i.e. when the external resistance is equal to the stack resistance [20].

The stack voltage and all the properties of solutions (conductivity, temperature, inlet flow rates, and pressure drop) were collected by the acquisition system (LabVIEW™, National Instruments, USA) at a frequency of 1 Hz. The electric current was measured by an external amperometer, while the power output was determined by Ohm's law ($P = E_{stack} \cdot I$). The collected data were afterwards post-processed using Matlab™.

7.2 Power measurements with natural solutions

The first power test was performed using real solutions (brackish water and brine) and assuming a flow rate of 8 l/min for both streams, i.e. a fluid velocity inside compartments of ~1 cm/s. Results collected during a typical measurement are shown in Figure 7.2, where all the monitored process variables are shown as a function of the time.

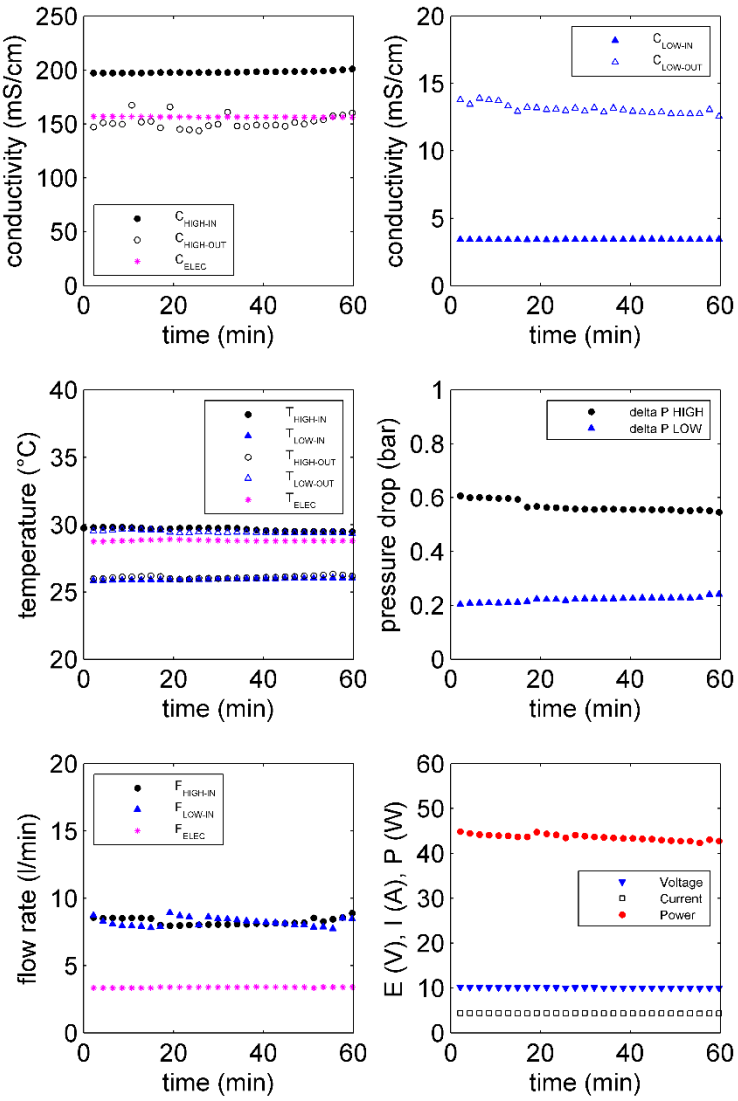

Figure 7.2. Variables collected by the system during the measurements. Power measurement performed with real brackish water and brine under constant load conditions (external resistance: 2.3 Ω). Feed flow rate: 8 l/min (i.e. ~1 cm/s fluid flow velocity).

7.2.1 Influence of flow distribution

The distribution manifolds of the small prototype are constituted by rectangular ducts with six inlet-outlet holes. Both solutions are fed to the stack from the bottom, and flow through the unit in a cross-flow arrangement until reaching the outlet collectors above the RED unit. Such configuration was designed to reduce pressure drops inside the channels and facilitate air bubble removal.

Despite such precautions, a non-uniform flow distribution was observed from the outlet manifolds during the first tests using a nominal flow velocity of 1 cm/s. In particular, both streams flew out mainly from the lowest manifolds, leaving the highest manifolds completely empty. This phenomenon can be attributed to a non-uniform flow distribution inside the spacer-filled channels of the RED unit.

In order to improve the internal flow distribution, a new system of valves was installed at inlet-outlet manifolds. In this way, the flow rate from each duct was manually controlled to ensure a complete filling of the RED unit. Moreover, an air purge system was installed above the outlet manifolds.

The effect of a non-uniform flow distribution was investigated by using the new system. Figure 7.3 shows a power measurement performed under the original (non-optimal) flow conditions and the improved situations.

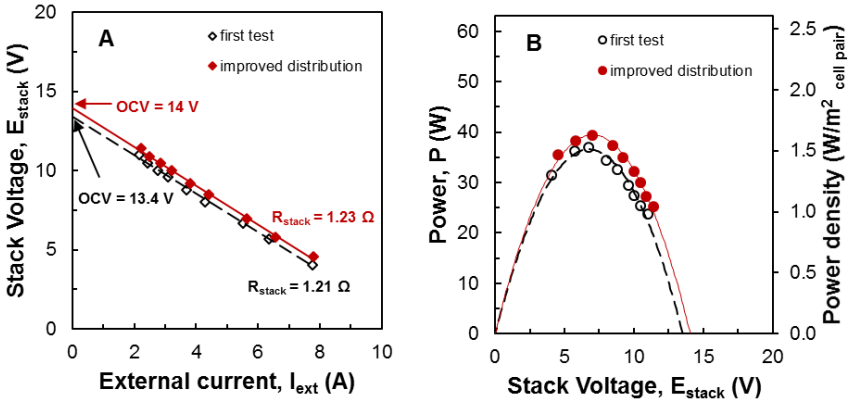

Figure 7.3. Influence of flow distribution on power output. First test: standard conditions. Improved distribution: improving the flow rate distribution by the inlet-outlet plugs. Power measurements performed feeding the prototype (44x44 cm^2, 125 cell pairs) with brackish water (3.4 mS/cm) and brine (170 mS/cm). Flow rate: 8 l/min (i.e. 1 cm/s fluid velocity).

Improving the internal flow distribution, a slight increase (5-10%) in the power production was obtained. This demonstrates that a further investigation of the internal flow distribution may lead to an improvement in the stack performance.

7.2.2 Effect of feed flow rates on power output

A number of tests were also performed to investigate the effect of both dilute and concentrate flow rates. Figure 7.4 shows the effect of increasing flow rates (for LOW and HIGH) on both power and power density.

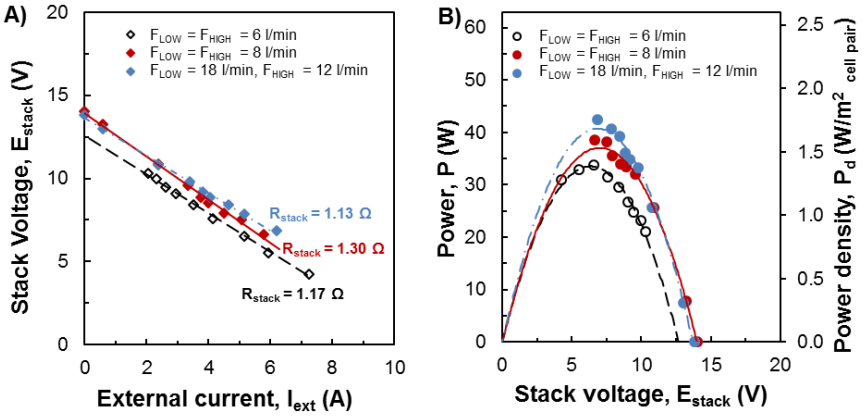

Figure 7.4. Influence of feed flow rates on process performance. Power measurements performed feeding the small prototype (44x44 cm^2, 125 cell pairs) with brine (196 ± 11 mS/cm) and brackish water (3.4 ± 0.1 mS/cm).

Using a feed flow rate of 18 l/min (i.e. ~2.2 cm/s feed flow velocity), a power output of 43 W was reached, i.e. almost 30% increase with respect to the case at lowest flow rates (6 l/min). The effect of increasing power is also due to the lower residence time of solutions inside stack, leading to a higher OCV (Figure 7.4.A). On the other hand, suitable flow rates for practical applications are limited by the pressure drops inside the stack. In this case, at the maximum investigated flow rate (Q_{LOW} = 18 l/min), a flow rate higher than 12 l/min was avoided in the brine compartments in order to keep the pressure drop below 1 bar, as suggested by the stack manufacturer. In particular, in that case pressure drops were 0.7 and 0.9 bar for diluate and concentrate, respectively.

7.2.3 Effect of flow rate of the electrode rinse solution

Aside from diluate/concentrate flow rates, also the flow conditions for the electrode rinse solution (F_{ERS}) can affect the power output from the system. Such phenomenon was experimentally observed increasing the flow rate for ERS from the design value (2.5 l/min) up to 4 l/min (Figure 7.5).

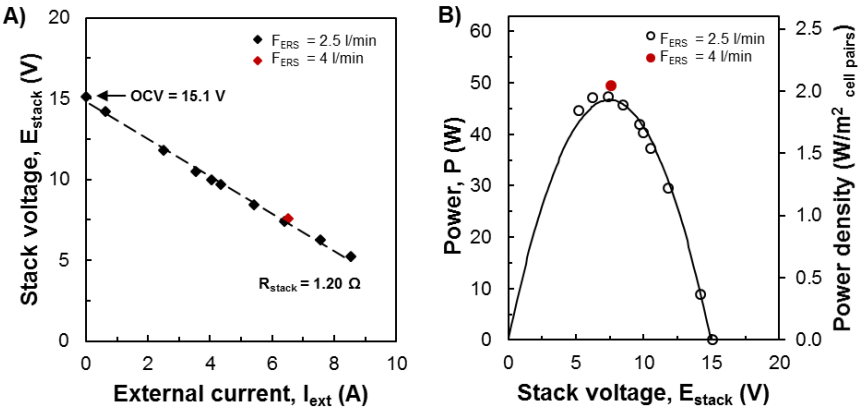

Figure 7.5. Effect of flow rate of the electrode rinse solution (F_{ERS}) on power output. Power measurements performed feeding the prototype with brine (210 mS/cm) and brackish water (3.4 mS/cm). Flow rate: 8 l/min (i.e. 1 cm/s flow velocity).

Although an increase in the power output has been observed using an ERS flow rate of 4 l/min, a higher flow rate in the electrode compartments is not recommended due to the high local pressure drops. In particular, increasing the flow rate in the electrode compartments from 2.5 to 4 l/min, pressure drop increased from 0.4 up to 0.7 bar, i.e. becoming comparable with the pressure drop in the diluate compartments. For this reason, the ERS flow rate was always kept in the range of 2-3 l/min, in order to reduce the risk of internal leakage towards the saline solutions compartments.

7.3 Power measurements with artificial solutions

Aside from the operation with real brine and brackish water, the RED system was also tested with artificial solutions, aiming to characterise quantitatively the effect of natural streams on process performance. For this purpose, artificial solutions were prepared using tap water and sea-salt from the saltworks, in order to reach the same conductivity of real brine (200-220 mS/cm) and brackish water (3.4 mS/cm).

The RED unit was rinsed with the artificial solutions and conditioned overnight before starting the testing. In order to investigate the influence of the diluate on process performance, the power measurements were carried out changing the diluate

feed flow rate (8 – 12 l/min) and conductivity (1.2 – 5.9 mS/cm). Conversely, constant conditions were kept for the concentrate, i.e. using artificial brine (215 mS/cm) at 8 l/min flow rate for all tests. The effect of diluate conditions on OCV and stack resistance is reported in Figure 7.6.

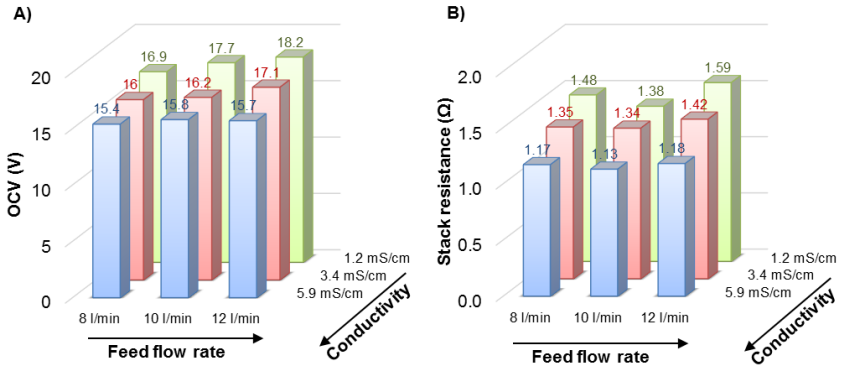

Figure 7.6. Influence of diluate conditions on OCV (A) and stack resistance (B). Power measurements performed feeding the prototype with artificial brine (NaCl solution at 215 mS/cm and 8 lt/min) and artificial brackish water (NaCl solution at 1.2 – 5.9 mS/cm).

Increasing the diluate conductivity, a reduction in OCV is observed due to the lower driving force available for the process (Figure 7.6.A). An increase of diluate flow rate leads to an increase of OCV, though the dependence is so weak to be in the same order of the experimental error. However, such expected effect is due to a lower residence time for diluate, thus a negligible reduction of driving force from inlet to outlet. On the other hand, the effect of diluate conditions are opposite for stack resistance (Figure 7.6.B), where the most favourable conditions within the investigated range are given by high diluate conductivity and low flow rate.

Based on these results, a counter-acting effect of diluate conditions on OCV and stack resistance can be identified. Such influence is reflected in the power output (Figure 7.7), where a scattering of measured power around an average value of 50 W has been observed. It is worth noting that the system was able to give stable performance in a wide range of operating conditions.

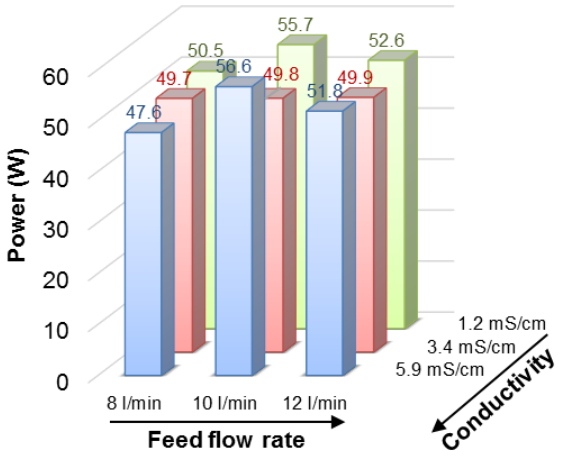

Figure 7.7. Influence of diluate conditions on power output. Power measurements performed feeding the prototype with artificial brine (NaCl solution at 215 mS/cm and 8 lt/min) and artificial brackish water (NaCl solution at 1.2 – 5.9 mS/cm).

From the experimental results show in Figure 7.7, it is not possible to identify optimal conditions for diluate flow rate and conductivity. On the other hand, similar conditions were previously modelled for a 20x20 cm^2 stack (par. 4.6.2): in that case, model predictions show that the maximum power density is obtained for a diluate concentration between 0.05 and 0.12 M NaCl, with flow velocity between 2 and 2.5 cm/s (Figure 4.13.A).

The scattering in power output experimentally observed (Figure 7.7) is in agreement with the model predictions, as the counter-acting effect of diluate flow rate/concentration on OCV and stack resistance leads to such variation, even for a slight change in the operating conditions.

Test with pure NaCl solutions

The measurements performed with artificial solutions showed that an average increasing power production of 30 – 40% was reached with respect to the natural solutions case. However, the salt from saltworks contains small amounts of other ions rather than Na^+ and Cl^- (K^+, Mg^{2+}, SO_4^{2-}), which may still have a relevant impact on

performance. For this reason, the RED unit was also tested with artificial solutions prepared with 99.5% pure sodium chloride (SOSALT S.p.A., Italy). The power measurements were performed changing the conductivity of diluate, ranging from 0.6 up to 5 mS/cm, while the conductivity of the artificial brine was kept close to the saturation point (206 mS/cm). Results are shown in Figure 7.8, where the relevant electric variable (stack voltage, resistance, power and power density) are reported as a function of the conductivity of feed dilute solution.

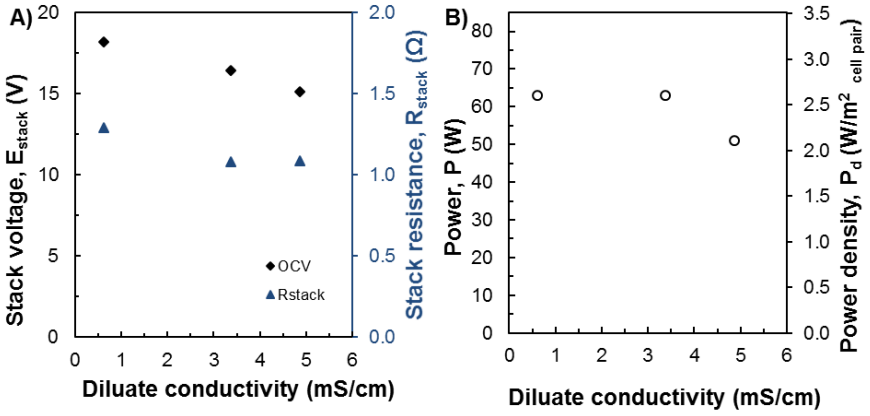

Figure 7.8. Influence of conductivity of diluate on process performance. A) Stack voltage and resistance. B) Power and power density. Power measurements performed feeding the prototype with artificial solutions prepared with 99.5% NaCl. Brine conductivity: 206 mS/cm. Feed flow rate: 8 l/min.

As previously shown in Figure 7.6, a decrease of both stack resistance and OCV is observed when increasing the diluate conductivity (Figure 7.8.A). As a consequence, a rather constant power output was reached when using 0.6 and 3.4 mS/cm NaCl solutions, while a reduced power was measured at 5 mS/cm (Figure 7.8.B). In a similar test, the diluate flow rate was increased up to 16 l/min (i.e. 2 cm/s flow velocity), thus achieving a power output of 66.3 W (2.7 W/m^2 of cell pair): this represents the highest value registered for the small RED prototype, as will be shown in Figure 7.10.

The direct comparison of stack performance with natural and artificial solutions is shown in Figure 7.9, where both diluate and concentrate were fed to the stack at 8 l/min flow rate in all the tests.

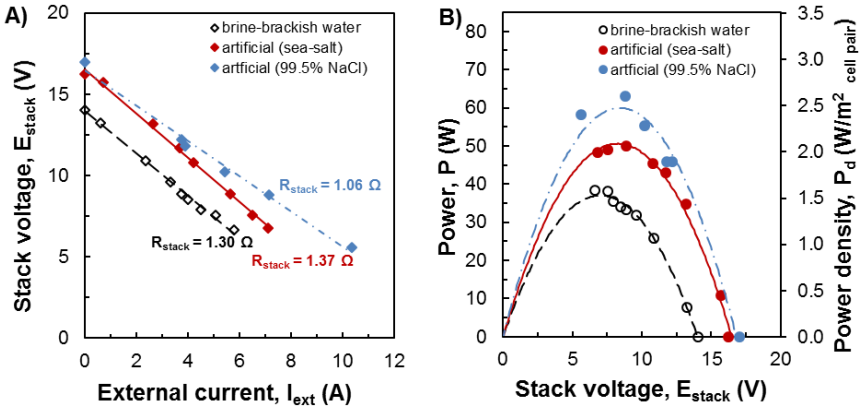

Figure 7.9. Power measurements performed with the small prototype (44x44 cm^2, 125 cell pairs) using real solutions (brackish water - brine) and artificial solutions. A) Polarization curve. B) Power and power density curve. Brine conductivity: 196 ± 11 mS/cm. Brackish water conductivity: 3.4 ± 0.1 mS/cm. Feed flow rates: 8 l/min (~1 cm/s fluid flow velocity).

The use of real solutions leads to a 13% reduction in the OCV with respect to the case of artificial solutions with sea-salt (Figure 7.9.A). The main difference between such tests is the higher content of NaCl in the sea-salt, whereas other ions (e.g. K^+, Ca^{2+}, Mg^{2+}, SO_4^{2-}) are present in the real brine. As a result, a lower OCV is reached with real solutions, while the overall stack resistance remains practically constant in both cases (Figure 7.9.A). Conversely, a lower stack resistance is registered when using 99.5% NaCl solutions: this is likely due to the high purity of the salt, which enhances the performance of membranes, reducing their actual resistance. Therefore, a power output of 63 W was achieved, thus reaching a further 30% increase with respect to the case with sea-salt (Figure 7.9.B).

7.4 Long-term performance of the small prototype

During the experimental campaign carried out with the small prototype, a significant amount of data was collected from May 2014 to September 2014, feeding the system with real brine and brackish water, and then with artificial solutions prepared with sea-salt or pure NaCl. The overall performance of the small prototype over five months of operation is shown in Figure 7.10, where both power output and power density are reported for the most relevant tests carried out during the experimental campaign.

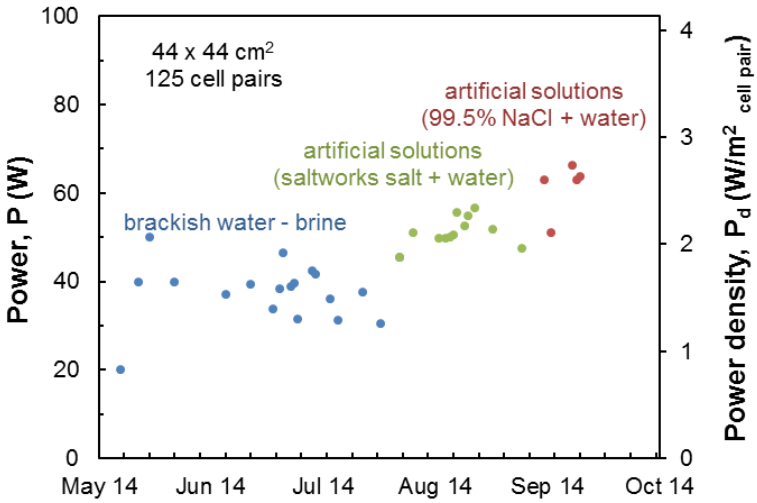

Figure 7.10. Overall performance of the prototype over five months of operation. Range of variable conditions: brine conductivity: 137 - 230 mS/cm, dilute conductivity: 0.7 - 7 mS/cm, temperature: 25-30°C, flow rates: 8 – 16 l/min.

In most cases, the experimental points reported in Figure 7.10 are obtained as a mean of 3 different measurements. The reproducibility of the experiments was good, as ±5% discrepancy was normally encountered in reproducibility tests. The scattering shown in Figure 7.10 is mainly due to the different experimental conditions investigated (e.g. changing flow rate or conductivity, as reported in the caption itself) caused by the variable conditions of real brine (temperature and conductivity) during the period or by operating choices of the experimental campaign when adopting

artificial solutions. Some of the variables monitored during the performed tests are reported in detail in Figure 7.11.

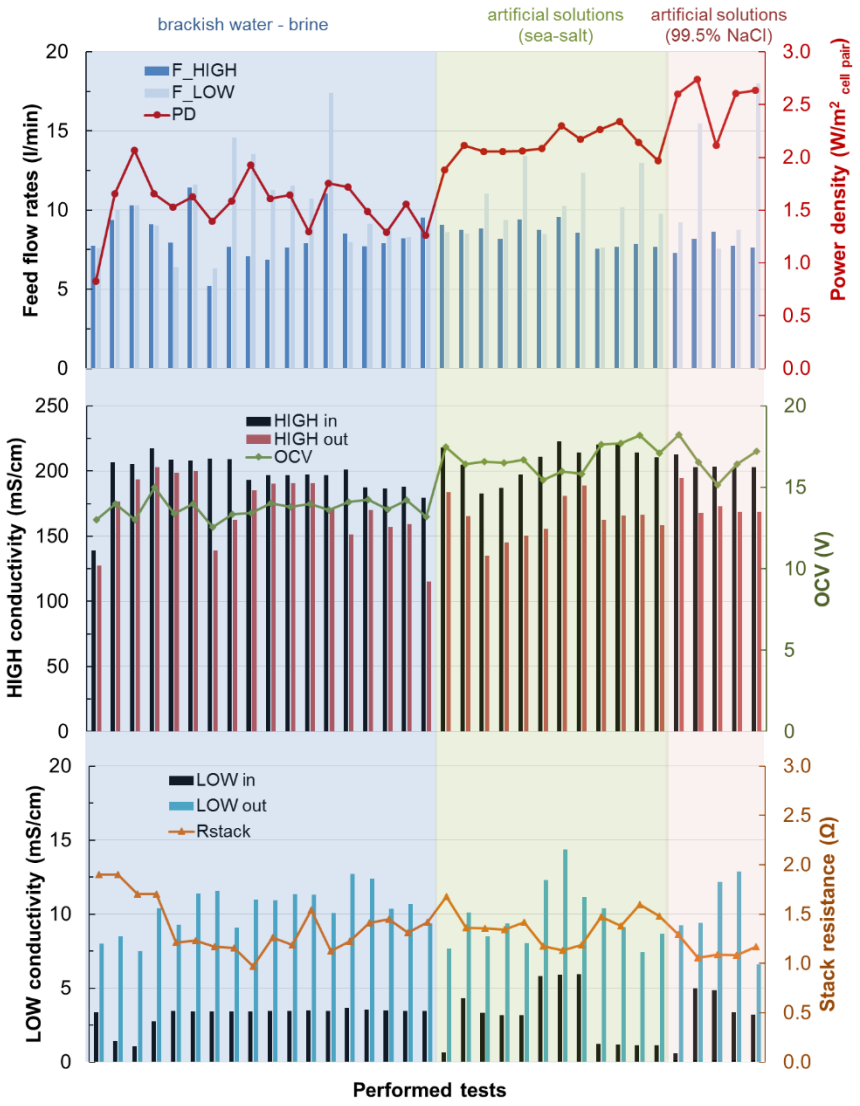

Figure 7.11. Overview of the performed tests with the small prototype (44x44 cm^2, 125 cell pairs) over five months of operation. Range of variable conditions: brine conductivity: 137 - 230 mS/cm, dilute conductivity: 0.7 - 7 mS/cm, temperature: 25-30°C, flow rates: 8 – 16 l/min.

It is worth noting how the system was able to work in a wide range of operating conditions, showing stable performance over the entire period of testing. The average power achieved with real brine and brackish water in typical conditions was 35 W (i.e. 1.4 W/m^2 cell pair), while using artificial solutions the power output increased up to 66 W (2.7 W/m^2 of cell pair).

7.5 Power measurements with large prototypes

After the installation of the large prototypes, the construction of a new electric circuit was necessary to fit the required range of external resistance for the larger stacks. Ten halogen lamps (100 W each) installed in parallel/series as shown in the electrical scheme (Figure 7.12) were used as variable-resistance load. The two large stacks were electrically connected in parallel: this allowed to double the total measured current without increasing the total voltage even when the two stacks were operated at the same time.

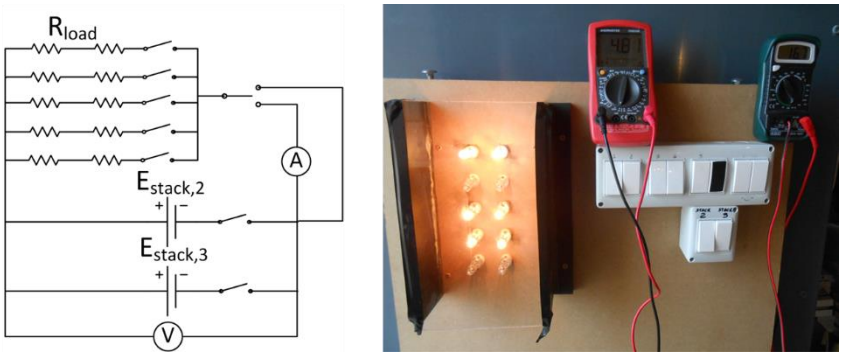

Figure 7.12. Schematic representation and picture of the external circuit used for power measurements with the large prototypes. Ten halogen lamps (each one with 100 W nominal power at 12V) were used as external load.

Following the procedure adopted for the small prototype, both large stacks were tested using artificial solutions. In particular, different conditions of conductivity and flow rates were investigated for dilute. As an example, Figure 7.13 shows the effect

of diluate conductivity on the performance of both large prototypes, both in terms of power output and power density.

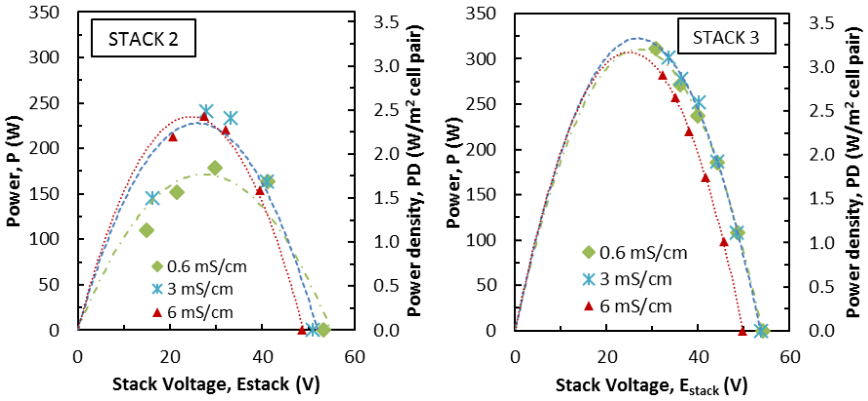

Figure 7.13. Influence of diluate conductivity on process performance. Power measurements performed with large prototypes fed with artificial brine (215 mS/cm) and artificial brackish water. Concentrate flow rate: 26 l/min. Diluate flow rate: 34 l/min.

It is worth noting that stack 3 always shows better performance than stack 2: this difference can be attributed to improvement in stack making, which reduces the internal leakages and pressure drop in the electrode compartments. In particular, stack 2 showed a slight change in the stack resistance during some tests (e.g. in the test at 0.6 mS/cm, Figure 7.13.A), likely due to variation in the behaviour of the electrode rinse solution [20].

The performance of the system does not change appreciably in the range of 3 – 6 mS/cm of diluate conductivity (i.e. 0.03 – 0.06 M NaCl). In this case, a power output of more than 320 W (3.3 W/m^2 cell pair) was reached, which was the highest value achieved with a single RED unit.

Both large prototypes were also tested together, with a parallel feed for solutions (Figure 7.14). Although other plant configuration were originally investigated during the modelling activities (as described in par. 4.8), a serial arrangement for the stacks was not taken into account. In fact, feeding the two units in series would lead to high hydraulic pressures inside the first unit (> 1 barg), increasing significantly the risk of internal leakage.

Feeding both units in parallel, internal resistance of 3.4 Ω and 2.8 Ω were estimated for stack 2 and stack 3, respectively (from slopes of the curves in Figure 7.14.A). Using both large prototypes, the maximum power output obtained with real brine and brackish water was 265 W (1.4 W/m^2 cell pair).

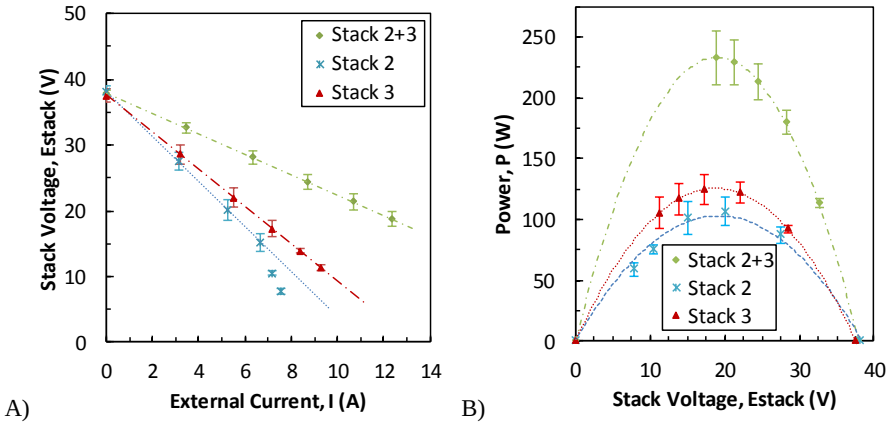

Figure 7.14. Power measurements with two large prototypes (44x44 cm^2, 500 cell pairs) using brine and brackish water. All measurements were performed with parallel feed for stacks. Brine conditions: conductivity 194 mS/cm, T = 28°C, flow rate 26 l/min. Brackish water conditions: conductivity 3.4 mS/cm, T = 25°C, flow rate 38 l/min. Error bars show standard deviation of all tests performed. A) Polarization curve. B) Power curve.

As previously shown in Figure 7.13, stack 3 showed better performance than stack 2 in all measurements. The different performance is especially clear in the high-current range, when a deviation of the polarisation curve from the linear behaviour was observed only for stack 2 (Figure 7.14.A). This phenomenon is generally caused by change in the properties (composition or flow rate) of the ERS solution, which affects the overall stack resistance. However, the same solution was used for both stacks, and no problem was encountered for stack 3. Therefore, any influence of the composition of the electrode rinse solution can be excluded. As a consequence, the change in the resistance for stack 2 may be due to mass transport phenomena in the electrode compartments. In fact, higher pressure drops were registered for stack 2 than for stack 3: this might be due to different geometry of the electrode compartments, though no information was provided by the stack manufacturer with this regard.

It is worth noting that the two large units were fed in parallel with flow rates lower than standard conditions (26 l/min and 38 l/min for brine and brackish water, respectively). Such flow rates correspond to fluid velocity in the range of 0.4 – 0.6 cm/s, causing the decline in performance with respect to the test performed in standard conditions. On the other hand, tests with larger flow rates were not possible due to physical limitations in the installed feed pumps.

Aside from testing the system with natural and artificial solutions, a hybrid situation was also investigated, i.e. using real brine as concentrate and tap water (0.7 mS/cm) as diluate. This condition provides further information regarding the effect of brackish water on stack performance. An overall summary of the tests performed with stack 2 is reported in Table 7.1. For each feed conditions, three different flow rates were investigated. Moreover, for the case of artificial solutions, three different diluate conductivity were also taken into account.

The use of tap water (0.7 mS/cm) as diluate allows to reach higher OCV values with respect to the brine – brackish water case. On the other hand, the lower conductivity of dilute causes an increase of the stack resistance. Because of these counter-acting effects, similar power output was obtained under brine – brackish water and brine – tap water conditions.

The same experimental campaign was later repeated on stack 3, and the relevant results are reported in Table 7.2. In this way, a fast comparison is possible between the two large prototypes.

Table 7.1. Summary of the main results achieved with stack 2.

Feed solutions	**LOW flow rate (l/min)**	**LOW conductivity (mS/cm)**	**OCV (V)**	**P (W)**	**P_d (W/m^2)**
brine - brackish water	36	3.4	41.7	123	1.3
	32	3.4	41.0	112	1.2
	16	3.4	38.9	125	1.3
brine - tap water	36	0.7	47.5	124	1.3
	32	0.7	44.3	122	1.3
	16	0.7	41.2	115	1.2
NaCl solutions	34	6.5	49.0	245	2.5
		3.5	51.2	257	2.7
		0.7	53.6	218	2.3
	32	6.5	48.3	240	2.5
		3.5	50.2	246	2.5
		0.7	52.4	186	1.9
	16	6.5	42.2	173	1.8
		3.5	47.0	186	1.9
		0.7	46.8	136	1.4

Table 7.2. Summary of the main results achieved with stack 3.

Feed solutions	LOW flow rate (l/min)	LOW conductivity (mS/cm)	OCV (V)	P (W)	P_d (W/m^2)
brine - brackish water	36	3.4	44.1	163	1.7
	32	3.4	43.4	148	1.5
	16	3.4	39.6	121	1.2
brine - tap water	36	0.7	49.6	203	2.1
	32	0.7	46.6	162	1.7
	16	0.7	42.4	144	1.5
NaCl solutions	34	6.5	49.5	265	2.7
		3.5	54.0	323	3.3
		0.7	55.4	287	3.0
	32	6.5	49.8	322	3.3
		3.5	53.4	323	3.3
		0.7	54.6	323	3.3
	16	6.5	42.9	202	2.1
		3.5	44.4	205	2.1
		0.7	48.3	237	2.4

Stack 3 showed always better performance than stack 2 under the same operating conditions. In particular, lower pressure drops were observed in the electrode compartments, which may indicate better fluid dynamic conditions for the ERS solution.

Table 7.3 shows an overview of the measurements carried out feeding stack 2 and stack 3 in parallel. The stacks were electrically connected in parallel, thus the OCV reported in Table 7.3 is the arithmetic average of OCV of single units.

Table 7.3. Summary of the main results achieved feeding both stacks in parallel.

Feed solutions	**LOW flow rate (l/min)**	**LOW conductivity (mS/cm)**	**OCV (V)**	**P (W)**	**P_d (W/m^2)**
brine - brackish water	19	3.4	38.4	256	1.3
	16	3.4	35.3	190	1.0
brine - tap water	19	0.7	41.2	266	1.4

From Table 7.3, it is evident how the power produced by the two stacks in parallel is practically the sum of the outputs of the two stacks (Table 7.1-Table 7.2). Therefore, the total nominal power capacity of the plant can be derived from the sum of the three stacks.

An overall comparison of all the tested RED prototypes can be given in terms of power density (Figure 7.15). Regarding the process scale-up, the comparison between stack 1 and stack 2 show that increasing the number of cell pairs from 125 up to 500 did not led to a reduction of performance. The third stack showed improved performance with respect to stack 2, especially due to reduced pressure drop in the electrode compartments and a likely reduction of internal leakages.

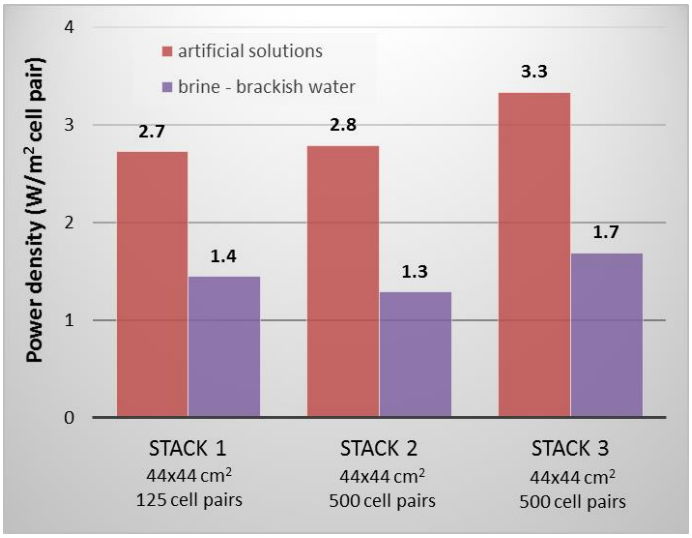

Figure 7.15. Performance of the RED prototypes tested in terms of power density (W/m^2 of cell pair). Tests performed using brine (200-220 mS/cm) – brackish water (3.4 mS/cm) and artificial solutions (NaCl solutions with same conductivity as natural solutions).

The overall capacity of the RED units installed in Marsala is shown in Figure 7.16. Using artificial solutions with the same conductivity of brine – brackish water, the REAPower plant showed a global capacity of almost 700 W. Moreover, using real brine and brackish water, the global capacity is nearly 330 W.

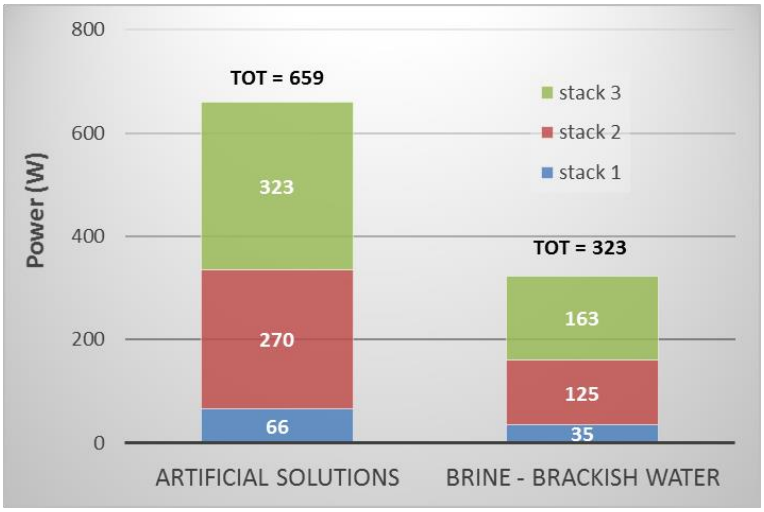

Figure 7.16. Overall plant capacity of the REAPower demonstration plant. Tests performed using brine (200-220 mS/cm) – brackish water (3.4 mS/cm) and artificial solutions (NaCl solutions with same conductivity as natural solutions).

It is worth noting that the simulations previously presented (par. 4.8) were based on the use of 3 RED units, each one with a 44x44 cm^2 membrane area and 500 cell pairs. With such RED plant, a target capacity of 1 kW is predicted by the process simulator. Although only two RED units of such size have been finally installed in the REAPower pilot plant, it is clear from Figure 7.16 that the installation of a third unit of the same size would allow to reach the target capacity of 1 kW with artificial solutions. On the other hand, a serial arrangement among RED stacks is not practical, due to the relatively high pressure drop arising within the compartments, which would lead to very low net power output.

7.6 Outlook and final remarks

In this chapter, the main achievements of the experimental campaign performed on the REAPower demonstration plant has been presented. The pilot plant, which is located in a saltworks area in Marsala (Trapani, Italy), has been tested for six months using both natural and artificial solutions.

Based on the previous modelling works and on the quality of the available feed waters, brackish water (equivalent to 0.03 M NaCl) was selected instead of seawater as dilute solution for all the tests, while saturated brine (~5 M NaCl) was adopted as concentrate. A RED prototype with 44x44 cm^2 membrane area equipped with 125 cell pairs has been tested for three months using such natural solutions, reaching an average power output of 35 W (i.e. 1.4 $W/m^2_{cell\ pair}$). Therefore, the same RED unit was tested with artificial solutions prepared with sea-salt and pure NaCl (99.5%), showing that the use of real brackish water and brine caused a reduction of process performance in the range of 40-50%. Such reduction is likely due to the presence of relevant amount of other ions, especially Mg^{2+}, in the real brine. With this regard, a pre-treatment stage for Mg^{2+} removal should be taken into account for further scaling-up and operation of RED plants. Overall, the first RED prototype was tested for five months, operating in a wide range of operating conditions without showing any significant performance loss nor fouling issue.

The plant was scaled up through the installation of two larger RED units, having the same membrane area and equipped with 500 cell pairs each. The increasing number of cell pairs did not lead to a reduction of performance with respect to the first unit. In particular, the third RED unit showed better performance than the second stack, likely due to improvement in stack making and reduction of internal leakages. Moreover, lower pressure drops were registered in the electrode compartments: this is especially important for reducing the risk of limiting current phenomenon.

With a plant capacity of almost 700 W using artificial NaCl solutions, and 330 W with real brine and brackish water, the REAPower plant is by far the largest application worldwide of the reverse electrodialysis technology, and clearly gives a truly demonstration of the feasible scaling-up of the process.

8 FUTURE PERSPECTIVES: REVERSE ELECTRODIALYSIS FOR WASTE HEAT RECOVERY[*†]

Abstract

Reverse electrodialysis has been widely addressed as a reliable technology to produce energy from natural salinity gradients. In a broader context, RED can be a new system to convert low-temperature heat (e.g. recovering waste heat from industrial plants) into electricity.

This chapter investigates the concept of "RED heat engine", i.e. a system aiming to convert heat into electricity by reverse electrodialysis. Synthetic solutions can be used for creating artificial salinity gradients and produce energy. The discharged solutions from RED system are sent to a thermally-driven separation unit, in order to restore the salinity gradient. Using very low-grade heat (e.g. industrial waste heat) as thermal energy source, the whole process can be economically sustainable.

The use of synthetic solutions in a closed-loop system allows also to overcome some drawbacks of natural streams, such as the need of extensive pre-treatment strategies to prevent fouling. Moreover, a variety of salts and solvents can be explored for optimising the RED performance. A new model has been developed for this purpose, in order to analyse the power production of a RED unit using non-conventional salts and identify possible alternatives to sodium chloride.

Compared with competitive technologies for waste heat recovery, RED heat engine can be a viable process for recovering very low temperature heat in the near future.

[*] Part of this chapter has been revised for publication as:

- M. Tedesco, A. Cipollina, A. Tamburini, W. van Baak, G. Micale, *Investigation of the most suitable salts for Power Production by Reverse Electrodialysis*, in preparation.

[†] The research activity presented in this chapter has been used for the project proposal *RED-Heat-to-Power*, successfully submitted for Horizon 2020 (Proposal Number: SEP-210184404; Call: H2020-LCE-2014-1).

8.1 Introduction

Reverse Electrodialysis has been broadly studied as a viable technology for the conversion of salinity gradient energy into electricity. Up to now, RED technology has been mainly focused on the exploitations of salinity gradients from natural streams, e.g. river water, seawater or brine. This allows to harvest an extremely high potential especially in coastal regions, where solutions with different salinity are available in large amount. However, the utilization of natural streams for RED process presents some remarkable drawbacks:

- Need for energy intensive pre-treatment processes to prevent fouling/biofouling phenomena [51,52].
- Geographic constraints for plant location (i.e. availability of both dilute and concentrated solutions in the same area).
- Large amount of both solutions required; in fact, the availability of diluate or concentrate can be often the limiting factor for the process scale-up [39,91].

Furthermore, a strong caution should be always exercised regarding the impact of discharged streams into the environment.

These drawbacks may be overcome operating the RED process in a closed-loop, i.e. in a stand-alone system where synthetic solutions are used as working fluids. The outlet streams from the RED process can be regenerated through a proper thermally-driven separation process, and eventually recycled back to the RED unit.

The concept of "closed-loop RED" system presents another notable advantage: using artificial solutions instead of natural streams, new kind of salt and solvent could be taken into account. Therefore, suitable solutions can be purposely adopted in order to enhance the performance of the RED process. For instance, very highly soluble salts can be used, reaching considerably high driving force for RED process. On the other hand, the selection of salt/solvent may be based on the energy costs for the regeneration stage, thus optimising the overall efficiency of the closed-loop system.

The whole process can be economically viable if a cheap source of thermal energy is available for the regeneration stage. With this regard, RED technology can be seen as an interesting alternative for recovering industrial waste heat at low temperature and produce electric energy [1,45]. Therefore, it can be considered as a "RED heat

engine", i.e. a system to convert low-grade heat into electricity by means of a reverse electrodialysis stage (Figure 8.1).

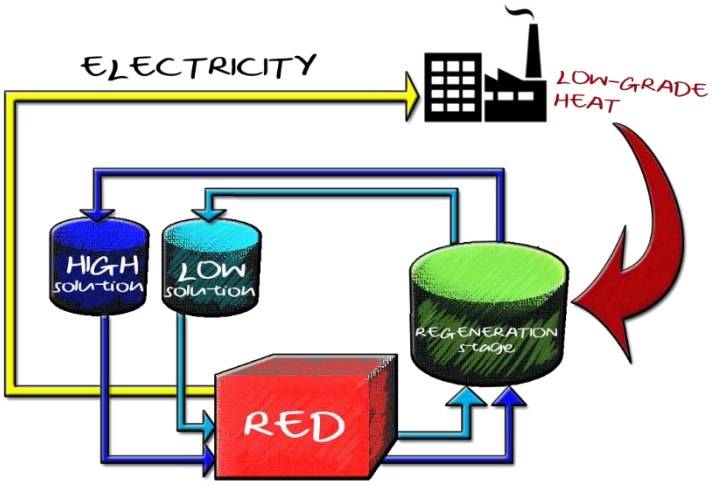

Figure 8.1. Principle of RED heat engine.

Although the concept of RED heat engine has been already presented in the literature [1,45,93], an in-depth investigation is still required to explore the potential of this technology. Luo et al. 2012 [90] proposed the principle of "thermally-driven electrochemical generator" (TDEG), i.e. a system where a RED stack is coupled with a distillation column as thermal separation unit, using aqueous solutions of ammonium bicarbonate (NH_4HCO_3) as working fluids [93].

The selection of ammonium bicarbonate is related to its thermolytic properties: this salt decomposes below its melting point, dissociating into ammonia, carbon dioxide and water when heated at temperature above 36°C [94]. As a result, ammonium bicarbonate solutions can be ideally regenerated at very low temperature (~50°C). In a closed-loop RED system, the use of ammonium bicarbonate could be an interesting option to reduce regeneration costs and achieve interesting efficiencies. On the other hand, NH_4HCO_3 has a rather poor solubility in water (2.7 mol/l at 25°C [95]), which limits the salinity difference for the RED process. With this regard, a

maximum power density of 0.33 W/m^2 of membrane was reached by Luo et al. using 0.02 M NH_4HCO_3 and 1.5 M NH_4HCO_3 solutions as diluate and concentrate, respectively [93].

For its peculiar thermolytic properties, NH_4HCO_3 has been investigated also in other novel applications for power production, namely microbial RED cells [96,97] and osmotic heat engine [98,99].

In a microbial RED system, a small RED stack is placed directly in contact with a microbial fuel cell (MFC), i.e. a biochemical reactor where exoelectrogenic bacteria are used to oxidize soluble organic matter, thus releasing electrons on an electrode surface [100]. In fact, the bacterial oxidation may provide a valuable anodic reaction for RED process. Therefore, coupling RED process with MFC, electric energy can be produced from wastewater and salinity gradients. Using solutions with conductivity typical of domestic wastewater (1 mS/cm), a power density ranging from 0.26 to 0.45 W/m^2 of projected cathode area (i.e. 0.025-0.045 W/m^2 of membrane) has been reported in an air-cathode MFC [96].

The osmotic heat engine (OHE), also known as "closed-loop PRO", has a concept similar to the RED heat engine, where a pressure retarded osmosis (PRO) unit is coupled with a distillation unit as regeneration stage. Such concept was firstly proposed in 1975 by Loeb [101], while a more detailed investigation has been recently presented by McGinnis [98,99]. In particular, the osmotic heat engine proposed by McGinnis is based on the use of an ammonium bicarbonate draw solution. A maximum thermal efficiency of 16% of the Carnot efficiency (i.e. an actual energy conversion efficiency of 1.2%) has been predicted for a OHE that use waste heat at 50°C temperature [99].

Both RED heat engine and osmotic heat engine can be seen, more generally, as salinity gradient power (SGP) engines, i.e. stand-alone systems where salinity gradients are exploited to convert waste heat into electricity. This concept has been recently presented as Heat-to-Current Converter (HTTC) by Marino et al. [102]. In particular, the main idea of the HTTC system is to use an electrochemical cell as salinity gradient converter, coupled with a distiller for the regeneration stage. Marino et al. reported a thermodynamic study for demonstrating the feasibility of the closed-

loop process for producing electricity from waste heat, showing that in reversible conditions the energy efficiency of the system is very close to the efficiency of the Carnot cycle operating in the same temperature range [102]. However, the authors do not provide specific indications about the technology adopted for the electrochemical cell (i.e. either reverse electrodialysis or capacitive mixing process [6,7]), nor for the distillation stage.

Focus of this chapter is to address the feasibility of RED heat engine (or "closed-loop RED") as viable technology to recover waste heat via electricity production. The study was focused both on the RED and on the regeneration stages. Regarding the RED stage, a model has been purposely developed to investigate the potential application of different salt solutions. Therefore, a sensitivity analysis has been performed with respect to the main operating parameters, in order to show the optimal concentration range for a number of possible salts. For the regeneration stage, both conventional and innovative separation processes were analysed as possible alternatives. The achievements of this study indicate promising directions for the development of the technology, in order to lead further R&D efforts towards the construction of the first demonstration prototype.

8.2 State-of-the-art of waste heat recovery technologies

Over ninety percent of the primary energy utilization in the world passes through a thermal separation stage to produce electricity [103]. During such processes, a significant amount of energy is discharged as "waste heat" via exhaust streams, condensers, gas coolers, or other heat transfer equipment. Aside from large industrial users, manufacturing processes and vehicle combustion engines are also responsible for a substantial release of waste heat at useful temperature [104], as well as biogas and biomass plants, cargo shipping, and decentralised diesel power plants.

The amount of energy that is ultimately lost is remarkably high, especially in the case of the most developed countries. Although published data on waste heat release are often limited or unavailable, it has been estimated that over two-third of the world primary energy supply for electricity production is rejected as waste heat, mainly from

thermo-mechanical energy conversion losses (Figure 8.2). Therefore, recovery of waste heat can be a practical strategy for decreasing the demand of high-grade energy and reducing greenhouse gas emissions, thus improving energy efficiency worldwide. Moreover, industrial waste heat represents in fact a burden for companies, causing disposal costs to prevent environmental issues.

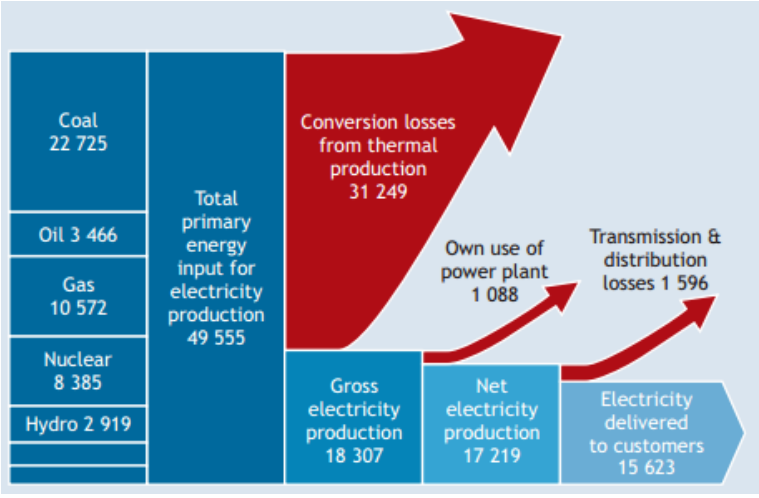

Figure 8.2. Energy flows in the global electricity system (TWh) [105].

Waste heat from industrial applications is discharged in a very wide range of temperature, which affects the potential recovery strategies. A generally accepted classification of waste heat based on temperature is rather difficult to identify. Nevertheless, three different levels of waste heat may be recognised:

- *High Temperature waste heat* (> 650°C), essentially related to hot flue gases from industrial furnaces (Table 8.2).
- *Medium Temperature waste heat* (230-650°C), mainly due to exhausted streams e.g. from boilers, heaters and ovens (Table 8.2).
- *Low Temperature waste heat* (< 230°C), from exhausted gases and cooling water streams in a variety of industrial processes (Table 8.3).

It is worth noting that a large part of waste heat is available at low-temperature range. As an example, industrial waste heat in the USA is estimated to be 833 TWh specifically for temperatures between 50° and 100°C [104]. Nevertheless, recovery of waste heat has been essentially limited to high and medium temperature ranges, while very few technologies are feasible to recover low-T waste heat. In fact, recovery waste heat at low temperature presents additional challenges to overcome: for instance, when the temperature of exhaust gases is below 120-150°C, water condensation on heat exchanger surfaces may occur, thus creating favourable conditions for fouling and deposition of corrosive substances. Moreover, the current state of the art of proposed technologies indicates that still very few processes can operate with heat sources below 100°C and with a sufficient efficiency for being economically feasible.

The primary approach to recover waste heat is based on the concept of "thermal cascading", i.e. the use of thermal energy for different applications, according to the required temperature range. For instance, waste heat from flue gases is commonly used to preheat combustion air through recuperative heat exchangers; exhaust streams can be used to preheat water and reactor loads, etc. Recovery waste heat by thermal cascading can remarkably improve the overall efficiency of the current energy system: in fact, nowadays 12.5% of primary fuel and 20.3% of electricity are still used for space heating, water heating and refrigeration, which are applications where low-grade heat can be sufficient [104].

Aside from thermal cascading, waste heat can also be converted into a more exploitable energy form, such as high-quality thermal energy, mechanical work or electric energy. As an example, low-grade heat (T ~100°C) can be recovered by increasing its temperature (up to ~150°C) through absorption heat transformers (AHTs): in this way, typically 50% of the waste heat can be "upgraded" to high-quality thermal energy, while the not-recovered amount of waste heat is discharged to a low-temperature sink [106].

Other technologies are able to use waste heat to generate power via mechanical work or electricity. A summary of the current technologies for waste heat recovery is reported in Table 8.3.

The traditional technologies proposed to recover waste heat by power generation are based on the production of mechanical energy, then electricity through a turbine, such as steam Rankine cycles and organic Rankine cycles. More recently, a number of novel technologies have been presented to obtain directly electric energy.

Table 8.1. Classification of high-temperature and medium-temperature waste heat. Adapted from [107].

Temp Range	Sources	Temp (°C)	Advantages	Disadvantages/ Barriers	Typical Recovery Methods/ Technologies
High > 650°C	Nickel refining furnace	1370-1650	High-quality energy, available for a diverse range of end-uses with varying temperature requirements High-efficiency power generation High heat transfer rate per unit area	High temperature creates increased thermal stresses on heat exchange materials Increased chemical activity/corrosion	Combustion air preheat Steam generation for process heating or for mechanical/ electrical work Furnace load preheating Transfer to med-low temperature processes
	Steel electric arc furnace	1370-1650			
	Basic oxygen furnace	1200			
	Aluminum reverberatory furnace	1100-1200			
	Copper refining furnace	760-820			
	Steel heating furnace	930-1040			
	Copper reverberatory furnace	900-1090			
	Hydrogen plants	650-980			
	Fume incinerators	650-1430			
	Glass melting furnace	1300-1540			
	Coke oven	650-1000			
	Iron cupola	820-980			
Medium 230-650°C	Steam boiler exhaust	230-480	More compatible with heat exchanger materials Practical for power generation		Combustion air preheat Steam/ power generation Furnace load preheating, feedwater preheating Transfer to low-T processes
	Gas turbine exhaust	370-540			
	Reciprocating engine exhaust	320-590			
	Heat treating furnace	430-650			
	Drying & baking ovens	230-590			

Table 8.2. Classification of low-temperature waste heat. Adapted from [107].

Temp Range	Sources	Temp (°C)	Advantages	Disadvantages/ Barriers	Typical Recovery Methods/ Technologies
Low <230°C	Exhaust gases exiting recovery devices in gas-fired boilers, ethylene furnaces, etc.	70-230	Large quantities of low-temperature heat contained in numerous product streams.	Few end uses for low temperature heat Low-efficiency power generation For combustion exhausts, low-T heat recovery is impractical due to acidic condensation and heat exchanger corrosion	Space heating Domestic water heating Upgrading via a heat pump to increase temp for end use Organic Rankine cycle
	Process steam condensate	50-90			
	Cooling water from: furnace doors	30-50			
	annealing furnaces	70-230			
	air compressors	30-50			
	internal combustion engines	70-120			
	air conditioning and refrigeration condensers	30-40			
	Drying, baking, and curing ovens	90-230			
	Hot processed liquids/solids	30-230			

Table 8.3. Current technologies to recover heat via power generation. Adapted from [107].

Technology	**Temperature range**	**Typical sources of waste heat**	**Capital cost ($/kW)**
Steam Rankine Cycle	M, H	Exhaust from gas turbines, reciprocating engines, incinerators, and furnaces.	1100-1,400
Kalina Cycle	L, M	Gas turbine exhaust, boiler exhaust, cement kilns	1100-1,500
Organic Rankine Cycle	L, M	Gas turbine exhaust, boiler exhaust, heated water, cement kilns	1,5003,500
Thermoelectric Generation	M, H	Not yet demonstrated in industrial applications	20,000-30,0000
Piezoelectric generation	L	Not yet demonstrated in industrial applications	10,000,000
Thermal Photovoltaic	M, H	Not yet demonstrated in industrial applications	N/A
Osmotic Heat Engine	L	Not yet demonstrated in industrial applications	N/A

Recovering waste heat via power generation is affected by a thermodynamic limit of efficiency achievable. In fact, the highest efficiency that can be reached by the heat engine is equal to the efficiency of a Carnot cycle (η_c) operating between the same temperatures of the hot source (T_h) and the cold sink (T_c):

$$\eta_c = 1 - \frac{T_c}{T_h} \tag{8.1}$$

Assuming the ambient temperature as cold sink for the process (T_c = 20°C), the Carnot efficiency is only function of the hot source temperature. As a result, using low-temperature waste heat (e.g. ~ 50-100°C), the Carnot efficiency is relatively low (η_c ~10-20%). The actual energy efficiency of the heat engine will be inevitably lower than the Carnot efficiency. As a consequence, most technologies that are industrially adopted for recovering medium/high temperature ranges are not suitable in the low temperature range, where higher efficiency may be required to make the recovery economically feasible.

Up to now, the only technologies industrially adopted for recovering low-T waste heat are organic Rankine cycles and Kalina cycle (Table 8.3). In addition, different applications have been recently proposed, although not yet demonstrated on industrial scale. Such technologies, being directly competitors of the proposed RED heat engine, will be described in more detail in the following paragraphs.

8.2.1 Rankine cycles

Rankine cycle systems represent the most adopted technology for recovering waste heat via power generation. These conventional and well-established processes are used in a wide range of temperature, from high temperature in combined heat and power (CHP) systems, to relatively low temperature (as low as 70-80°C).

In a Rankine cycle, waste heat is firstly converted into mechanical work, and ultimately into electricity using a turbine. The thermodynamic cycle is constituted by the following steps: 1) waste heat is used to generate vapour in a heat boiler. 2) The vapour is sent to drive a turbine, thus generating electricity. 3) The exhaust gas from the turbine is recovered in a vacuum condenser. 4) Finally, the condensate is pumped to elevate its pressure and sent to the hot boiler.

Based on the nature of the working fluid adopted, three different types of Rankine cycles can be identified: steam Rankine cycle (SRC), Organic Rankine cycles (ORCs), and Kalina cycle (where the working fluid is a binary mixture of ammonia and water). The physical properties of the working fluid strongly influences the operating conditions of the cycle, thus determining different ranges of applicability for the three types of Rankine cycles.

Steam Rankine cycle (SRC)

The steam Rankine cycle (SRC) is the earliest technology proposed to convert heat into power, using water as working fluid. The use of water makes a minimum allowable temperature for SRC applications: in fact, low-T waste heat may not provide enough energy to superheat the steam, thus causing steam condensation and

possible erosion of the turbine blades. In practical applications, SRC systems are not adopted when the temperature of the waste heat source is below 340-370°C.

Thanks to its simple and well-established technology, SRC is largely adopted in the industry for recovering hot gases in the medium-temperature range (370-550°C). SRC is also applied in combined heat and power (CHP) systems at high temperature range (> 650°C), where the Rankine cycle is directly fuelled by oil or coal.

Organic Rankine Cycle (ORC)

Organic Rankine cycle (ORC) is a thermodynamic cycle where an organic compound is used as working fluid instead of water. The organic working fluid is generally characterised by a lower boiling point and a higher molecular mass with respect to water: the low boiling point allowed to operate the cycle at lower temperature, while a high molecular mass gives higher mass flow, and therefore a compact design and higher turbine efficiency. Some example of common working fluids are silicon oil, propane, haloalkanes, iso-pentane, iso-butane, p-xylene, toluene. However, current research in the ORC technology is focusing on the selection of new working fluids [108].

ORC has been the first technology that has made technically and economically feasible the recovery of waste heat at temperature below 300°C. Thanks to the properties of the adopted working fluid, ORC is especially suitable for recovering waste heat in the low-medium temperature ranges (80-300°C).

Kalina Cycle (KC)

In the Kalina Cycle (KC) the working fluid adopted in the cycle is an ammonia-water mixture. The main advantage of using a binary mixture in a Rankine cycle is that the working fluid increases its temperature during evaporation (unlike pure substances). This leads to a better use of the waste heat, resulting in an increase of the efficiency by 15-25% with respect to ORC systems at the same temperature level. As a result, the Kalina cycle presents the highest efficiency among the Rankine cycles for waste heat recovery in the low temperature range. However, its complexity and high capital costs makes it economically feasible only in large power plants (~100 MW).

8.2.2 Direct electrical convertor devices

These recent developed technologies are based on the direct conversion of thermal energy into electricity. In this field, thermoelectric and piezoelectric may be promising options to recover waste heat in small-scale applications, e.g. from internal combustion engines. However, these technologies are currently affected by very low efficiency and high capital costs, and their application for recovering industrial waste heat has not been proven yet.

Thermoelectric Generator (TEG)

Thermoelectric Generator (TEG) devices are constituted by semiconductors able to convert a temperature difference into electric potential (Seebeck effect). Therefore, they can be seen as "solid-state heat engines" for the direct conversion of waste heat into electricity. Thanks to their simplicity and compactness, TEG devices could be a promising alternative to Rankine cycles, especially in small-scale applications. TEGs are currently adopted for the recovery of waste heat of internal combustion engines [109]. Alternatively, TEG devices has been also proposed as heat pumps, converting electrical power directly into cooling and heating (Peltier effect) [110].

Despite being a very promising technology, TEG is still affected by rather low energy efficiency. The reported efficiency for such devices is 2-3% when the temperature of waste heat source is 60-120°C, respectively [103]. These values are approximately one-third of the efficiency of ORC systems in the same temperature range. Current research efforts are focused on developing flexible, cost-effective devices with higher efficiency. In particular, organic thermoelectric materials are gaining interest in this field.

Piezoelectric Power Generators (PEPG)

Piezoelectric Power Generators (PEPG) are constituted by a piezoelectric thin-film membrane that generates electric potential when subjected to mechanical vibrations. Such mechanical vibrations on the PEPG device can be induced by a gas involved in an expansion/compression cycle fed by waste heat (150-200°C). However, PEPG devices are still characterised by rather low efficiency (~1%) and

strong technological challenges to overcome. For instance, new materials able to operate at high oscillatory frequencies (~1 KHz) are needed to increase substantially the process efficiency [105].

Carbon Carrier Cycle

This recently patented technology is based on a modification of the Rankine cycle, where the condenser is replaced by a carbon dioxide chemical absorption stage [111]. In this way, the working gas from the turbine is temporarily stored in liquid state, thus it can be easily pumped. Moreover, being the chemical absorption highly endothermic, the temperature of the gas exiting the turbine may be as low as −70° C. As a result, very high efficiency are declared by the authors of the patent, though no applications have been reported to date. Waste heat at temperature as low as 150°C can be theoretically exploited for such energy conversion device.

Based on the current state-of-the-art of the technologies to recover waste heat via power generation, it can be concluded that some conventional processes (i.e. organic Rankine cycle, Kalina cycle) allow to recover waste heat at temperature as low as 100°C with acceptable efficiency. In addition, some emerging technologies such as thermoelectric generators are gaining significant interest in small-scale applications.

However, when looking at low-temperature waste heat (<100°C), no technology has been proven to give high recovery efficiency. Therefore, there is still a notable amount of waste heat currently unexploited, which could be used as source of energy for the proposed RED heat engine.

8.3 RED heat engine: technological challenges and perspectives

The concept of RED heat engine is to generate electricity from salinity gradients using a Reverse Electrodialysis (RED) device in a closed-loop system. Using the working fluids in a closed-loop, only limited amounts of artificial saline solutions are required, which is a remarkable advantage with respect to conventional open loop RED. In order to restore the original salinity gradient, the solutions exiting from the

RED unit are then regenerated through a separation step that uses low-temperature heat as its energy source.

The system consists of two main stages (Figure 8.3): i) a thermal separation stage, which can be fed by heat from a low-grade external source; ii) a power generation stage, i.e. a reverse electrodialysis unit.

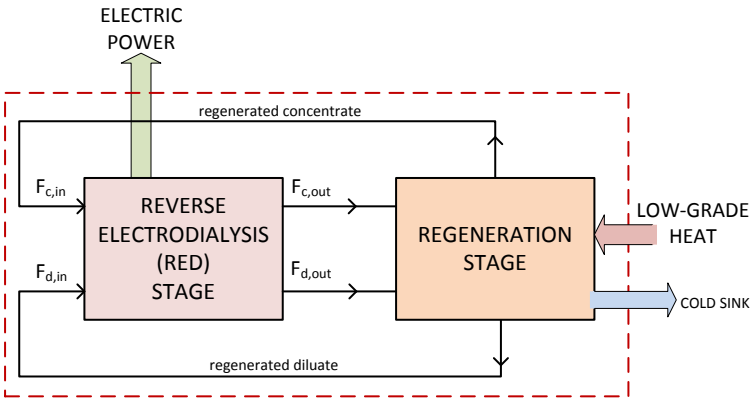

Figure 8.3. Simplified scheme of the RED heat engine.

Although the concept of closed-loop RED has been already presented in the recent literature [45,93], the real potential of such technology is still far from being explored in detail. With this regard, the use of artificial salinity gradient in a closed-loop allows to investigate a variety of non-conventional salt or solvent for the working fluids. Highly soluble salts can be promising alternatives of sodium chloride, provided that optimised membranes for such new salts will be developed. A more detailed investigation on the selection of suitable salt is presented in par. 8.4.

The selection of different solvent could be also taken into account to enhance the regeneration stage. In particular, some organic solvents such as methanol, ethanol, acetonitrile can be explored for such purpose. For instance, the use of a solvent with lower latent heat of evaporation or lower boiling point than water may reduce the regeneration costs, allowing to exploit waste heat at lower temperature range as thermal energy source.

On the other hand, the use of unconventional artificial solutions requires the development of proper ion exchange membranes. In fact, most of the IEMs currently available on the market are purposely designed for aqueous solutions of sodium chloride. The use of different salt/solvent, including the use of azeotropic water/organic mixtures, may require adaptations and new materials for the membrane compositions, in order to maintain low electrical resistance and high permselectivity in the new process conditions.

The use of thin membranes has been already proven to benefit the RED process. The development of thinner membranes would allow to increase power densities [71,84]. Moreover, profiled membranes [26] can be taken into account to improve the overall system fluid dynamic and energy generation performance. In fact, avoiding the use of net spacers is also beneficial to eliminate a major cost element.

New membrane structure can be also investigated to reduce the osmotic flux, which in fact causes a reduction of the RED process efficiency [39]. In general, the water permeability of the IEM is reduced by increasing polymer cross-linking: however, this causes also an increase of membrane resistance. An alternative approach to the solvent-flow management can be the use of charge-mosaic membranes, i.e. membranes constituted by parallel arrays of cation- and anion-exchange elements [112].

Using new membrane structures and process conditions, a different stack design may be needed for RED heat engine. In particular, different geometrical configuration can be taken into account, in terms of width/length ratio, channel thickness, optimised geometry for profiled membranes, feed streams distribution systems.

The likely increase of current density due to the artificial solutions may also require a further investigation of the electrode compartments. With this regard, capacitive electrodes [113] could be considered as a promising option for enhanced RED process: in this case, no redox couple is required, thus preventing gas evolution and production of unwanted species from electrode reactions.

Aside from the technological barriers related to the RED stage, a careful study of the regeneration stage is required to enhance the efficiency of the overall process. A separation process for regenerating the artificial salinity gradient can be based either

on the extraction of salt from the outlet dilute ($F_{d,out}$ stream in Figure 8.3), or on the extraction of solvent from the outlet concentrate ($F_{c,out}$ stream in Figure 8.3). Therefore, two categories of "solvent extraction" and "salt extraction" processes can be identified.

The main technological challenges for the development of the RED heat engine are summarised in Table 8.4.

Table 8.4. Technological challenges for the development of RED heat engine.

Component	**Technological challenges**	**Possible alternatives**
Working fluids	Increasing power density and efficiency of the closed-loop process	• high soluble salts (e.g. LiBr, $LiNO_3$, $KC_2H_3O_2$) • thermolytic salts (NH_4HCO_3) • Use of organic solvents (e.g. methanol, ethanol, acetonitrile)
Ion exchange membranes	Development of suitable membranes for RED heat engine	• new IEMs to be designed according to the adopted working fluids • profiled membranes • better membranes for controlling osmosis
Stack design	Improving design for RED heat engine	• Modifying aspect ratio • Improving geometry of profiled membranes • Optimising feed streams distribution systems
Electrode system	Selection of new redox processes and electrodes for artificial solutions	• new electrode system for reaching higher current density conditions • use of capacitive electrodes
Regenerative process	Selection of suitable process for regenerating working fluids by low-T waste heat	• solvent extraction • salt extraction
Overall process	High energy efficiency	• suitable working fluids to enhance power density • cost-effective regeneration process

8.4 Investigation of new salts for RED heat engine

The performance of all electrochemical processes is strongly affected by the physical properties of the electrolyte solutions, especially when highly concentrated solutions are used. In general, a suitable salt for RED applications should have:

- *High solubility in water.* Solubility in water defines a clear physical threshold to the maximum concentration exploitable for salinity gradient, thus increasing the driving force for RED process. The solubility of sodium chloride in water is sensibly high, being 5.5 M (36 gr. salt/100 gr. water) at 25°C [95]. Other inorganic salts, such as $LiClO_3$ and KNO_2 have a remarkably high solubility [95], allowing in principle to reach a salinity ratio (i.e. ratio between C_{HIGH} and C_{LOW}) up to 200-300.
- *High equivalent conductivity of the aqueous solution.* The equivalent conductivity has a strong impact on stack resistance, being most likely the highest contribution to the overall internal resistance [20]. With this regard, it is worth noting that the NaCl gives rather highly conductive aqueous solution, compared to other common inorganic salts.

Based on such properties, 16 uni-univalent salts have been selected and compared with sodium chloride (Table 8.5). The use of bivalent salts were not taken into account, as bivalent ions are generally responsible to increase the membranes resistance [88,90].

Table 8.5. List of salts investigated for RED heat engine.

Salt	Formula	Molecular weight	Solubility in water at 25°C * (mol/l)	Conductivity of saturated solution at 25°C * (mS/cm)
Ammonium Bromide	NH_4Br	97.94	6.39	390.5
Ammonium Chloride	NH_4Cl	53.49	5.74	388.6
Ammonium Bicarbonate	NH_4HCO_3	79.06	2.68	116.8
Ammonium Nitrate	NH_4NO_3	80.04	11.70	353.1
Lithium Bromide	LiBr	86.84	13.13	189.4
Lithium Chlorate	$LiClO_3$	90.39	15.31	14.9
Lithium Chloride	LiCl	42.39	14.76	163.2
Lithium Nitrate	$LiNO_3$	68.95	10.11	81.7
Potassium Acetate	$KC_2H_3O_2$	98.14	12.32	88.6
Potassium Bromide	KBr	119	4.97	370.1
Potassium Chloride	KCl	74.55	4.15	298.4
Potassium Fluoride	KF	58.1	13.88	265.2
Potassium Nitrate	KNO_3	101.1	3.31	192.3
Sodium Bromide	NaBr	102.89	7.46	262.3
Sodium Chlorate	$NaClO_3$	106.44	7.27	162.0
Sodium Chloride	NaCl	58.44	5.50	239.7
Sodium Nitrite	$NaNO_2$	68.99	10.15	47.0

* Source: [95,114].

Up to now, only ammonium bicarbonate has been proposed as an alternative salt to sodium chloride in RED systems [45,93]. However, this salt has been investigated only experimentally, while no modelling efforts has been presented for describing the different process conditions. Moreover, the modelling works so far proposed in the literature on RED process are based on the use of NaCl solutions, thus not predicting the process behaviour using different salts.

With this regard, a new model is here proposed for estimating the maximum power production by reverse electrodialysis using different salt solutions. In particular, the aim of the model was to evaluate the optimal feed concentration for both dilute and concentrated streams that maximise the power output, using different type of salt in the saline solutions (Table 8.5). Notwithstanding the model presented in Chapter 3, the development of a new model has been necessary for this purpose. The properties of solutions were estimated through generalized correlations that allowed to take into account the use of different salts. As a result, the model estimates

the power output of RED unit using different salts, thus identifying possible alternatives to sodium chloride for enhancing the performance of RED process. The following assumptions were made for modelling purposes:

a) All solutions' and cell pairs' variables are evaluated at the average conditions between inlet-outlet of the feed channels;
b) Constant membrane properties (permselectivity, resistance);
c) Neglecting solvent transport through membranes;
d) Neglecting polarisation phenomena;
e) Ideal current distribution (i.e. no parasitic currents).

Among the aforementioned assumptions, one of the strongest is certainly the definition of constant membranes properties. In fact, IEMs properties can change significantly when changing the type of salt [115] and its concentration. However, the lack of reliable information in the literature regarding membrane properties with different salt solutions, leading to the need of adopting the experimental information available for the case of NaCl solutions [82].

For the sake of clarity, the whole set of equations of the new model will be reported, though some of the equations involved have been already presented in the previous model (par. 3.3).

8.4.1 Model equations

The physical properties of solutions have been estimated in terms of activity coefficients, equivalent conductivity and density. In particular, activity coefficients are calculated through the correlation proposed by Staples [116]:

$$\ln \gamma = \frac{-\left|z_+ z_-\right| A_\gamma \, m^{1/2}}{1 + B_\gamma \, m^{1/2}} + C_\gamma \, m + D_\gamma \, m^2 + E_\gamma \, m^3 \qquad (8.2)$$

where A_γ = 1.17625 kg$^{1/2}$ mol$^{-1/2}$, m is the molality of the solution (equal to the ionic strength, for 1:1-valent electrolyte [72]), z_+ and z_- are the cation and anion valence numbers, respectively. The coefficients B_γ, C_γ, D_γ, E_γ are evaluated for each

investigated salt by fitting experimental data collected from the literature [114]. Their values may be found in Appendix B.

The equivalent conductivity is estimated by means of Jones and Dole' equation [117]:

$$\Lambda = \Lambda_0 - \frac{A_\Lambda \, c^{1/2}}{1 + B_\Lambda \, c^{1/2}} - C_\Lambda \, c \tag{8.3}$$

where Λ_0 is the equivalent conductivity of salt at infinite dilution, A_Λ, B_Λ, C_Λ are model parameters used for fitting, and c is the molar concentration. The negative term proportional to the concentration in eq. (8.2) allows this correlation to be in good agreement with experimental data for highly concentrated solutions. The values of these parameters for each salt are reported in Appendix B, while the agreement with the experimental data for some investigated salts is shown in Figure 8.4.

The solutions density has been estimated as a linear function of molal concentration for both dilute/concentrated solutions:

$$\rho = \rho_0 + \left(\frac{\Delta \rho}{\Delta m} \right) m \tag{8.4}$$

where ρ_0 is density of pure solvent at 25°C, and the slope of the line was evaluated by fitting experimental data from literature ([114], parameters values are reported in Appendix B).

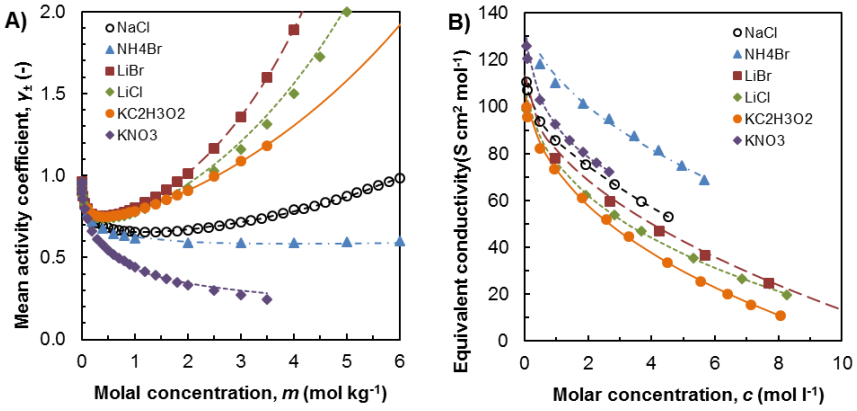

Figure 8.4. Estimated properties for some of the investigated aqueous solutions at 25°C. A) Mean activity coefficient. B) Equivalent conductivity. Symbols: experimental data [114]. Lines: model predictions.

The cell pair voltage (E_{cell}) is determined by Nernst equation [11]:

$$E_{cell} = \left(\alpha_{CEM} + \alpha_{AEM}\right) \frac{R\,T}{F} \ln\left(\frac{\gamma_{HIGH}\ m_{HIGH}}{\gamma_{LOW}\ m_{LOW}}\right) \tag{8.5}$$

where R, T, and F have their usual meaning, α_{AEM}, α_{CEM} are the permselectivity of AEM and CEM, and the subscripts *HIGH* and *LOW* refer to concentrated and dilute streams, respectively. For the sake of simplicity, the effect of salt nature/concentration on permselectivity has been neglected, assuming constant values of 0.65 and 0.90 for AEM and CEM permselectivity, respectively. These values were experimentally measured for Fujifilm membranes using 0.5 M NaCl - 4 M NaCl solutions [82].

The electrical resistance of both solutions are evaluated according to Ohm's law:

$$R_{LOW} = f\,\frac{\delta_{LOW}}{\Lambda_{LOW}\ c_{LOW}} \qquad R_{HIGH} = f\,\frac{\delta_{HIGH}}{\Lambda_{HIGH}\ c_{HIGH}} \tag{8.6-8.7}$$

Where δ_{LOW}, δ_{HIGH} are *LOW* and *HIGH* compartment thicknesses, while f (spacer shadow factor) is a geometric constant accounting for the presence of a non-conductive spacer inside the channels (f = 1.56 for the adopted 270 μm woven spacer). Therefore, the electrical resistance of the whole cell pair is given by:

$$R_{cell} = R_{LOW} + R_{HIGH} + R_{AEM} + R_{CEM} \tag{8.8}$$

where R_{AEM}, R_{CEM} are AEM and CEM resistance, respectively.
The total stack resistance may be evaluated as:

$$R_{stack} = N\, R_{cell} + R_{blank} \tag{8.9}$$

where N is the number of cell pairs, and R_{blank} is the electrode compartments resistance (blank), which is considered as a constant based on previous experimental results (R_{blank} = 0.4 Ω [82]).

The Open Circuit Voltage (OCV) can be defined as the voltage arising from N cell pairs in zero-current conditions:

$$OCV = N\, E_{cell} \tag{8.10}$$

The stack voltage is evaluated as sum of all cell pair voltage minus the internal ohmic losses:

$$E_{stack} = OCV - R_{stack}\; j \tag{8.11}$$

where j is the electrical current density through the stack, given by:

$$j = \frac{E_{stack}}{R_{ext}} \tag{8.12}$$

where R_{ext} is the external load of the system. It is possible to demonstrate that the maximum power output is reached when the external load is equal to the stack resistance [20]. Therefore, the following condition has been added to the model to estimate the maximum power output:

$$R_{ext} = R_{stack} \tag{8.13}$$

Salt flux through membranes can be estimated as

$$J_{salt} = \frac{j}{F} + 2\,\frac{D_{salt}\left(c_{HIGH} - c_{LOW}\right)}{\delta_m} \tag{8.14}$$

where D_{salt} is the salt permeability coefficient through membranes and δ_m is IEM thickness. The salt permeability coefficient has been assumed as constant (D_{salt} = 10^{-12} m^2/s). In fact, in practical conditions the diffusion term in eq. (8.14) has a minor role with respect to the migration term, due to the permselectivity of the membranes. Therefore, the assumption of a constant salt permeability coefficient can be assumed as reliable, as previously demonstrated (par. 4.1.1).

The overall mass balance in the concentrate compartment is given by:

$$c_{HIGH,out} - c_{HIGH,in} = -\frac{J_{salt}\,A}{Q} \tag{8.15}$$

In eq. (8.15), A is the membrane active area and Q is the volumetric flow rate in a single compartment, while $c_{HIGH,out}$ and $c_{HIGH,in}$ are the outlet and inlet concentration

for the concentrated stream, respectively. Likewise, a mass balance for the dilute stream can be written (with opposite sign for salt flux).

Finally, the specific power per cell pair area (power density) is evaluated as:

$$P_d = \frac{j^2 R_{ext}}{N} \tag{8.16}$$

The overall set of equations (8.2-8.16) has been afterwards implemented in a solver software especially suitable for optimization problems (GAMS [118]). This model allowed to find the optimal values of feed concentration ($c_{LOW,in}$ and $c_{HIGH,in}$) that maximise the gross power density (eq. (8.16)) for each investigated salt. The only constraint for this optimisation study is that $c_{HIGH,in}$ must be lower than the salt solubility limit.

8.4.2 Model predictions and results

The developed model, although not being yet experimentally validated, was used to investigate the maximum power density achievable with a lab-scale RED unit (10x10 cm^2, 10 cell pairs) using different salts. In particular, the model is in fact able to compare qualitatively the behaviour of different salts with sodium chloride, though based on the assumption of constant IEMs properties.

Figure 8.5 shows both the maximum power density and the open circuit voltage achievable with different salt solutions; two dashed lines are shown for the case of sodium chloride, adopting such salt as benchmark.

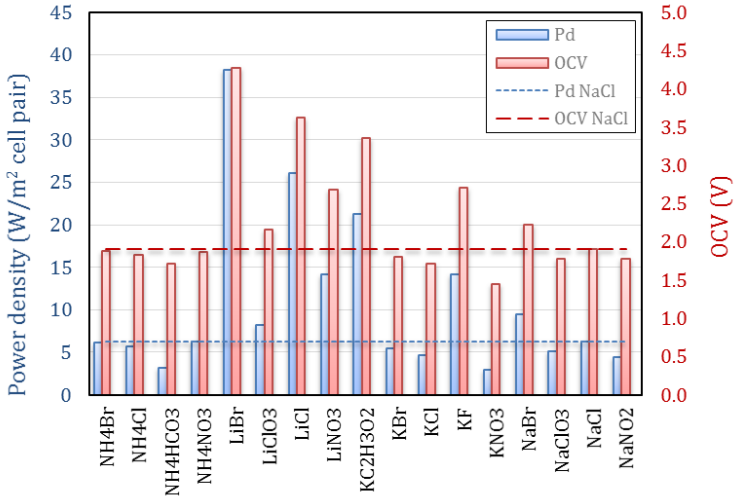

Figure 8.5. Max power density and OCV achievable using different salts solutions. Simulations of a RED unit (10x10 cm^2, 10 cell pairs) equipped with Fujifilm membranes (α_{AEM} = 0.65, α_{CEM} = 0.90; R_{AEM} = 1.55 Ω cm^2; R_{CEM} = 2.96 Ω cm^2), 270 µm woven spacers. T = 25 °C; v = 1 cm/s. Dashed lines for NaCl case are shown as benchmark.

Figure 8.5 clearly shows that different salts solutions give a power density significantly higher than NaCl case. In particular, the use of some salts, such as LiBr, can lead to power output more than 6 times higher than conventional NaCl solutions. In some cases, as for lithium nitrate ($LiNO_3$) and potassium acetate ($KC_2H_3O_2$), the significant enhancement in power output is due to a combined effect of higher OCV and lower stack resistance with respect to NaCl case.

However, it is worth noting that the reliability of these predictions strongly depends on the properties of the available membranes. In fact, commercial ion exchange membranes can unlikely operate with such high performance using non-conventional salts solutions. Therefore, the development of new membranes purposely designed for different salts could be crucial to exploit the benefit of artificial salinity gradients.

Figure 8.6 shows the optimal feed concentrations evaluated by the model for both concentrate and dilute. For most of the investigated salts, the model predicts an optimal concentration of the concentrate equal to the solubility limit in water at 25°C. This limit was set as a physical constraint for the model in the optimisation study. As

a result, a feed concentration as high as possible for the concentrate is preferable in most cases for enhancing the power output. However, such statement is not generally true, as some salts (e.g. $LiClO_3$, LiCl, $NaNO_2$) show an optimal concentration significantly lower than the solubility limit. For these salts, a further increase of the feed concentration would cause a reduction of the power output achievable, likely due to an increase of the stack resistance despite the higher salt concentration.

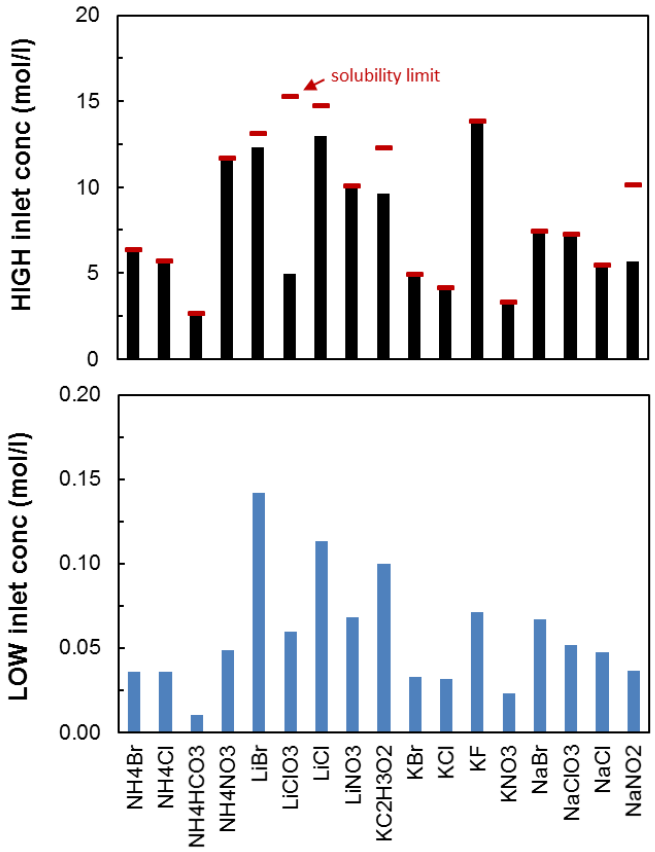

Figure 8.6. Optimal feed concentration for concentrate (above) and dilute (below). Simulations of a RED unit (10x10 cm^2, 10 cell pairs) equipped with Fujifilm membranes (α_{AEM} = 0.65, α_{CEM} = 0.90; R_{AEM} = 1.55 Ω cm^2; R_{CEM} = 2.96 Ω cm^2), 270 µm woven spacers. T = 25 ˚C; v = 1 cm/s.

Regarding the dilute stream, the optimal concentration lies in a relatively narrow range for all the investigate salts, i.e. between 0.01 M and 0.015 M.

The areal resistance of cell pair components (CEM, AEM, dilute and concentrate) are shown in Figure 8.7. While the resistance of the concentrated solution is practically negligible in all cases, the diluate resistance may be the main contribution to the overall stack resistance for some salts.

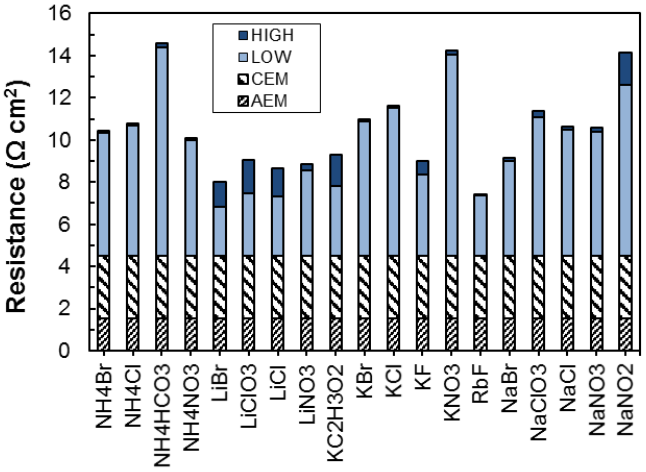

Figure 8.7. Area resistances of cell pair components using different salts. A constant resistance of AEM and CEM is assumed as constant. Simulations of a RED unit (10x10 cm^2, 10 cell pairs) equipped with Fujifilm membranes (α_{AEM} = 0.65, α_{CEM} = 0.90; R_{AEM} = 1.55 Ω cm^2; R_{CEM} = 2.96 Ω cm^2), 270 μm woven spacers. T = 25 ˚C; v = 1 cm/s.

The model predictions shown in Figure 8.7 are obtained assuming constant resistance for the ion exchange membranes, according to the properties of Fujifilm membranes in 0.5 M – 4 M NaCl solutions [82]. In all the investigated cases, the electrical resistance of the membranes is a significant contribution of the stack resistance, indicating that the development of IEMs with lower resistance can lead to a remarkable reduction of the ohmic losses.

8.5 Regeneration technologies for RED heat engine

A crucial aspect in the development of a RED heat engine system is the selection of a cost-effective separation process for regenerating the exhausted streams of the RED unit. In particular, a suitable separation process should restore the original

salinity of concentrate and diluate by using a thermal energy source at very low temperature. Up to now, only conventional distillation has been proposed as regeneration technology for closed-loop RED [45,93,102]. However, a variety of conventional and innovative process can be ideally used for this purpose, providing higher energy efficiency than conventional distillation.

The state of the art of low-temperature separation technologies is closely related to the field of seawater desalination: therefore, conventional processes such as Multiple Effect Distillation (MED) or Membrane Distillation (MD) could be promising options for RED heat engine applications.

The processes considered in this section are grouped in two categories, based on the regeneration strategy and on the heat source temperature: (i) solvent-extraction processes (operating in the range of 60-100°C), and (ii) solute-extraction processes (which can operate, in principle, with heat source temperature as low as 40°C).

Regeneration strategy by solvent extraction

The regeneration strategy based on "solvent extraction" is outlined in Figure 8.8. The two solutions are regenerated by partial evaporation of the solvent from the concentrated stream (F_2) exiting the RED unit. In order to rebalance the salt transfer within the RED unit from the concentrated to the dilute solution, a preliminary mixing of stream F_1 into F_2 is needed, thus restoring the original amount of solute in the concentrate loop. The stream F_2 is then processed in the regeneration unit, resulting into two exiting streams: a solute-rich stream (the regenerated "concentrate stream", F_5 or $F_{c,in}$), and an ideally solute-free stream (F_4), which is then mixed with the stream F_3 to give the regenerated diluate ($F_{d,in}$).

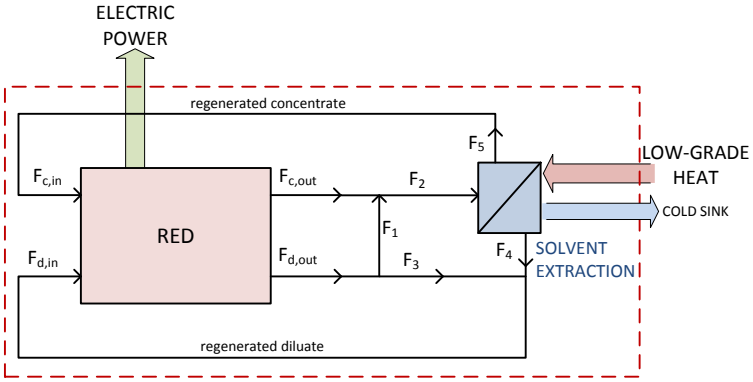

Figure 8.8. Conceptual scheme of RED heat engine with solvent extraction as regeneration strategy.

Conventional evaporative processes can be considered for the solvent extraction stage shown in Figure 8.8. In particular, Multiple Effect Distillation (MED) and Membrane Distillation (MD) can be very promising options, being the most efficient and the most innovative technology in the desalination industry, respectively [119]. Aside from these broadly applied technologies, other emerging desalination processes with reduced energy costs could be also adopted for RED heat engine applications. For instance, novel processes based on vapour regeneration by adsorption/desorption cycles (i.e. adsorption desalination [120]) can halve the specific energy consumptions with respect to conventional desalination processes.

Thanks to the use of artificial solutions in a closed-loop system, the evaporative processes can also work under new operating conditions, which are not feasible for the desalination industry. For example, MED units can operate at temperatures higher than 70ºC, which is generally avoided in seawater desalination to prevent precipitation of scarcely soluble salts present in the feed.

On the other hand, some novel design of membrane distillation modules could be also useful to maximize internal heat recovery, e.g. spiral-wound or vacuum multi-effect (V-MEMD) configurations. This latter configuration consists of a number of units where vapour is separated from the evaporating solutions by means of a hydrophobic membrane [121]. As a result, V-MEMD is similar to the conventional MED process, but more flexible and scalable technology.

Regeneration strategy by solute extraction

The concept of "solute extraction" is sketched in Figure 8.9. This method is based on the thermo-sensitivity properties of the salt, which can be recovered from the exhausted dilute stream by causing a strong variation of solubility or thermal degradation at temperature above 40-50°C.

Within the RED unit, salt transport occurred from concentrate to diluate due to the salinity gradient across membranes. Water transport through IEMs is caused by two counteracting phenomena, i.e. osmosis and electro-osmosis: however, the osmotic flux is generally dominant in RED systems, thus a net water transport from diluate to concentrate is observed [39,82]. As a result, the exhaust diluate exiting from the RED stage contains an excess of salt, while the exhaust concentrate contains an excess of water.

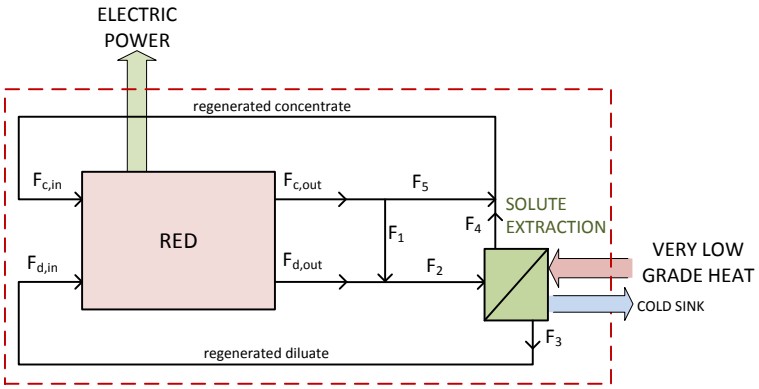

Figure 8.9. Conceptual scheme of RED heat engine with solute extraction as regeneration strategy.

In the scheme shown in Figure 8.9, a by-pass stream (F_1) from the concentrate loop is mixed with the stream outlet dilute ($F_{d,out}$), in order to restore the amount of solvent into the diluate loop. Therefore, the excess of salt from exhaust diluate ($F_{d,out}$) is recovered through the solute extraction stage.

The exiting streams from the solute extraction stage are a solvent-rich stream (F_3), which constitutes the regenerated diluate ($F_{d,in}$), and an ideally pure solute stream (F_4), which can be used to regenerate the concentrate feed solution ($F_{c,in}$).

Based on the thermo-sensitivity properties of the salt, two different options can be taken into account for the solute extraction process:

- *Thermolytic salts*. The salt is converted into gaseous species by a thermal degradation process. An example of these compounds is ammonium bicarbonate (NH_4HCO_3), which is converted into ammonia, carbon dioxide and water, developing a gas phase very easy to separate from the liquid solution when temperature exceeds ~40-50°C (depending on unit pressure [94]).
- *Switchable-solubility salts*. These salts are able to change their polarity and, therefore, their solubility in aqueous solutions within carbonation/de-carbonation and heating/cooling cycles.

8.6 Analysis of potentials: energy efficiency of a RED heat engine

The developed model for the RED stage (par. 8.4) has been used for evaluating the power production of a RED heat engine using different type of salt solutions. The same model, coupled with simple additional mass and energy balance equations for the process schemes presented (Figure 8.8-Figure 8.9), can be adopted to calculate the energy efficiency of RED heat engine. In this way, a theoretical estimation of the energy efficiency is presented in this section, aiming to demonstrate the potential application of some RED heat engine systems, and provide indications for further development of the process. In particular, although the values assumed for membranes properties and specific energy consumptions of the regeneration stages are optimistic figures, these values could be reasonably achieved in the near future.

The energy efficiency of RED heat engine (η) has been evaluated as:

$$\eta = \frac{P}{Q_{wh}} \tag{8.17}$$

where P is the electric power produced by the RED unit, while Q_{wh} is the thermal energy supplied as waste heat in the regeneration stage.

Apart from the energy efficiency, the performance of RED heat engine has been evaluated also in terms of *exergetic* efficiency. Exergy (or "available work") of a system is defined as the maximum theoretical amount of work achievable when a heat flow is converted into power in a generic thermodynamic cycle. Therefore, it can be seen as a form of energy that accounts for the "grade" at which the energy is available, providing a correct measure of the work potential of heat.

For RED heat engine, the power output of the cycle (i.e. electric energy) can be considered as pure exergy. The power input (thermal energy) has an exergetic content that depends on the temperature level of the heat source: the higher the heat source temperature, the higher is the exergetic content of the heat and therefore the theoretical work obtainable. It can be demonstrated that the exergetic efficiency (η_{ex}) is practically equal to the ratio of the energy efficiency of the heat engine (η) and the corresponding Carnot efficiency:

$$\eta_{ex} = \frac{\eta}{\eta_c} \tag{8.18}$$

In order to estimate the energy efficiency of RED heat engine, two different case studies have been analysed:

- *Case I: recovery of waste heat at low T (~90°C).* For this reference case, sodium chloride aqueous solutions were considered in the RED stage, assuming a regeneration step by Multiple Effect Distillation (MED).
- *Case II: recovery of waste heat at very low T (~60°C).* This scenario is based on the use of ammonium bicarbonate, with a thermal degradation process for the regeneration stage.

It is worth noting that the choice of NaCl solutions was related to the availability of reliable information on membrane properties at the state of the art of the RED technologies only for this salt. Thus, the analysis has been performed with NaCl in order to predict an optimistic, though realistic, scenario, which could be significantly improved if novel components (e.g. membranes, regeneration stage, etc.) optimised for unconventional salt solutions will be developed.

For the RED stage, a large-scale unit (50x50 cm^2, 1000 cell pairs) has been considered in this analysis. Ion exchange membranes with permselectivity of 0.9 and electrical resistance of 0.5 Ω cm^2 have been taken into account: although commercial IEMs may not have yet such properties, these values are reasonably achievable by new IEMs in the next future, aiming at the improvement the performance of the RED stage. The overall conditions of the analysis are reported in Table 8.6.

Table 8.6. Overall conditions for the estimation of energy efficiency of RED heat engine*.

		Case I Low T process	**Case II Very low T process**
	Waste heat source temperature (°C)	90	60
RED stage	Salt	NaCl	NH_4HCO_3
	Concentrate concentration (mol/l)	5	2.5
	Diluate concentration (mol/l)	0.01	0.01
	Concentrate flow velocity (cm/s)	1	1
	Diluate flow velocity (cm/s)	0.3	2
	Temperature (°C)	40	20
Regeneration stage	Technology	MED	Thermal degradation
	Energy consumption (kWh_{th}/m^3 of extracted solvent)	25	-
	Energy consumption (kWh_{th}/mol of extracted salt)	-	100

* Simulations of a RED unit (50x50 cm^2, 1000 cell pairs) equipped with 200 μm spacers. Membrane permselectivity: $\alpha_{AEM} = \alpha_{CEM} = 0.90$. Membrane resistance: $R_{AEM} = R_{CEM} = 0.5$ Ω cm^2.

The amount of thermal energy required in the regeneration stage should be estimated case by case, according to the adopted regeneration technology and process layout. For the first case study, Multiple Effect Distillation (MED) has been taken into account for the regeneration stage. Conventional MED plants require 40 to 50 kWh_{th}/m^3 of distillate [119]. In the adopted scenario, a target of 25 kWh_{th}/m^3 has been set, assuming a heat source at 90°C.

In the second investigated case, the use of ammonium bicarbonate has been taken into account. For such salt, the enthalpy of formation is +125 kJ/mol and the mixing enthalpy (endothermic reaction, referred to the formation of a 0.1-0.2M solution) is -25 kJ/mol [94]. Therefore, a total amount of energy of about 100 kJ/mol of salt is required in the regeneration stage. A temperature increase of 5°C for the dilute solution can be provided by an additional quote of thermal energy, while the remaining heating (for a larger temperature variation in the process streams to better perform the separation) can be achieved by a thermal integration of the process. As a result, a heat source at 60°C would suffice for the regeneration stage.

Based on the above-mentioned assumptions, the model predictions results obtained are reported in Table 8.7.

Table 8.7. Estimation of energy efficiency of RED heat engine*.

Performance factor	**Case I** **Low T process**	**Case II** **Very low T process**
Power density (W/m^2)	9.97	10.3
Brine potential energy (kWh/m^3)	0.84	0.87
Energy efficiency (%)	12.8	5.1
Carnot efficiency (%)	19	12
Exergetic efficiency (%)	67	42

* Simulations of a RED unit (50x50 cm^2, 1000 cell pairs) equipped with 200 μm spacers. Membrane permselectivity: $\alpha_{AEM} = \alpha_{CEM} = 0.90$. Membrane resistance: $R_{AEM} = R_{CEM} = 0.5\ \Omega\ cm^2$.

For the first case, a total energetic efficiency of 12.8% is estimated, which corresponds to an exergetic efficiency of 67%. Conversely, for the second case a total

energetic efficiency of 5.1% has been estimated, equivalent to an exergetic efficiency of 42%.

Finally, the estimated exergetic efficiency of RED heat engine has been compared with the state-of-the-art technologies for the conversion of waste heat into power (Figure 8.10). In particular, the diagram reports the typical operating temperature range of the process, along with the theoretical efficiency achievable according to the Carnot cycle (on the secondary horizontal axis).

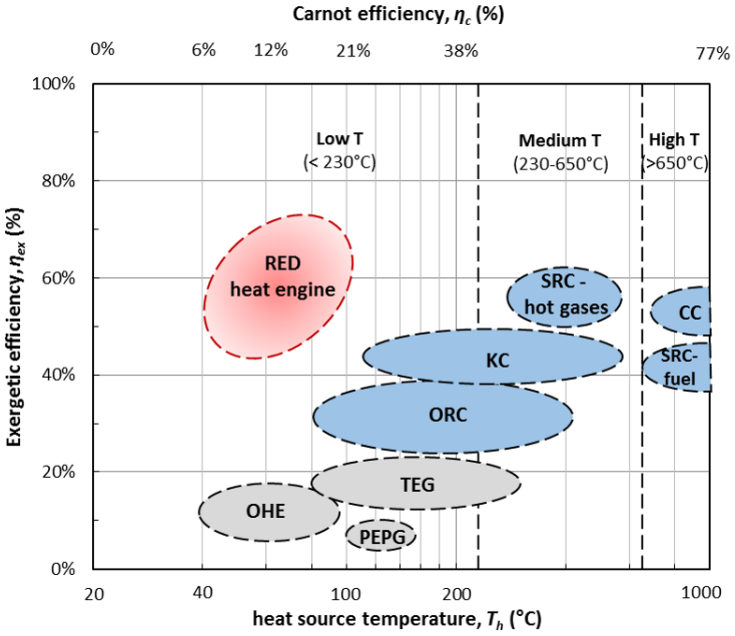

Figure 8.10. State of the art technologies for the conversion of heat into power. Grey circles refer to technologies at very early stage of development. The Carnot efficiency (on the secondary horizontal axis) is evaluated assuming a cold sink temperature of 20°C. Source: [103,107,110,122].
SRC-hot gases: Steam Rankine Cycle integrated with gas turbine/other topping cycles; SRC-fuel: Steam Rankine Cycle directly fuelled by oil, coal or other fuels; KC: Kalina Cycle; ORC: Organic Rankine Cycle; TEG: Thermoelectric Generation; PEPG: Piezoelectric Power Generation with waste heat-powered expansion/ compression cycle; OHE: Osmotic Heat Engine.

Figure 8.10 clearly shows as RED heat engine could be the only suitable technology for recovering waste heat at very low temperature, especially at T<100°C. Therefore, based on the model predictions, RED heat engine may give a significant improvement of the current state-of-the-art.

8.7 Outlook and final remarks

The aim of this work has been an investigation of the feasibility of RED heat engine for waste heat recovery at low temperature range.

The presented optimisation study showed the potential of non-conventional salts for enhancing the power output of RED systems. Moreover, it gives a preliminary screening of possible alternatives different from sodium chloride, demonstrating that a number of salts could be ideally suitable for significantly improving the power output of the RED unit.

In order to develop a feasible technology for waste heat recovery, research efforts should be focused on the following points:

- Development of new ion exchange membranes, purposely designed for working with artificial salinity gradient;
- Experimental investigation of different salts and solvents, aiming to create suitable working fluids, in terms of power production and regeneration costs;
- proof-of-concept of the regeneration of exhaust solutions from RED stage through non-conventional separation processes;
- Experimental demonstration of RED heat engine technology on laboratory-pilot scale.

RED heat engine can be a truly promising option for waste heat recovery at very low temperature range. The actual resource that can be used for RED heat engine is notably higher. Waste heat at any temperature could be first used for other applications and then used by a RED heat engine in a cascading approach.

The selection of suitable working fluids and a cost-effective regeneration strategy are both relevant issues for the development of a feasible technology for recovering waste heat at low temperature. The investigation of a wide range of regeneration technologies, salts and solvents might lead to a significant improvement of the current energy efficiency, towards the development of new applications for electro-membrane processes and new ion exchange membranes with high performance and low cost.

CONCLUSIONS

The aim of this thesis has been an in-depth investigation on the reverse electrodialysis process throughout modelling and experimentally activities, which eventually led to the construction of the first demonstration plant fed with concentrated brines.

The main achievements of the research activities presented can be summarised as follows:

i. *Development of a multi-scale model for RED process.* A new model for the RED process has been developed and validated. The model, based on multi-scale approach, was able to predict the process behaviour under conditions unexplored before, using highly concentrated solutions.

ii. *Experimental investigation on laboratory-scale.* A wide experimental campaign has been performed on a RED lab-scale unit, leading to values of power density among the highest reported in the literature. The information collected during such tests provides original data for model validation.

iii. *Design, construction and testing of a RED pilot plant.* A RED pilot plant was designed and installed in Marsala (Trapani, Italy) as final accomplishment of the REAPower project. The plant, which has been tested over six months of operation, represents the first plant worldwide operating with real brine and brackish water.

iv. *Conceptual analysis of a 'RED heat engine' system.* A novel application for the RED technology was been investigated, aiming to recover industrial waste heat via electricity generation by reverse electrodialysis.

For the above main points, the following concluding remarks are here made.

i. *Development of a multi-scale model for RED process.* The first research efforts were devoted to the development and validation of the new RED model. Implementing the model in an equation-based solver software (gPROMS), a user-friendly simulator for the RED process was built and further exploit for analysing

the RED technology at different scales. The model validation was carried out using original experimental data collected on a laboratory RED unit (10x10 cm^2, 50 cell pairs). After the calibration, a good match has been found with experiments in a wide range of feed salt concentration. Optimal feed conditions have been identified for the adopted system, i.e. employing brackish water (0.08-0.1 M NaCl) as diluate and brine (4.5-5 M NaCl) as concentrate. Based on these findings, the use of brackish water and saturated brine have been later considered for the design and operation of the pilot plant. For the first time, the effect of asymmetric path has been investigated, i.e. using different path length for diluate and concentrate inside a RED unit. In particular, the simulation of a longer path length for diluate leads to a significant reduction in the power output, while a weaker effect is registered for longer path length for concentrate. On the other hand, increasing the concentrate path length enhances almost proportionally the power output and the overall process yield. Therefore, a longer path length for concentrate might be considered to enhance the process performance on larger scale. In order to provide indications for scaling-up the RED process, the operation of a RED plant with three modules was simulated, considering different operating conditions and flow arrangement (i.e. parallel or serial feed). The stronger influence on process performance has been attributed to the diluate, both in terms of concentration and flow rate. In particular, the availability of brackish water is a key factor for the plant performance.

ii. *Experimental investigation on laboratory-scale.* Aside from giving input for model validation, the experimental campaign performed on the laboratory RED unit (10x10 cm^2, 50 cell pairs) led to significant outcomes for characterising the best process conditions. Following the model predictions and the indications coming from previous experiments, a power density of 12 W/m^2 of cell pair was reached, using 0.1 M NaCl as diluate and 5 M NaCl as concentrate at 40°C. These results, among the highest so far reported in the literature, clearly demonstrate that a careful selection of process conditions and membranes properties can lead to a successful scale-up of the RED technology.

iii. *Design, construction and testing of a RED pilot plant.* The aforementioned results, together with the R&D activities carried out within the REAPower project, led to the design and construction of the first RED pilot plant fed with real brackish water and brines from saltworks. The plant is located in a saltworks area in Marsala (South of Italy), which is an ideal location for demonstrating the application of RED process in real environment. During the plant scale-up, three different RED modules were installed and tested: a first "small" prototype (44x44 cm^2, 125 cell pairs) and two larger prototypes (44x44 cm^2, 500 cell pairs each). Overall, the REAPower pilot plant has been operating for six months, both using real solutions (saturated brine and brackish water) and artificial NaCl solutions with the same conductivity of natural streams. The overall capacity registered for the plant was almost 700 W using artificial solutions with the same conductivity of natural streams. Using real brine and brackish water, a power output of nearly 330 W was reached: such performance reduction may be mainly attributed to the presence of different ions (especially Mg^{2+}) in the natural streams, causing an increase of the membranes resistance. With such figures, the REAPower pilot plant represents in fact the largest application worldwide of the reverse electrodialysis technology to date, and gives a truly demonstration of the feasible scaling-up of the process.

iv. *Conceptual analysis of a 'RED heat engine' system.* Exploring new field of applications for RED technology, the novel concept of RED heat engine has been broadly investigated. A new model has been purposely developed to study the effect of different salts on power output. In this way, some salts (e.g. lithium bromide or potassium acetate) have been identified as promising alternative to NaCl, though further investigations are required. In particular, the development of new ion exchange membranes with suitable properties for such solutions may well result into an increase of one order of magnitude for the values of power produced by reverse electrodialysis, thus notably boosting the economic feasibility of the process. Other salts, such as ammonium bicarbonate, might well be evaluated as

an alternative option to reduce the energy costs in the regeneration stage, therefore increasing the energy efficiency of the whole system.

Although notable achievements have been already reached during the last decade, the current development of RED process is still far away from demonstrating its huge potential. The research activities presented in this thesis, in line with the R&D strategies of the REAPower project, contributes to improve the state-of-the-art of the RED process. Moreover, the application of RED technology for the recovery of industrial waste heat can lead to new technological challenges, thus further exploring the potential of salinity gradient power.

ACKNOWLEDGEMENTS

This work could not be possible without the help of some brilliant students. I would like to thank Davide Bascone, Paolo Mazzola and Fabio Santoro for their work on process modelling. Paolo Modica, Giuseppe Russo and Marialaura Guarino are acknowledged for performing the experiments on the laboratory test-rig at VITO. I would like to thank Claudio Scalici and Davide Vaccari for designing and testing the pilot plant in Marsala, Ornella Calderone and Maurizio Bevacqua for their experimental work on closed-loop RED at Fujifilm.

I would like to express my deepest gratitude to Andrea and Giorgio, for being both good supervisors and friends. Their contributions to this thesis have been far from a simple supervision.

I would like to thank all the colleagues of the REAPower consortium, especially REDstack and Fujifilm, for the fruitful discussions during the project meetings.

Willem van Baak is especially acknowledged for his great support and help during my research periods at Fujifilm.

I would like to thank prof. Bogle for his help on process modelling and validation and model validation task during my research visit at UCL.

Luigi Gurreri and Alessandro Tamburini are acknowledged for their everyday help during this PhD.

Finally, I thank my parents for giving constantly strong support and great example, as I always remember in my life.

NOMENCLATURE

Latin letters

$a_{open,x}$	spacer open area in the direction along IEM (-)
$a_{open,y}$	spacer open area in the direction perpendicular IEM (-)
a	parameter of Islam et al.' equation (-)
A	membrane area or cell pair area, (m^2)
A_1	Debye-Hückel constant (0.3915 at 25°C)
b	channel (or membrane) width (m)
b'	constant of Pitzer equation (-)
B'	parameter of Islam et al.' equation, ($m^{1/2}$ $mol^{-1/2}$)
B'_1	parameter of Islam et al.' equation, (S m^3 $mol^{-3/2}$)
B'_2	parameter of Islam et al.' equation ($m^{3/2}$ $mol^{-1/2}$)
B^{γ}	second virial coefficient of Pitzer equation (kg mol^{-1})
B^{φ}	second virial coefficient of Pitzer equation (kg mol^{-1})
c	molar concentration (mol l^{-1})
C	salt concentration (mol m^{-3})
$\bar{C}'_{b,k}, \bar{C}'_{s,k}$	salt concentration averaged between inlet-centre of k-th channel
$\bar{C}''_{b,k}, \bar{C}''_{s,k}$	salt concentration averaged between centre-outlet of k-th channel
C^{γ}	third virial coefficient of Pitzer equation (Kg^2 mol^{-2})
C^{φ}	third virial coefficient of Pitzer equation (Kg^2 mol^{-2})
D_{NaCl}	NaCl permeability coefficient (m^2 s^{-1})
E_{cell}	cell pair voltage (V)
E_{stack}	stack voltage (V)
F	Faraday constant (96490 C mol^{-1})
f_y, f_x	spacer shadow factor in the direction perpendicular/along IEM (-)
f_m	shadow factor for membranes
F'	parameters of Islam et al.' equation (-)

I	electric current (A)
I'	ion strength (mol/l)
j	current density (A m^{-2})
J'_w	volumetric water flux (m^3 m^{-2} s^{-1})
J_{tot}	salt molar flux (mol m^{-2} s^{-1})
J_{eosm}	electro-osmotic flux (mol m^{-2} s^{-1})
J_{osm}	osmotic flux (mol m^{-2} s^{-1})
J_w	net water flux (mol m^{-2} s^{-1})
L	channel length (m)
L_p	water permeability coefficient ($m^3 \cdot bar^{-1} \cdot m^{-2} \cdot h^{-1}$)
m	electrolyte molal concentration (mol kg^{-1})
N	number or cell pairs (-)
P_d	gross power density (W m^{-2} cell pair)
$P_{d,net}$	net power density (W m^{-2} cell pair)
P_{pump}	pumping power (W)
Q_b, Q_s	brine/seawater flow rate in single channel (m^3 s^{-1})
Q_{tot}	total feed flow rate (m^3 s^{-1})
R	universal gas constant (8.314 J mol^{-1} K^{-1})
R_{AEM}, R_{CEM}	AEM/CEM areal resistance (Ω m^2)
R_b, R_s	brine/seawater areal resistance (Ω m^2)
R_{blank}	electrode compartments (blank) resistance (Ω m^2)
R_{cell}	cell pair resistance (Ω m^2)
R_{stack}	cells stack resistance (Ω m^2)
R_u	external load (Ω m^2)
T	temperature (K)
v	fluid velocity (m s^{-1})
x	flow direction (m)
z	ion valence (-)

Greek letters

α_{AEM}, α_{CEM}	AEM/CEM permselectivity (-)
β	permselectivity correction factor (-)
$\gamma_{\pm}$	mean activity coefficient (-)
δ_b, δ_s	brine/seawater compartment thickness (m)
δ_m	membrane thickness (m)
δ_{tot}	total cell pair thickness (m)
ε	dielectric constant (-)
ε_{sp}	spacer porosity (-)
ϕ	osmotic coefficient (-)
ϑ_b, ϑ_s	polarisation coefficients (-)
ΔC_b^*	concentration drops in the diffusion boundary layer for brine
ΔC_s^*	concentration drops in the diffusion boundary layer for seawater
ΔP	pressure drop (Pa)
$\Delta \Pi^*$	real osmotic pressure difference (Pa)
η	viscosity of solution (Pa s)
η_p	pump efficiency (-)
υ	van't Hoff factor (-)
Λ	equivalent conductivity (S m^2 mol^{-1})
Λ^0	equivalent conductivity at infinite dilution ($126.5 \cdot 10^{-4}$ S m^2 mol^{-1})
$\overline{\Lambda}'_{b,k}$ $\overline{\Lambda}'_{s,k}$	equivalent conductivity averaged between inlet-centre of k-th channel
$\overline{\Lambda}''_{b,k}$, $\overline{\Lambda}''_{s,k}$	equivalent conductivity averaged between centre-outlet of k-th channel

Subscripts and superscripts

c	collector
cell	cell pair
d	distributor
ext	external circuit
LOW	diluted solution
HIGH	concentrated solution
bulk	bulk conditions
int	membrane-solution interface

Acronyms

AEM	Anionic Exchange Membrane
CEM	Cationic Exchange Membrane
IEM	Ion Exchange Membrane
RED	Reverse Electrodialysis
SGP	Salinity Gradient Power
DBL	diffusion boundary layer
CFD	Computational Fluid Dynamics

APPENDICES

A. Properties of some homogeneous ion exchange membranes

Source: [53].

Membrane	Type	Thickness (mm)	IEC (mol/g (meq/g))	Area resistance (Ω cm2)	Remarks
Asahi Chemical Industry Co. Japan					
Aciplex K-192	CEM	0.13–0.17	–	1.6–1.9	Univalent selective
Aciplex-501SB	CEM	0.16–0.20	–	1.5–3.0	–
Aciplex A-192	AEM	>0.15	–	1.8–2.1	Univalent selective
Aciplex-501SB	AEM	0.14–0.18	–	2.0–3.0	–
Aciplex A201	AEM	0.22–0.24	–	3.6–4.2	Desalination
Aciplex A221	AEM	0.17–0.19	–	1.4–1.7	Diff. Dialysis
Asahi Glass Co. Ltd., Japan					
Selemion CMV	CEM	0.13–0.15	–	2.0–3.5	Strongly acidic
Selemion AMV	AEM	0.11–0.15	–	1.5–3.0	Strongly basic
Selemion ASV	AEM	0.11–0.15	–	2.3–3.5	Strongly basic, univalent
Selemion DSV	AEM	0.13–0.17	–	–	Strongly basic, dialysis
Flemion	–	–	–	–	Chlor-alkali
DuPont Co., USA					
Nafion NF-112	CEM	0.051	–	–	PEM fuel cell
Nafion NF-1135	CEM	0.089	–	–	PEM fuel cell
Nafion NF-115	CEM	0.127	–	–	PEM fuel cell
Nafion N-117	CEM	0.183	0.9	1.5	PEM fuel cell
FuMA-Tech GmbH, Germany					
FKS	CEM	0.090–0.110	0.9	2–4	Standard CEM
FKB	CEM	0.100–0.115	0.8	5–10	For EDBM
FK-40	CEM	0.035–0.045	1.2	1	Proton conductor, thin
FKD	CEM	0.040–0.060	1	1	Base dialysis
FAS	AEM	0.100–0.120	1.1	2–4	Standard AEM

FAB	AEM	0.090–0.110	0.8	2–4	For EDBM, acid blocker
FAN	AEM	0.090–0.110	0.8	2–4	Nitrate selective AEM
FAA	AEM	0.080–0.100	1.1	2.4	Base stable
FAD	AEM	0.08	1.3	1.2	Acid dialysis
Ionics Inc., USA					
CR61-CMP	CEM	0.58–0.70	2.2–2.5	11	ED whey
CR67-HMR	CEM	0.53–0.65	2.1–2.45	7.0–11.0	ED whey
CR67-HMP	–	–	–	–	EDI
AR103QDP	AEM	0.56–0.69	1.95–2.20	14.5	ED whey
AR204SZRA	AEM	0.48–0.66	2.3–2.7	6.2–9.3	EDR
AR112-B	AEM	0.48–0.66	1.3–1.8	20–28	Nitrate selective
MEGA a.s., Czech Republic					
Ralex MH-PES	AEM	0.55 (Dry)	1.8	<8	ED, EDI
Ralex AMH-5E	AEM	0.7 (Dry)	1.8	<13	Cataphoresis
Ralex CM-PES	CEM	0.45 (Dry)	2.2	<9	ED, EDI
Ralex CMH-5E	CEM	0.6 (Dry)	2.2	<12	Anaphoresis
PCA Polymerchemie Altmeier GmbH, Germany					
PC 100 D	AEM	0.08–0.1	1.2 Quat.	5	Small organic anions
PC 200 D	AEM	0.08–0.1	1.3 Quat.	2	Medium organic anions
PC Acid 35	AEM	0.08–0.1	1 Quat.	–	HCl production
PC Acid 70	AEM	0.08–0.1	1.1 Quat.	–	Pickling acids (HNO3/HF)
PC Acid 100	AEM	0.08–0.1	0.57 Quat.	–	Sulphuric acid production
PC-SK	CEM	–	–	–	Standard CEM
PC-SA	AEM	–	–	–	Standard AEM
Solvay S.A., Belgium					
Morgane CDS	CEM	0.130–0.170	1.7–2.2	0.7–2.1	Standard CEM
Morgane CRA	CEM	0.130–0.170	1.4–1.8	1.8–3.0	Reconc. of acids
Morgane ADP	AEM	0.130–0.170	1.3–1.7	1.8–2.9	High demin. Or recons.
Morgane AW	AEM	0.130–0.170	1.0–2.0	0.9–2.5 (HCl 1M)	

	–	–	–	1.3–4.4 (HNO3 1M)	HCl and HNO3 recovery
Tokuyama Co., Japan					
Neosepta CM-1	CEM	0.13–0.16	2.0–2.5	0.8–2.0	Low Rm
Neosepta CM-2	CEM	0.12–0.16	1.6–2.2	2.0–4.5	Low D
Neosepta CMX	CEM	0.14–0.20	1.5–1.8	2.0–3.5	High strength
Neosepta CMS	CEM	0.14–0.17	2.0–2.5	1.5–3.5	Univalent selective
Neosepta CMB	CEM	0.22–0.26	–	3.0–5.0	High strength
Neosepta AM-1	AEM	0.12–0.16	1.8–2.2	1.3–2.0	Low Rm
Neosepta AM-3	AEM	0.11–0.16	1.3–2.0	2.8–5.0	Low D
Neosepta AMX	AEM	0.12–0.18	1.4–1.7	2.0–3.5	High strength
Neosepta AHA	AEM	0.18–0.24	–	3.0–5.0	Base resistant
Neosepta ACM	AEM	0.10–0.13	1.4–1.7	3.5–5.5	Proton blocker
Neosepta ACS	AEM	0.12–0.20	1.4–2.0	3.0–6.0	Univalent selective
Neosepta AFN	AEM	0.15–0.18	2.0–3.5	0.2–1.0	Diff. dialysis
Neosepta AFX	AEM	0.14–0.17	1.5–2.0	0.7–1.5	Diff. dialysis
Tianwei Membrane Co. Ltd., China					
TWEDG	AEM	0.16–0.21	1.6–1.9	3–5	Standard AEM
TWDDG	AEM	0.18–0.23	1.9–2.1	<3	Standard AEM for DD
TWAPB	AEM	0.16–0.21	1.4–1.6	5–8	Proton blocker
TWANS	AEM	0.17–0.20	1.2–1.4	6–10	Nitrate selective AEM
TWAHP	AEM	0.20–0.21	1.2–1.4	<2	High protein flux
TWAEDI	AEM	0.18–0.21	1.6–1.8	6–8	For EDI
TWCED	CEM	0.16–0.18	1.4–1.6	2–4	Standard CEM
TWCDD	CEM	0.16–0.18	1.6–2.0	2–4	Standard CEM for DD
TWCEDI	CEM	0.16–0.18	1.2–1.4	5–8	For EDI

The measurement conditions to determine the area resistance varied with companies:

- Asahi Chemical Co., DuPont Co., Tokuyama Co.: 0.5M NaCl at 25 ◦C;
- Asahi Glass Co. Ltd.: 1 kHz AC in a 0.5M NaCl solution;
- FuMA-Tech, GmbH: 0.6M NaCl at 25 ◦C;
- PCA Polymerchemie Altmeier: GmbH, 1N KCl;
- Solvay S.A.: 1 kHz AC in 10 g/l NaCl at 25 ◦C, except AW (measured in a 1M H2SO4, HCl or HNO3 solution at 25 ◦C);
- Tianwei Co.: 0.1N NaCl at 17 ◦C.

B. Parameters for activity coefficients and equivalent conductivity evaluation

Evaluation of activity coefficients by Pitzer's equation (Chapter 3)

The Pitzer's correlation is a virial equation to estimate the activity coefficients in a wide range of solute concentration. The parameters presented in eq. (3.1) and (3.2) are defined as follows [74,75]:

$$B^{\gamma} = 2\beta^{(0)} + 2\beta^{(1)}\left[1-\left(1+\alpha m^{1/2}-\alpha^2 m/2\right)\exp\left(-\alpha m^{1/2}\right)\right]\Big/\alpha^2 m \quad \text{(B.1)}$$

$$B^{\varphi} = \beta^{(0)} + \beta^{(1)} e^{-\alpha\sqrt{I}} \quad \text{(B.2)}$$

$$C^{\gamma} = \frac{3}{2} C^{\varphi} \quad \text{(B.3)}$$

where α is a fixed constant (α = 2 (kg/mol)$^{1/2}$); *I'* and *m* are the ion strength and molality of the electrolyte, respectively; $\beta^{(0)}$, $\beta^{(1)}$, C^{φ} are the adjustable parameters, which are function of the nature of the electrolyte and determined from fitting with experimental data. The values for NaCl are reported in Table B.1.

Table B.1. Binary interaction parameters of Pitzer equation for NaCl [34].

$\beta^{(0)}$	$\beta^{(1)}$	C^{φ}
0.06743	0.3301	0.00263

Evaluation of equivalent conductivity by Islam's equation (Chapter 3)

The Islam's correlation is an extension of the Falkenhagen-Leist-Kelbg (FLK) equation to estimate the equivalent conductivity of electrolyte solution at high concentration [76]. The extended definitions of parameters in eq. (3.3) are reported below.

$$B'(c) = 50.29 \cdot 10^{8} \Big/ (\varepsilon T)^{1/2} \tag{B.4}$$

$$B_1'(c) = 82.5 \Big/ \left[\eta (\varepsilon T)^{1/2} \right] \tag{B.5}$$

$$B_2'(c) = 8.204 \cdot 10^{5} \Big/ (\varepsilon T)^{3/2} \tag{B.6}$$

$$F' = \frac{\left[\exp\left(0.2929\, B\, c^{1/2} a\right) - 1 \right]}{\left(0.2929\, B\, c^{1/2} a\right)} \tag{B.7}$$

where a is the adjustable parameter used in the correlation to fit the experimental data (a = 3.79 Å for NaCl); η, ε and T are viscosity, dielectric constant and temperature of the electrolyte solution, respectively.

Evaluation of activity coefficients by Staples' equation (Chapter 8)

For the model developed in Chapter 8, the correlation proposed by Staples [116] has been adopted:

$$\ln \gamma = \frac{-|z_+ z_-| A_\gamma \, m^{1/2}}{1 + B_\gamma \, m^{1/2}} + C_\gamma \, m + D_\gamma \, m^2 + E_\gamma \, m^3 \qquad (0.1)$$

where A_γ = 1.17625 $kg^{1/2}$ $mol^{-1/2}$, m is the molality of the solution (equal to the ionic strength, for 1:1-valent electrolyte [72]), z_+ and z_- are the cation and anion valence numbers, respectively. The coefficients B_γ, C_γ, D_γ, E_γ are evaluated by fitting experimental data collected from the literature [114]. Their values are reported in Table B.2.

Table B.2. Fitting parameters for Staples' equation.

Salt	B_γ	C_γ	D_γ	E_γ
Ammonium Bromide	1.3980	0.0203	0	0
Ammonium Chloride	1.2343	0.0233	9.98E-06	9.11E-07
Ammonium Hydrogen Carbonate	0	0	0	0
Ammonium Nitrate	0.5500	0	0	0
Lithium Bromide	0.9136	0.3788	2.16E-07	0
Lithium Chlorate	3.2239	0.1728	0	0
Lithium Chloride	1.1551	0.2882	0.0002	0
Lithium Nitrate	2.3142	0.1286	0	0
Potassium Acetate	1.6197	0.2048	5.79E-05	0
Potassium Bromide	1.2874	0.0295	0.0025	0
Potassium Chloride	1.2639	0.0181	5.40E-07	0.0006
Potassium Fluoride	1.2883	0.1236	0	0
Potassium Nitrate	0.3958	0	0	0
Sodium Bromide	1.1817	0.1595	0.0002	0
Sodium Chlorate	1.2187	0	0	0
Sodium Chloride	1.2751	0.0956	5.82E-05	0.0005
Sodium Nitrite	1.1785	0.0205	0	0

Evaluation of activity coefficients by Jones and Dole' equation (Chapter 8)

The equivalent conductivity is estimated by means of Jones and Dole' equation [117]:

$$\Lambda = \Lambda_0 - \frac{A_\Lambda \, c^{1/2}}{1 + B_\Lambda \, c^{1/2}} - C_\Lambda \, c \qquad (0.2)$$

where Λ_0 is the equivalent conductivity of salt at infinite dilution, c is the molar concentration, while A_Λ, B_Λ, C_Λ are model parameters used for fitting (Table B.3).

Table B.3. Fitting parameters for Jones and Dole' equation.

Salt	Λ_0 *	A_Λ	B_Λ	C_Λ
Ammonium Bromide	144.2605	31.1814	0	0.0077
Ammonium Chloride	149.6000	147.4843	3.4498	4.3618
Ammonium Hydrogen Carbonate	90.0000	41.5531	0.6023	0
Ammonium Nitrate	119.1743	13.8316	0	3.6929
Lithium Bromide	113.2420	31.5360	0	0.0073
Lithium Chlorate	112.0088	55.6221	0.2338	1.49E-07
Lithium Chloride	114.9700	42.9745	0.1045	0.0073
Lithium Nitrate	132.6046	82.0721	0.3727	0
Potassium Acetate	113.3042	42.7384	0.0644	3.7E-06
Potassium Bromide	151.8400	103.7700	1.8953	0.492
Potassium Chloride	149.5025	139.1595	3.2158	4.4275
Potassium Fluoride	142.1236	178.0337	2.3216	4.9626
Potassium Nitrate	144.8900	76.9314	0.4536	0.0152
Sodium Bromide	112.2101	18.4116	0.1714	6.0175
Sodium Chlorate	102.9242	30.7606	0.0245	0.5813
Sodium Chloride	126.5000	91.0239	1.6591	6.8041
Sodium Nitrite	122.7667	84.7105	0.2984	0

* Source: [123].

Evaluation of density of aqueous solutions for different salts (Chapter 8)

The solutions density has been estimated as a linear function of molal concentration for both dilute/concentrated solutions:

$$\rho = \rho_0 + \left(\frac{\Delta\rho}{\Delta m}\right) m \tag{0.3}$$

where ρ_0 is density of pure solvent at 25°C (0.997 g/ml [95]). The slope of the line was evaluated by fitting experimental data from literature [114,123], and their values are reported in Table B.4.

Table B.4. Values of parameters used for the estimation of density of aqueous solutions.

Salt	***Δρ/Δm***
Ammonium Bromide	0.0524
Ammonium Chloride	0.0128
Ammonium Hydrogen Carbonate	0.0324
Ammonium Nitrate	0.0149
Lithium Bromide	0.0441
Lithium Chlorate	0.0272
Lithium Chloride	0.0188
Lithium Nitrate	0.0250
Potassium Acetate	0.0262
Potassium Bromide	0.0810
Potassium Chloride	0.0395
Potassium Fluoride	0.0330
Potassium Nitrate	0.0539
Sodium Bromide	0.0643
Sodium Chlorate	0.0503
Sodium Chloride	0.0349
Sodium Nitrite	0.0409

REFERENCES

[1] B.E. Logan, M. Elimelech, Membrane-based processes for sustainable power generation using water, Nature. 488 (2012) 313–319.

[2] J.W. Post, J. Veerman, H.V.M. Hamelers, G.J.W. Euverink, S.J. Metz, K. Nymeijer, et al., Salinity-gradient power: Evaluation of pressure-retarded osmosis and reverse electrodialysis, J. Memb. Sci. 288 (2007) 218–230. doi:10.1016/j.memsci.2006.11.018.

[3] G.Z. Ramon, B.J. Feinberg, E. Hoek, Membrane-based production of salinity-gradient power, Energy Environ. Sci. 4 (2011) 4423–4434.

[4] G.L. Wick, W.R. Schmitt, Prospects for renewable energy from the sea, Mar. Technol. Soc. J. 11 (1977) 16–21.

[5] A. Achilli, A.E. Childress, Pressure retarded osmosis: From the vision of Sidney Loeb to the first prototype installation — Review, Desalination. 261 (2010) 205–211. doi:10.1016/j.desal.2010.06.017.

[6] D. Brogioli, Extracting renewable energy from a salinity difference using a capacitor, Phys. Rev. Lett. 103 (2009) 058501(4).

[7] B.B. Sales, M. Saakes, J.W. Post, C.J.N. Buisman, P.M. Biesheuvel, H.V.M. Hamelers, Direct power production from a water salinity difference in a membrane-modified supercapacitor flow cell, Environ. Sci. Technol. 44 (2010) 5661–5665.

[8] R. Baker, Membrane Technology and Application, 2nd Ed., 2004.

[9] S. Loeb, Large-scale power production by pressure-retarded osmosis, using river water and sea water passing through spiral modules, Desalination. 143 (2002) 115–122. doi:10.1016/S0011-9164(02)00233-3.

[10] X. Zhu, W. Yang, M.C. Hatzell, B.E. Logan, Energy recovery from solutions with different salinities based on swelling and shrinking of hydrogels., Environ. Sci. Technol. 48 (2014) 7157–63. doi:10.1021/es500909q.

[11] H. Strathmann, Ion-exchange membrane separation processes, Elsevier Science Limited, 2004.

[12] L. Gurreri, A. Tamburini, A. Cipollina, G. Micale, M. Ciofalo, CFD prediction of concentration polarization phenomena in spacer-filled channels for reverse electrodialysis, J. Memb. Sci. 468 (2014) 133–148. doi:http://dx.doi.org/10.1016/j.memsci.2014.05.058.

[13] J. Veerman, M. Saakes, S.J. Metz, G.J. Harmsen, Reverse electrodialysis: Evaluation of suitable electrode systems, J. Appl. Electrochem. 40 (2010) 1461–1474.

[14] R.E. Pattle, Production of Electric Power by mixing Fresh and Salt Water in the Hydroelectric Pile, Nature. 174 (1954) 660.

[15] R. Audinos, Inverse Electrodialysis. Study of Electric Energy Obtained Starting with Two Solutions of Different Salinity, J. Power Sources. 10 (1983) 203–217.

[16] J.N. Weinstein, F.B. Leitz, Electric power from differences in salinity: the dialytic battery, Sci. (New York, NY). 191 (1976) 557.

[17] J. Jagur-Grodzinski, R. Kramer, Novel process for direct conversion of free energy of mixing into electric power, Ind. Eng. Chem. Process Des. Dev. 25 (1986) 443–449.

[18] M. Turek, B. Bandura, Renewable energy by reverse electrodialysis, Desalination. 205 (2007) 67–74.

[19] M. Turek, B. Bandura, P. Dydo, Power production from coal-mine brine utilizing reversed electrodialysis, Desalination. 221 (2008) 462–466.

[20] J. Veerman, M. Saakes, S.J. Metz, G.J. Harmsen, Reverse electrodialysis: Performance of a stack with 50 cells on the mixing of sea and river water, J. Memb. Sci. 327 (2009) 136–144. doi:10.1016/j.memsci.2008.11.015.

[21] A. Daniilidis, D.A.A. Vermaas, R. Herber, K. Nijmeijer, Experimentally obtainable energy from mixing river water, seawater or brines with reverse electrodialysis, Renew. Energy. 64 (2014) 123–131. doi:http://dx.doi.org/10.1016/j.renene.2013.11.001.

[22] J. W. Post, Blue Energy: Electricity production from Salinity Gradients by Reverse Electrodialysis, Wageningen University, 2009.

[23] P. Długołęcki, Mass transport in Reverse Electrodialysis for Sustainable Energy Generation, Twente University, 2009.

[24] J. Veerman, Reverse Electrodialysis: design and optimization by modeling and experimentation, University of Groeningen, 2008.

[25] D.A.A. Vermaas, Energy generation from mixing salt water and fresh water: Smart flow strategies for reverse electrodialysis, University of Twente, 2014.

[26] D.A.A. Vermaas, M. Saakes, K. Nijmeijer, Doubled Power Density from Salinity Gradients at Reduced Intermembrane Distance, Environ. Sci. Technol. 45 (2011) 7089–7095. doi:10.1021/es2012758.

[27] E. Brauns, Towards a worldwide sustainable and simultaneous large-scale production of renewable energy and potable water through salinity gradient power by combining reversed electrodialysis and solar power?, Desalination. 219 (2008) 312–323. doi:10.1016/j.desal.2007.04.056.

[28] A. Cipollina, A. Misseri, G.D. Staiti, A. Galia, G. Micale, O. Scialdone, Integrated production of fresh water, sea salt and magnesium from sea water, Desalin. Water Treat. 49 (2012) 390–403.

[29] M. Tedesco, A. Cipollina, A. Tamburini, G. Micale, J. Helsen, M. Papapetrou, REAPower: use of desalination brine for power production through reverse electrodialysis, Desalin. Water Treat. 53 (2015) 3161–3169. doi:10.1080/19443994.2014.934102.

[30] P. Długołęcki, K. Nymeijer, S. Metz, M. Wessling, Current status of ion exchange membranes for power generation from salinity gradients, J. Memb. Sci. 319 (2008) 214–222. doi:10.1016/j.memsci.2008.03.037.

[31] M. Tedesco, A. Cipollina, A. Tamburini, W. van Baak, G. Micale, Modelling the Reverse ElectroDialysis process with seawater and concentrated brines, Desalin. Water Treat. 49 (2012) 404–424.

[32] P. Długołecki, B. Anet, S.J. Metz, K. Nijmeijer, M. Wessling, Transport limitations in ion exchange membranes at low salt concentrations, J. Memb. Sci. 346 (2010) 163–171.

[33] A.H. Galama, D.A. Vermaas, J. Veerman, M. Saakes, H.H.M. Rijnaarts, J.W. Post, et al., Membrane resistance: The effect of salinity gradients over a cation exchange membrane, J. Memb. Sci. 467 (2014) 279–291.

[34] R.K. Nagarale, G.S. Gohil, V.K. Shahi, Recent developments on ion-exchange membranes and electro-membrane processes., Adv. Colloid Interface Sci. 119 (2006) 97–130. doi:10.1016/j.cis.2005.09.005.

[35] O. Scialdone, C. Guarisco, S. Grispo, A.D. Angelo, A. Galia, Investigation of electrode material - Redox couple systems for reverse electrodialysis processes. Part I: Iron redox couples, J. Electroanal. Chem. 681 (2012) 66–75.

[36] J.W. Post, C.H. Goeting, J. Valk, S. Goinga, J. Veerman, H.V.M. Hamelers, et al., Towards implementation of reverse electrodialysis for power generation from salinity gradients, Desalin. Water Treat. 16 (2010) 182–193. doi:10.5004/dwt.2010.1093.

[37] A. Daniilidis, R. Herber, D.A. Vermaas, Upscale potential and financial feasibility of a reverse electrodialysis power plant, Appl. Energy. 119 (2014) 257–265. doi:http://dx.doi.org/10.1016/j.apenergy.2013.12.066.

[38] H. Strathmann, Electrodialysis, a mature technology with a multitude of new applications, Desalination. 264 (2010) 268–288. doi:10.1016/j.desal.2010.04.069.

[39] J. Veerman, M. Saakes, S.J. Metz, G.J. Harmsen, Reverse electrodialysis: A validated process model for design and optimization, Chem. Eng. J. 166 (2011) 256–268. doi:10.1016/j.cej.2010.10.071.

[40] C.H. Goeting, J. Valk, Membrane stack for a membrane based process and method for producing a membrane therefor, 2011.

[41] S. Pawlowski, J. Crespo, S. Velizarov, Pressure drop in reverse electrodialysis: Experimental and modeling studies for stacks with variable number of cell pairs, J. Memb. Sci. 462 (2014) 96–111. doi:http://dx.doi.org/10.1016/j.memsci.2014.03.020.

[42] L. Gurreri, A. Tamburini, A. Cipollina, G. Micale, CFD analysis of the fluid flow behavior in a reverse electrodialysis stack, Desalin. Water Treat. 48 (2012) 390–403.

[43] P. Długołecki, J. Dabrowska, K. Nijmeijer, M. Wessling, Ion conductive spacers for increased power generation in reverse electrodialysis, J. Memb. Sci. 347 (2010) 101–107.

[44] D.A.A. Vermaas, M. Saakes, K. Nijmeijer, Power generation using profiled membranes in reverse electrodialysis, J. Memb. Sci. 385–386 (2011) 234–242. doi:10.1016/j.memsci.2011.09.043.

[45] M.C. Hatzell, B.E. Logan, Evaluation of flow fields on bubble removal and system performance in an ammonium bicarbonate reverse electrodialysis stack, J. Memb. Sci. 446 (2013) 449–455.

[46] J. Veerman, J.W. Post, M. Saakes, S.J. Metz, G.J. Harmsen, Reducing power losses caused by ionic shortcut currents in reverse electrodialysis stacks by a validated model, J. Memb. Sci. 310 (2008) 418–430. doi:10.1016/j.memsci.2007.11.032.

[47] O. Scialdone, A. Albanese, A.D. Angelo, A. Galia, C. Guarisco, Investigation of electrode material - Redox couple systems for reverse electrodialysis processes. Part II: Experiments in a stack with 10–50 cell pairs, J. Electroanal. Chem. 704 (2013) 1–9. doi:http://dx.doi.org/10.1016/j.jelechem.2013.06.001.

[48] D.H. Kim, S.M. Moon, J. Cho, Investigation of the adsorption and transport of natural organic matter (NOM) in ion-exchange membranes, Desalination. 151 (2003) 11–20. doi:10.1016/S0011-9164(02)00968-2.

[49] W.E. Katz, The electrodialysis reversal (EDR) process, Desalination. 28 (1979) 31–40. doi:10.1016/S0011-9164(00)88124-2.

[50] R.P. Allison, Electrodialysis reversal in water reuse applications, Desalination. 103 (1995) 11–18. doi:10.1016/0011-9164(95)00082-8.

[51] D.A.A. Vermaas, D. Kunteng, J. Veerman, M. Saakes, K. Nijmeijer, Periodic feedwater reversal and air sparging as antifouling strategies in reverse electrodialysis, Environ. Sci. Technol. 48 (2014) 3065–3073.

[52] D.A.A. Vermaas, D. Kunteng, M. Saakes, K. Nijmeijer, Fouling in reverse electrodialysis under natural conditions, Water Res. 47 (2013) 1289–1298. doi:http://dx.doi.org/10.1016/j.watres.2012.11.053.

[53] T. XU, Ion exchange membranes: State of their development and perspective, J. Memb. Sci. 263 (2005) 1–29. doi:10.1016/j.memsci.2005.05.002.

[54] A. Tanioka, M. Kawaguchi, M. Hamada, K. Yoshie, Dissociation constant of a weak electrolyte in charged membrane, J. Phys. Chem. B. 102 (1998) 1730–1735. doi:10.1021/jp972900g.

[55] A. Philipse, A. Vrij, The Donnan equilibrium: I. On the thermodynamic foundation of the Donnan equation of state., J. Phys. Condens. Matter. 23 (2011) 194106. doi:10.1088/0953-8984/23/19/194106.

[56] J. Balster, D.. Stamatialis, M. Wessling, Electro-catalytic membrane reactors and the development of bipolar membrane technology, Chem. Eng. Process. Process Intensif. 43 (2004) 1115–1127. doi:10.1016/j.cep.2003.11.010.

[57] K. Kontturi, L. Murtomäki, J.A. Manzanares, Ionic Transport Processes: In Electrochemistry and Membrane Science, OUP Oxford, 2008.

[58] T. Sata, Studies on anion exchange membranes having permselectivity for specific anions in electrodialysis — effect of hydrophilicity of anion exchange membranes on permselectivity of anions, J. Memb. Sci. 167 (2000) 1–31. doi:10.1016/S0376-7388(99)00277-X.

[59] T. Xu, K. Hu, A simple determination of counter-ionic permselectivity in an ion exchange membrane from bi-ionic membrane potential measurements: Permselectivity of anionic species in a novel anion exchange membrane, Sep. Purif. Technol. 40 (2004) 231–236. doi:10.1016/j.seppur.2004.03.002.

[60] N. Lakshminarayanaiah, Transport phenomena in artificial membranes, Chem. Rev. 65 (1965) 491.

[61] N.P. Berezina, N.A. Kononenko, O.A. Dyomina, N.P. Gnusin, Characterization of ion-exchange membrane materials: properties vs structure., Adv. Colloid Interface Sci. 139 (2008) 3–28. doi:10.1016/j.cis.2008.01.002.

[62] E. Fontananova, W. Zhang, I. Nicotera, C. Simari, W. Van Baak, G. Di Profio, et al., Probing membrane and interface properties in concentrated electrolyte solutions, J. Memb. Sci. 459 (2014) 177–189. doi:http://dx.doi.org/10.1016/j.memsci.2014.01.057.

[63] J. Krol, Concentration polarization with monopolar ion exchange membranes: currentâ□“voltage curves and water dissociation, J. Memb. Sci. 162 (1999) 145–154. doi:10.1016/S0376-7388(99)00133-7.

[64] X. Dominguez-Benetton, S. Sevda, K. Vanbroekhoven, D. Pant, The accurate use of impedance analysis for the study of microbial electrochemical systems, Chem. Soc. Rev. (2012).

[65] P. Długołęcki, P. Ogonowski, S.J. Metz, M. Saakes, K. Nijmeijer, M. Wessling, On the resistances of membrane, diffusion boundary layer and double layer in ion exchange membrane transport, J. Memb. Sci. 349 (2010) 369–379. doi:10.1016/j.memsci.2009.11.069.

[66] H.Y. Lu, C.S. Lin, S.C. Lee, M.H. Ku, J.P. Hsu, S. Tseng, et al., In situ measuring osmosis effect of Selemion CMV/ASV module during ED process of concentrated brine from DSW, Desalination. 279 (2011) 278–284. doi:10.1016/j.desal.2011.06.020.

[67] C. Jiang, Y. Wang, Z. Zhang, T. Xu, Electrodialysis of concentrated brine from RO plant to produce coarse salt and freshwater, J. Memb. Sci. 450 (2014) 323–330. doi:http://dx.doi.org/10.1016/j.memsci.2013.09.020.

[68] T. Rottiers, K. Ghyselbrecht, B. Meesschaert, B. Van der Bruggen, L. Pinoy, Influence of the type of anion membrane on solvent flux and back diffusion in electrodialysis of concentrated NaCl solutions, Chem. Eng. Sci. 113 (2014) 95–100. doi:10.1016/j.ces.2014.04.008.

[69] C. Forgacs, Recent developments in the utilization of salinity power, Desalination. 40 (1982) 191–195.

[70] R.E. Lacey, Energy by reverse electrodialysis, Ocean Eng. 7 (1980) 1–47. doi:10.1016/0029-8018(80)90030-x.

[71] E. Brauns, Salinity gradient power by reverse electrodialysis: effect of model parameters on electrical power output, Desalination. 237 (2009) 378–391. doi:10.1016/j.desal.2008.10.003.

[72] J.O.M. Bockris, A.K.N. Reddy, Modern Electrochemistry vol. 1: Ionics, 2nd ed., Springer, 1998.

[73] K.M. Hangos, I.T. Cameron, Process modelling and model analysis, Academic Press, 2001.

[74] K.S. Pitzer, Thermodynamics of electrolytes. I. Theoretical basis and general equations, J. Phys. Chem. 77 (1973) 268–277.

[75] C.F. Weber, Calculation of Pitzer Parameters at High Ionic Strengths, Ind. Eng. Chem. Res. 39 (2000) 4422–4426. doi:10.1021/ie000411o.

[76] S.S. Islam, R.L. Gupta, K. Ismail, Extension of the Falkenhagen-Leist-Kelbg equation to the electrical conductance of concentrated aqueous electrolytes, J. Chem. Eng. Data. 36 (1991) 102–104.

[77] L. Gurreri, A. Tamburini, A. Cipollina, G. Micale, M. Ciofalo, CFD simulation of mass transfer phenomena in spacer filled channels for reverse electrodialysis applications, Chem. Eng. Trans. 32 (2013) 1879–1884.

[78] P. Englezos, N. Kalogerakis, Applied parameter estimation for chemical engineers, CRC, 2000.

[79] O.S. Burheim, F. Seland, J.G. Pharoah, S. Kjelstrup, Improved electrode systems for reverse electro-dialysis and electro-dialysis, Desalination. 285 (2012) 147–152. doi:10.1016/j.desal.2011.09.048.

[80] E. Güler, R. Elizen, M. Saakes, K. Nijmeijer, Micro-structured membranes for electricity generation by reverse electrodialysis, J. Memb. Sci. 458 (2014) 136–148. doi:http://dx.doi.org/10.1016/j.memsci.2014.01.060.

[81] P. Sistat, G. Pourcelly, Chronopotentiometric response of an ion-exchange membrane in the underlimiting current-range. Transport phenomena within the diffusion layers, J. Memb. Sci. 123 (1997) 121–131.

[82] M. Tedesco, A. Cipollina, A. Tamburini, I.D.L. Bogle, G. Micale, A simulation tool for analysis and design of reverse electrodialysis using concentrated brines, Chem. Eng. Res. Des. 93 (2015) 441–456. doi:10.1016/j.cherd.2014.05.009.

[83] S. Pawlowski, P. Sistat, J. Crespo, S. Velizarov, Mass transfer in reverse electrodialysis: Flow entrance effects and diffusion boundary layer thickness, J. Memb. Sci. 471 (2014) 72–83.

[84] M. Tedesco, E. Brauns, A. Cipollina, G. Micale, P. Modica, G. Russo, et al., Reverse Electrodialysis with saline waters and concentrated brines: a laboratory investigation towards technology scale-up, J. Membr. Sci. (2015).

[85] N.Y. Yip, D.A. Vermaas, K. Nijmeijer, M. Elimelech, Thermodynamic, energy efficiency, and power density analysis of reverse electrodialysis power generation with natural salinity gradients, Environ. Sci. Technol. 48 (2014) 4925–4936.

[86] D.A. Vermaas, E. Guler, M. Saakes, K. Nijmeijer, Theoretical power density from salinity gradients using reverse electrodialysis, Energy Procedia. 20 (2012) 170–184. doi:10.1016/j.egypro.2012.03.018.

[87] J. Veerman, M. Saakes, S.J. Metz, G.J. Harmsen, Electrical power from sea and river water by reverse electrodialysis: A first step from the laboratory to a real power plant, Environ. Sci. Technol. 44 (2010) 9207–9212.

[88] J.W. Post, H.V.M. Hamelers, C.J.N. Buisman, Influence of multivalent ions on power production from mixing salt and fresh water with a reverse

electrodialysis system, J. Memb. Sci. 330 (2009) 65–72. doi:10.1016/j.memsci.2008.12.042.

[89] E. Güler, W. van Baak, M. Saakes, K. Nijmeijer, Monovalent-ion-selective membranes for reverse electrodialysis, J. Memb. Sci. 455 (2014) 254–270. doi:http://dx.doi.org/10.1016/j.memsci.2013.12.054.

[90] D.A. Vermaas, J. Veerman, M. Saakes, K. Nijmeijer, Influence of multivalent ions on renewable energy generation in reverse electrodialysis, Energy Environ. Sci. 7 (2014) 1434–1445.

[91] M. Tedesco, P. Mazzola, A. Tamburini, G. Micale, I.D.L. Bogle, M. Papapetrou, et al., Analysis and simulation of scale-up potentials in reverse electrodialysis, Desalin. Water Treat. Doi 10.1080/19443994.2014.947781. (n.d.).

[92] R.A. Tufa, E. Curcio, W. Van Baak, J. Veerman, S. Grasman, E. Fontananova, et al., Potential of brackish water and brine for energy generation by salinity gradient power-reverse electrodialysis (SGP-RE), RSC Adv. 4 (2014) 42617–42623.

[93] X. Luo, X. Cao, Y. Mo, K. Xiao, X. Zhang, P. Liang, et al., Power generation by coupling reverse electrodialysis and ammonium bicarbonate: Implication for recovery of waste heat, Electrochem. Commun. 19 (2012) 25–28.

[94] F. Ullman, Ullmann's encyclopedia of industrial chemistry, Wiley-VCH Verlag GmbH. (2005) 1499.

[95] R.H. Perry, D.W. Green, J.O. Maloney, Perry's chemical engineers' handbook, McGraw-Hill New York, 2008.

[96] R.D. Cusick, Y. Kim, B.E. Logan, Energy capture from thermolytic solutions in microbial reverse- electrodialysis cells, Science (80-.). 335 (2012) 1474–1477.

[97] J.Y. Nam, R.D. Cusick, Y. Kim, B.E. Logan, Hydrogen generation in microbial reverse-electrodialysis electrolysis cells using a heat-regenerated salt solution, Environ. Sci. Technol. 46 (2012) 5240–5246.

[98] R.L. McGinnis, M. Elimelech, J.R. McCutcheon, Osmotic heat engine, 2008.

[99] R.L. McGinnis, J.R. McCutcheon, M. Elimelech, A novel ammonia-carbon dioxide osmotic heat engine for power generation, J. Memb. Sci. 305 (2007) 13–19.

[100] B.E. Logan, K. Rabaey, Conversion of Wastes into Bioelectricity and Chemicals by Using Microbial Electrochemical Technologies, Science (80-.). 337 (2012) 686–690. doi:10.1126/science.1217412.

[101] S. Loeb, Method and apparatus for generating power utilizing pressure-retarded-osmosis, 1975.

[102] M. Marino, A. Carati, L. Galgani, D. Brogioli, Theoretical thermodynamic analysis of a closed-cycle process for the conversion of heat into electrical energy by means of a distiller and an electrochemical cell, Renew. Energy. (2014).

[103] A.B. Little, S. Garimella, Comparative assessment of alternative cycles for waste heat recovery and upgrade, Energy. 36 (2011) 4492–4504. doi:http://dx.doi.org/10.1016/j.energy.2011.03.069.

[104] A.S. Rattner, S. Garimella, Energy harvesting, reuse and upgrade to reduce primary energy usage in the USA, Energy. 36 (2011) 6172–6183.

[105] International Energy Agency, Combined Heat and Power-Evaluating the benefits of greater global investment., Paris, Fr. (2008).

[106] P. Donnellan, K. Cronin, E. Byrne, Recycling waste heat energy using vapour absorption heat transformers: A review, Renew. Sustain. Energy Rev. 42 (2015) 1290–1304. doi:10.1016/j.rser.2014.11.002.

[107] B. Inc, Waste Heat Recovery: Technology Opportunities in the US Industry, in: Waste Heat Recover. Technol. Oppor. US Ind., 2008: pp. 1–112.

[108] E.H. Wang, H.G. Zhang, B.Y. Fan, M.G. Ouyang, Y. Zhao, Q.H. Mu, Study of working fluid selection of organic Rankine cycle (ORC) for engine waste heat recovery, Energy. 36 (2011) 3406–3418. doi:10.1016/j.energy.2011.03.041.

[109] Q. Zhang, Y. Sun, W. Xu, D. Zhu, Organic Thermoelectric Materials: Emerging Green Energy Materials Converting Heat to Electricity Directly and Efficiently., Adv. Mater. 26 (2014) 6829–6851. doi:10.1002/adma.201305371.

[110] L.E. Bell, Cooling, heating, generating power, and recovering waste heat with thermoelectric systems., Science. 321 (2008) 1457–1461. doi:10.1126/science.1158899.

[111] J. Karthauser, T. Östrom, Method for conversion of low temperature heat to electricity and cooling, and system therefore, 2012.

[112] M. Higa, D. Masuda, E. Kobayashi, M. Nishimura, Y. Sugio, T. Kusudou, et al., Charge mosaic membranes prepared from laminated structures of PVA-based charged layers1. Preparation and transport properties of charged mosaic membranes, J. Memb. Sci. 310 (2008) 466–473. doi:10.1016/j.memsci.2007.11.024.

[113] D.A. Vermaas, J. Veerman, N.Y. Yip, M. Elimelech, M. Saakes, K. Nijmeijer, High efficiency in energy generation from salinity gradients with reverse electrodialysis, ACS Sustain. Chem. Eng. 1 (2013) 1295–1302.

[114] V.M.M. Lobo, J.L. Quaresma, Handbook of electrolyte solutions, Elsevier, 1989.

[115] G.M. Geise, H.J. Cassady, D.R. Paul, B.E. Logan, M.A. Hickner, Specific ion effects on membrane potential and the permselectivity of ion exchange membranes, Phys. Chem. Chem. Phys. 16 (2014) 21673–21681. doi:10.1039/C4CP03076A.

[116] B.R. Staples, Activity and Osmotic Coefficients of Aqueous Alkali Metal Nitrites, J. Phys. Chem. Ref. Data. 10 (1981) 765–777.

[117] G. Jones, C.F. Bickford, The conductance of aqueous solutions as a function of the concentration. I. Potassium bromide and lanthanum chloride, J. Am. Chem. Soc. 56 (1934) 602–611.

[118] GAMS Integrated Development Environment v24.1, GAMS Softw. GmbH. (2013).

[119] G. Micale, A. Cipollina, L. Rizzuti, Seawater Desalination for Freshwater Production, Springer, 2009.

[120] K.C. Ng, K. Thu, Y. Kim, A. Chakraborty, G. Amy, Adsorption desalination: An emerging low-cost thermal desalination method, Desalination. 308 (2013) 161–179. doi:http://dx.doi.org/10.1016/j.desal.2012.07.030.

[121] G. Zaragoza, A. Ruiz-Aguirre, E. Guillén-Burrieza, Efficiency in the use of solar thermal energy of small membrane desalination systems for decentralized water production, Appl. Energy. (2014).

[122] S. Quoilin, M. Van Den Broek, S. Declaye, P. Dewallef, V. Lemort, Techno-economic survey of Organic Rankine Cycle (ORC) systems, Renew. Sustain. Energy Rev. 22 (2013) 168–186. doi:http://dx.doi.org/10.1016/j.rser.2013.01.028.

[123] D.R. Lide, CRC Handbook of chemistry and physics, 86th edn, 2005–2006, CRC Press, Boca Raton, 2005.